Asteroseismology of Intermediate Mass Stars: Pre-main Sequence Evolution

by

Joel Tanner

A Thesis Submitted to Saint Mary's University, Halifax, Nova Scotia in Partial Fulfillment of the Requirements for the Degree of

MASTER OF SCIENCE

in

Astronomy

(Department of Astronomy and Physics)

Aug 1, 2007, Halifax, Nova Scotia

© Joel Tanner, 2007

Approved: ....
             Dr. D. Guenther
             Supervisor

Approved: ....
             Dr. C.I. Short
             Examiner

Approved: ....
             Dr. R.G. Deupree
             Examiner

Date:

Canada

Acknowledgements

I am greatly indebted to my advisor, Dr. David Guenther, for his guidance, encouragement and words of wisdom. David has been my mentor during my time at Saint Marys and I remain grateful for his wisdom and the enlightening discussions we shared over the past few years.

It is a pleasure to thank my thesis examiners, Drs. Bob Deupree and Ian Short, for providing me with thoughtful comments and interminable support. In addition to serving on the examination committee, Bob and Ian have been a valuable influence throughout my studies, and I am appreciative for the time and effort they invested in my education. I would also like to thank Dr. David Turner for stimulating my interest in pre-main sequence isochrones.

Finally, I am most fortunate to be part of a loving family, all of whom continue to encourage and support me in striving toward my goals.

Contents

List of Figures

List of Tables

Abstract

Asteroseismology of Intermediate Mass Stars: Pre-main Sequence

Evolution

by Joel Tanner

We investigate in detail the potential of asteroseismology in exploring the structure of intermediate mass ($1.6 \leq M_\odot \leq 5.0$) pre-main sequence stars. It is expected that pre- and post-main sequence stars will produce differing oscillation spectra due to the dependance of oscillation frequencies on the internal structure of that star. We compute densely populated grids of pre- and post-main sequence stellar models, which are then used as a tool to explore the oscillation frequencies of pre-main sequence stars. We examine the cause of the oscillation spectra by correlating the frequencies with changes in stellar structure and comparing fundamental properties of pre-main sequence stars to their post-main sequence counterparts. By fashioning a set of oscillation frequencies designed to mimic observed oscillation spectra, we determine the conditions under which we can distinguish the evolutionary state of a star through its oscillation spectra alone, and explore our ability to constrain stellar parameters as a function of the quality of the observed frequency spectrum. Using the dense grids to construct precise pre-main sequence isochrones, we fit them to two young open clusters. Finally, we present efforts in constraining the stellar parameters of two pre-main sequence stars by matching the observed frequencies to the calculated frequency spectra of all grid models.

August 14, 2007

Chapter 1

Introduction

1.1 Star Formation and the Birthline

It is difficult to determine the precise initial conditions prior to the onset of pre-main sequence (PMS) evolution. The broad theory of star formation begins with the accretion of material from circumstellar surroundings onto a protostar progenitor, and during this phase, the accreted circumstellar material directly influences the stellar photosphere causing irregular variability. To properly model star formation, the necessary physics must include theoretical flux calculations as well as radiation hydrodynamics, convection, and magnetic fields. Recent advances have yielded models that include this required physics and are able to follow star formation from the molecular cloud through to protostellar collapse and the halt of accretion (eg: Banarjee & Pudritz (2007); Wuchterl (1999); Larson (2007)). However, PMS stars do not become visible until well after the mass accretion phase, so in the context of asteroseismology, accurately modeling star formation is not required.

Interstellar clouds will collapse when the cloud's self-gravity exceeds internal pressure support, at which point the cloud collapses non-homologously, eventually establishing a hy-

drostatic core surrounded by an optically thick dust envelope. From this point forward, the evolution of the hydrostatic core is determined by the mass accretion rate, which can proceed with rates in excess of 10^{-3} $M_\odot$ per year (Banarjee & Pudritz, 2007) for massive stars. After the envelope has accreted onto the core, the protostellar core begins quasi-static contraction along the Hayashi track, at which time the star can become optically visible. This location in the HR-diagram, called the birthline, has been predicted for various masses and mass flow rates by Stahler (1988), Palla & Stahler (1990), and Palla & Stahler (1991). Based on a spherically symmetric collapse of a progenitor cloud, neglecting rotation, turbulent motion, and magnetic fields, the predicted birthline for low-mass stars ($0.2 \leq M_\odot \leq 1.0$) is in agreement with observations of low-mass T Tauri stars. Palla & Stahler (1990) computed the birthline for intermediate-mass stars (Palla & Stahler, 1990) by combining pre-main sequence evolutionary tracks with a theoretical mass-radius relationship for accreting protostars. Although deuterium is quickly burnt during the early protostar phase (Stahler, Shu & Taam, 1980), its burning significantly influences the radius of the forming star during the accretion phase, and therefore the location of the birthline (Stahler, 1988). Unlike the early evolution of low mass stars, the burning of deuterium in intermediate mass stars does not play a significant role in the protostar formation because the rate at which the deuterium is fused is shorter than the mass accretion rate. For intermediate mass stars ($1.6 \leq M_\odot \leq 5.0$), the effect of deuterium burning on evolution is not expected to be important. Although deuterium is present in stars of this mass, it exists in a thin surface layer only and is rapidly destroyed during the final contraction to the ZAMS (Palla & Stahler, 1999). The early mass accretion phase is not dealt with in our models, rather we start evolution just after the formation of the protostellar core (see section 2.1

for details). Once on the ZAMS, nuclear burning in the interior replaces gravity as the dominant energy source and contributor to the radiated surface flux.

1.2 Fundamentals of Stellar Pulsation and Asteroseismology

Observations of stars are limited to their surface properties. For example, a star's brightness can be measured at a given wavelength, or the composition determined by observing the spectrum of the atmosphere. Much like seismology is the study of earthquakes, asteroseismoloy provides a means to probe the detailed internal structure of a star by observing the vibrations of the stellar surface. Both Unno *et al.* (1989) and Cox (1980) provide a thorough examination of stellar pulsation. The purpose of the following section is to review the fundamentals of asteroseismology pertinent to this thesis and to provide basic technical knowledge concerning stellar pulsation. Christensen-Dalsgaard *et al.* (2003) presents a detailed study of the linear theory of nonradial oscillations of spherically symmetric stars, and the techniques employed in solving the equations of stellar oscillations.

The linearized equations describing non-radial stellar oscillations are separable into an angular component described by spherical harmonics that characterizes the oscillation pattern in the stellar interior and surface regions, and a radial component that must be solved on a computer. Perturbations to a spherically symmetric, non-rotating star are described by

the product of a function of radius and a spherical harmonic:

$$\xi(r,\theta,\phi,t) = \xi_{nl}(r)Y_l^m(\theta,\phi)e^{i\omega t}, \tag{1.1}$$

where r, θ, ϕ, t are the radial coordinate, colatitude, longitude, and time, respectively. In adiabatic theory, the function ξ is the perturbation associated with a radial, pressure, gravitational potential, or the derivative of gravitational potential. The value ω is the angular frequency of the wave (related to the observed frequency by $\omega_{nlm} = 2\pi\nu_{nlm}$), and $Y_l^m(\theta,\phi)$ are spherical harmonics given by:

$$Y_l^m(\theta,\phi) = (-1)^m C_{lm} P_l^m(cos\theta)e^{im\phi}. \tag{1.2}$$

The radial order n is equal to the number of perturbation nodes on a radial line from the center to the surface. The degree l corresponds to the number of perturbation nodes parallel to lines of longitude and is always > 0, while the azimuthal order m is a measure of the number of nodes parallel to lines of latitude and ranges from $-l < m < l$. P-modes all have $n \geq 1$, however they are not all directly observable. When considering stars in spherical symmetry, as is done in the forthcoming discussion, the mode frequencies depend only on n and l.

Stellar oscillations are classified as either pressure waves (p-modes), or gravity waves (g-modes). P-modes are acoustic waves where the dominant restoring force is pressure, and are found to propagate in the outermost regions of stars, such as convective envelopes, where they are driven by stochastic excitation of convection. P-modes reach maximum

amplitude in the outer convective envelopes, and are thus the easiest to observe. Gravity is the dominant restoring force in g-modes. These modes propagate in the interior of stars, such as radiative cores, and are damped in convective regions. Predicted to exist in solar type stars, g-modes could bear important information about stellar cores (Demarque & Guenther, 1999). It is possible for p-modes to be purely radial with degree $l = 0$, however, g-modes are always variable in the horizontal coordinates and therefore must have $l \geq 1$.

1.3 Asymptotic Theory for p-modes

The asymptotic theory of stellar pulsation approximates the frequencies of p-modes when the radial order (n) is much greater than the degree (l). Oscillation frequencies are detected through Doppler-shifted light from the stellar surface, measured as a time-series of luminosity or velocity. The easiest mode to detect is for $l = 0$, which corresponds to the stellar radius expanding or contracting uniformly in all directions. Because modes of high degree exhibit many patches of the stellar surface that are expanding and contracting simultaneously, the light variability is not as extreme and more difficult to detect. Further, because stars are unresolved point sources, the observed light is integrated over the entire surface, hence the peaks and troughs will average out. Figure 1.1 shows some examples of low l oscillation modes that can exist in stars. High degree modes are seen in the sun because observers can resolve the solar surface, but all other stars are observed as point sources so observations are limited to low l. Asteroseismology, unlike helioseismology, is

therefore concerned with the calculation of low l modes.

As asymptotic theory predicts, p-mode frequencies are observed at regularly spaced intervals that correspond to modes of subsequent radial order. Low resolution frequency spectra exhibit regularly spaced $l = 0$ modes, the separation between frequencies defined as the large spacing, $\Delta_{n,l}$, with $l = 1$ modes falling approximately halfway between $l = 0$ modes. Higher resolution spectra will include similarly spaced frequencies for $l = 2$ and $l = 3$ modes, which appear near the $l = 0$ and $l = 1$ modes, respectively. These higher degree modes reveal another separation in frequency called the small spacing, $\delta_{n,l}$, which corresponds to the difference of the most closely matched frequencies from modes differing in degree by $\Delta l = 2$. Figure 1.2 shows a sample frequency spectrum, with frequency on the abscissa, and amplitude on the ordinate. The schematic shows modes of degree $l = 0$ through $l = 3$ and identifies the large and small frequency spacings.

The echelle diagram is a convenient method of illustrating frequency spectrum properties. In it, the frequencies are plotted on the ordinate against a folding frequency on the abscissa, which is simply the frequency modulo $\Delta\nu$. Specifically, the folded frequency is calculated with:

$$\nu_{fold} = \nu_0 + \nu - b\Delta\nu, \tag{1.3}$$

where ν is the frequency of a given mode, b is an integer so that ν_{fold} is between 0 and $\Delta\nu$, and ν_0 is an arbitrary zero point shift. Generally, it is convenient to choose a $\Delta\nu$ similar to the large spacing through the frequency range of interest. This diagram results in frequencies arranged vertically in lines comprising modes of the same degree l. Figure
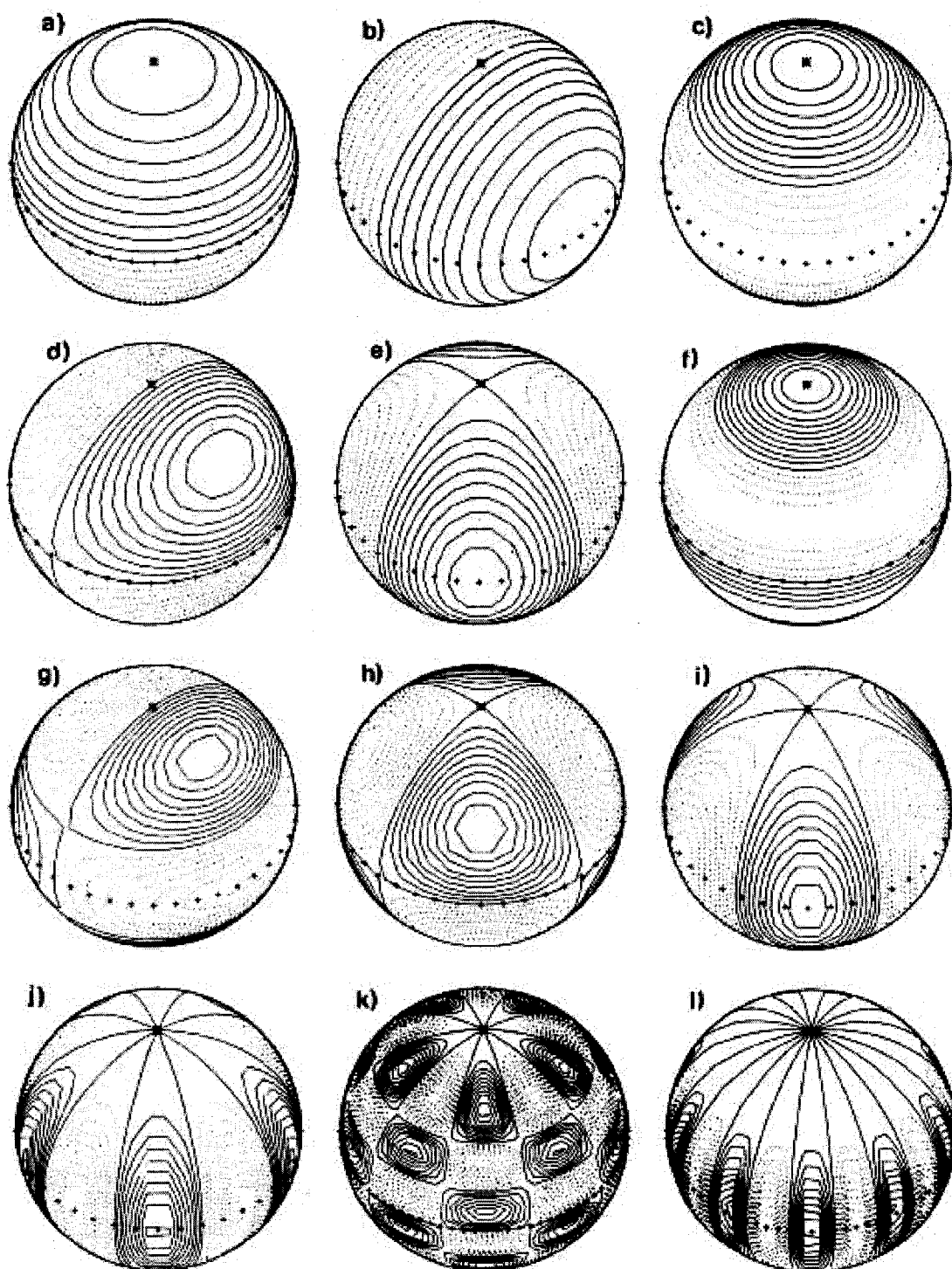
Figure 1.1 Examples of spherical harmonics for differing values of l and m (Christensen-Dalsgaard *et al.*, 2003). Lines represent the positive (solid) and negative (dashed) contours of the real component of spherical harmonics Y_l^m (see equation 1.2). The axis of rotation is inclined 45 degrees forward. The following modes are illustrated: $a)l = 1, m = 0; b)l = 1, m = 1; c)l = 2, m = 0; d)l = 2, m = 1; e)l = 2, m = 2; f)l = 3; m = 0; g)l = 3; m = 1; h)l = 3, m = 2; i)l = 3, m = 3; j)l = 5, m = 5; k)l = 10, m = 5; l)l = 10, m = 10.$
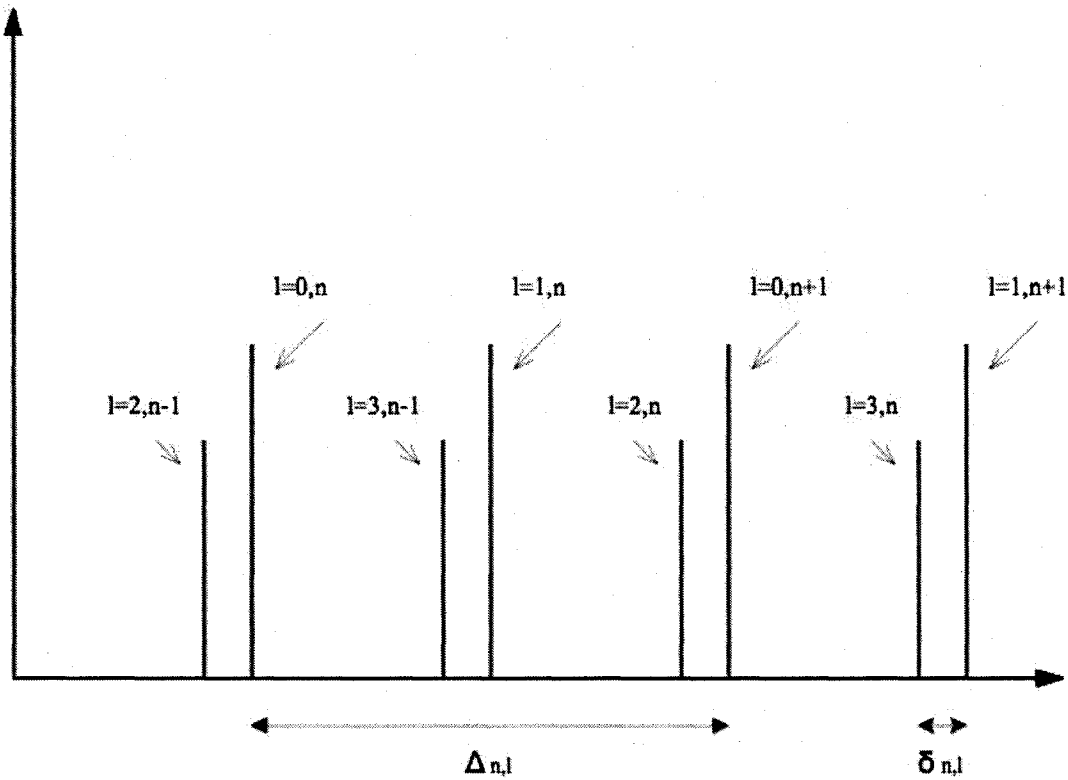
Figure 1.2 Schematic of oscillation spectrum showing $l = 0, 1, 2$ and 3 modes of a non-rotating star. The degree and order of each mode are indicated as well as the large $(\Delta \nu)$ and small $(\delta \nu)$ spacing.

1.3 shows the same sample frequency spectrum, but presented as an echelle diagram, which

arranges modes of the same l in vertical lines. The large and small frequency separations

are identified in the figure.

P-mode frequencies for $n \gg l$ have been characterized by Tassoul (1980), who illustrated

the dependence of frequency on sound speed:

$$\nu_{nl} = \frac{\omega_{nl}}{2\pi} \approx \left(n + \frac{1}{2} + \frac{1}{4} + \beta \right) \Delta \nu - (AL^2 - \epsilon) \frac{\Delta \nu^2}{\nu_{nl}}, \tag{1.4}$$

Folded Frequency
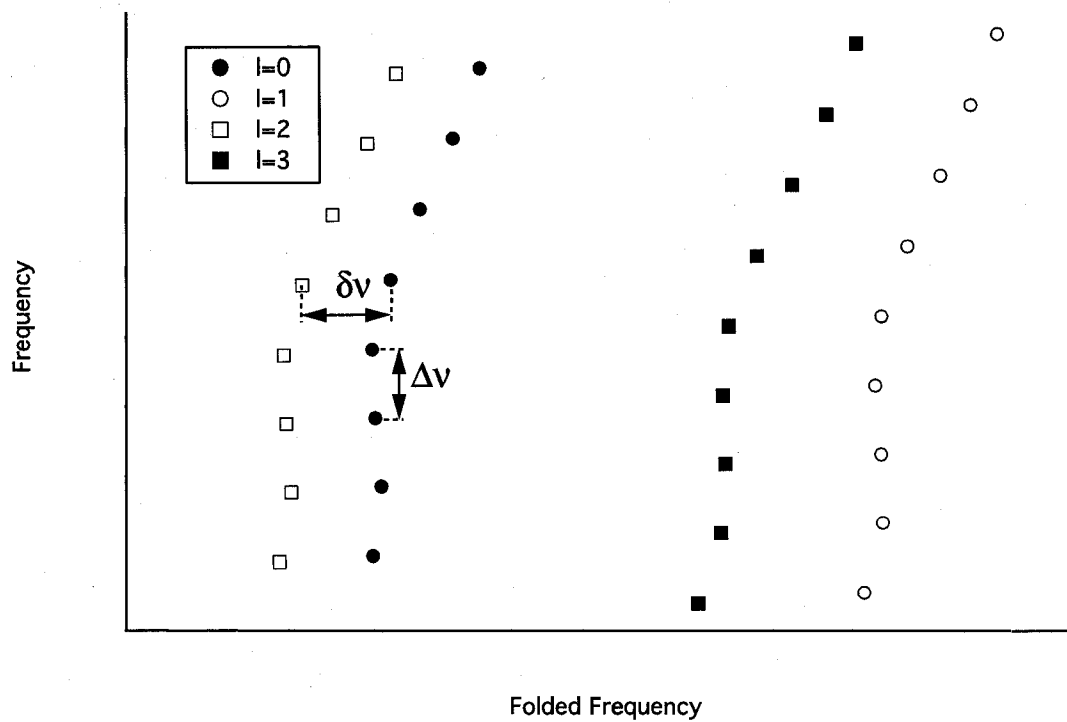
Figure 1.3 Schematic of an echelle diagram showing $l = 0, 1, 2$ and 3 modes of a non-rotating star. The degree of the modes are indicated as well as the large $(\Delta\nu)$ and small $(\delta\nu)$ spacing.

where

$$\Delta\nu = \left(2\int_0^R \frac{dr}{c_s}\right)^{-1},$$ (1.5)

and

$$A = \frac{1}{4\pi^2\Delta\nu}\left(\kappa - \int_0^R \frac{dc_s}{dr}\frac{dr}{r}\right).$$ (1.6)

In equations (1.4), (1.5), and (1.6), n and l are the radial order and degree of the mode, r is the radial location in the star, $L = l + 1/2$, c_s is the sound speed and the constants β, ϵ, and κ are dependent on the structure of the stellar surface layers and are independent of l. The second order term for the p-mode frequency depends on stellar structure. The first and second order terms can be isolated as follows:

$$\Delta_n \equiv \nu_{nl} - \nu_{n-1,l} \propto \Delta\nu,$$ (1.7)

$$\delta_{nl} = \nu_{nl} - \nu_{n-1,l+2} \propto \Delta\nu \int_0^R \frac{dc}{dr}\frac{dr}{r}.$$ (1.8)

Equations (1.7) and (1.8) are the large and small spacings, respectively. Equation (1.7) reveals that to leading order Δ_n is proportional to $\Delta\nu$, thus the large spacing is strongly influenced by the sound speed in the surface layers (refer to equation 1.5) and is in fact, a measure of the p-mode crossing time (Isaak & Isaak, 2001). For an ideal gas, the sound speed varies according to:

$$c_s^2 = \frac{k_B T}{\mu m_H},$$ (1.9)

where k_B is the Boltzmann constant, μ is the mean molecular weight, and m_H is the atomic weight of Hydrogen.

The small spacing (equation 1.8) is related to the asymptotic expression (equation 1.6) by the following equation (Tassoul, 1980):

$$\delta_{nl} \approx -(4l-6)\frac{\Delta\nu}{4\pi^2\nu_{nl}}\int_0^R \frac{dc_s}{dr}\frac{dr}{c_s}. \tag{1.10}$$

From equation 1.10, the small spacing depends predominantly on the derivative of the sound speed in the stellar interior. The small spacing is sensitive to the mean molecular weight as well as the structure of the core, and so reflects the evolutionary state of the star (Guenther, 2002).

1.4 Oscillations and Fundamental Properties

A Fourier transform of the power spectrum will show peaks at the small spacing and at half of the large spacing, which could provide constraints on the structure of the star. However, the useful interpretation of the spacings is increasingly limited after the star evolves from the ZAMS (Guenther, 2002) and mode bumping disrupts the regular spacing. Mode bumping occurs when the range of g-mode frequencies overlap with the range in p-mode frequencies, resulting in specific p- and g-modes interfering with each other. Nonetheless, the large and small spacings are a manifestation of acoustic wave crossing time (which is to first order proportional to radius) and evolutionary state, respectively.

Sound speed depends on the temperature and the mean molecular weight (refer to equation 1.9), and decreases with the temperature near the stellar surface. We present a detailed

examination of sound speed for specific models in section 2.4. The large spacing depends on $1/c_s$, so it is most sensitive to regions where $1/c_s$ is large (ie: where c_s is small) which occurs near the surface. From the dependance on radius, the large spacing is related to the dynamical time scale, and by extension the mean stellar density, by the relation:

$$t_{dyn} \approx \sqrt{\frac{R^3}{GM}} \approx \frac{1}{\sqrt{G \langle \rho \rangle}}. \tag{1.11}$$

Individual p-mode frequencies as well as the frequency spacings change with the evolution of the star. For stars evolving from the ZAMS, the increasing radius will cause the p-mode frequencies to decrease, while the opposite is true for pre-main sequence stars that evolve from the Hayashi track toward the main sequence.

The use of observed p-mode frequencies has been proposed as a means to deduce stellar properties (eg: Christensen-Dalsgaard (1993)). This pioneering work resulted in the development of the asteroseismic HR diagram, which shows the large spacing versus small spacing throughout the evolution of a star. When combined with an accurate estimate of composition, this diagram relates the mass and age of a star to the large and small spacings from the p-mode oscillations. We present a detailed discussion of this subject in section 3.2 that includes an examination of the PMS astroseismic HR diagram.

Asteroseismology can aid in constraining stellar properties if other stellar parameters are known. For example, an estimate of radius combined with the small spacing uniquely determines a stellar model. Of course, it is preferable to use stellar properties that are independent. For instance, it is difficult to isolate a single model using radius and large

spacing, because the radius is a primary factor in determining the large spacing.

1.5 Pre-Main Sequence Stars

Pre-main sequence stars lie between the birthline and the ZAMS in the HR diagram. Because they still interact with the circumsteller environment from which they recently formed, they are often characterized by IR excesses and emission lines, and can show photometric and spectroscopic variability (Zwintz *et al.*, 2005b). The fact that PMS stars move through the classical instability strip suggests that the variability could be due to stellar pulsations similar to δ-Scuti stars, which are pulsating variables that exist in the lower part of the instability strip. They show small, regular light variations from radial and non-radial modes with periods ranging from minutes to hours.

1.5.1 T Tauri Stars

First discovered by Joy (1942), T Tauri stars are newly formed low-mass stars that have recently become optically visible. Several studies (eg: Joy (1945); Herbig (1962)) show that these stars are in the PMS phase of evolution. They exhibit large irregular light variations on time scales ranging from minutes to years that could be attributed to instabilities in a residual accretion disk, or activity in the stellar atmosphere. The spectral type of T Tauri stars is typically G, K or M and they have normal photospheres with continuum and line-emission characteristics of a hotter envelope (7000K to 10000K). Based on spectroscopic properties, T Tauri stars are recognizable as members of two broad catagories: Classical

T Tauri Stars (CTTSs) and weak-lined T Tauri Stars (WTTSs). CTTSs are characterized by extensive disks that result in strong emission lines, including Ca II H and K lines, Fe I emission at $\lambda = 4063$ and 4132 Å, O I and S II, and Li I at $\lambda = 6707$ Å. WTTSs are surrounded by a weak or non-existent disk and are X-ray sources with a pre-main sequence optical counterpart. WTTSs are particularly useful because they are relatively unobstructed by circumstellar material.

1.5.2 Herbig Ae/Be Stars

Herbig Ae/Be (HAEBE) stars are more massive (between 2 and 10 $M_\odot$) than T Tauri stars. HAEBE stars are radiatively stable during quasi-static contraction, consequently they have a lower mass limit near $2M_\odot$. The upper mass limit corresponds to the intersection of the birthline and the ZAMS. Above this mass limit, stars have no observable pre-main sequence evolutionary paths in the HR diagram, but appear directly on the ZAMS. HAEBE stars have spectral type A or B with luminosity class III to V and exhibit strong emission in H-alpha and Ca H and K lines as well as an IR excess attributed to hot or cool circumstellar dust. HAEBE stars also show emission lines from O I, Ca II, Si II, Mg II and Fe II.

The large volume of cirumstellar material that characterizes HAEBE stars contributes to the spectral energy distribution (SED) in the UV and dominates the SED in the IR, making it difficult to distinguish between the circumstellar material and the photosphere. Observed UV excess is attributed to accretion rates on the order of 10^{-7} $M_\odot$ per year, and because these stars are often found in star forming regions, extinctions for individual stars

can differ significantly from the average extinction of the ISM.

HAEBE stars exhibit both regular and irregular variability. UX Ori type stars experience large and sudden drops in magnitude accompanied by an increased reddening and degree of polarization, followed by a slow return to the initial magnitude. This kind of variation is only observed in stars of spectral types A0 and later. A second type of variability is connected with gradual changes in the degree of cirumstellar extinction, and is characterized by long-term fading on time scales of years. HAEBE stars also exhibit millimagnitude variability due to stellar pulsation as they traverse the instability strip in the HR diagram. The mass range of the pre-main sequence models studied here overlaps low mass HAEBE stars and high mass T Tauri stars.

1.6 Stellar Modeling

Constructing an accurate stellar model requires knowledge of seven fundamental stellar properties: mass, age, luminosity, helium composition, metal composition, effective temperature and mixing length. For comparison with real stars, most of these model properties can be directly determined through observation.

Stellar masses are commonly determined from precisely measured orbital parameters of binary systems, or (for main sequence stars) inferred through the mass-luminosity relation. Luminosity is derived from measurements of the bolometric magnitude, coupled with an estimate of the distance. The stellar composition is typically determined through

comparison with computed atmospheres, and the temperature is usually determined from color indices or spectral line equivalent widths. The mixing length parameter, however, is not determined through observation. This parameter is part of the mixing length theory (Böhm-Vitense, 1958), which characterizes convection by assuming that convective energy is transported a distance l (the mixing length) by a convective bubble. The mixing length is assumed to be proportional to the pressure scale height $l = \alpha H_P$, where α is the mixing length parameter, and the pressure scale height, H_P is, given by:

$$H_P = -\frac{dr}{dlnP} \qquad (1.12)$$

For our models, a mixing length parameter of 1.7 was determined by constraining models of the sun to the observed solar radius.

1.7 Outline of Thesis

This thesis describes our investigation of the asteroseismic properties of pre-main sequence (PMS) stars. PMS stars are young objects that are not fueled by core hydrogen burning, but rather by gravitational contraction and deuterium fusion. Because pulsation frequencies are highly dependent on stellar structure, we compute a densely populated array of models (section 2.1) to enable us to study oscillation spectra across the HR-diagram. Since the study of stellar evolution and pulsation has historically focused on post-main sequence models, we find it helpful to contrast our findings with post-main sequence models.

In chapter 2 we review the fundamental properties of PMS stars and compare them with post-main sequence models. We present the evolution of the internal structure in the context of its consequence to stellar pulsation. Following this, chapters 3 and 4 investigate the frequency spectra of PMS stars in detail by examining the large and small frequency separations across the HR diagram. In addition, the boundaries of the instability strip are constrained by identifying all models in the grid with driven modes.

We use the dense model grids to compute improved PMS isochrones in chapter 5. The dense grids enable our isochrones to resolve the "bump" caused by the burning of ^{12}C as PMS stars approach the ZAMS. Because PMS stars evolve rapidly, PMS isochrones are sensitive to effects that are not important in post-main sequence isochrones. The age of a PMS isochrone is sensitive to the zero age, but the lack of nuclear burning in PMS stars makes defining the zero age ambiguous. We estimate this uncertainty and include its effects in our isochrones. We use the new isochrones to explain features in photometry from two young open clusters.

Our ability to constrain properties of a star from its oscillation spectra is determined by the number of observed frequencies and their uncertainty. In chapter 6 we probe our ability to use asteroseismology to constrain stellar parameters of PMS stars. We accomplish this by constructing artificial "observed" oscillation spectra and match them to the dense model grids.

In chapter 7 we employ our dense model grids to constrain stellar properties of two PMS stars. Unlike the artificial oscillation spectra in chapter 6, real data may include false

detections due to instrumental effects or aliasing, and rotation can cause modes to split. We use the dense model grids to match to oscillation spectra from NGC 6530 85 and HD 104237.

Chapter 2

Model Characteristics

2.1 Pre-main Sequence Models

PMS models begin as fully convective spheres that gravitationally contract until nuclear burning begins on the zero age main sequence (ZAMS). On the way to the ZAMS, this evolutionary path takes PMS stars through the same region as evolving post-main stars, including the instability strip. Although the surface properties can be similar, pre- and post-main sequence stars have different internal structures. We study the internal structure of models to determine differences in pre- and post-main sequence oscillation spectra, and how the frequencies evolve with time.

The grids of PMS models were constructed using the Yale Stellar Evolution Code (YREC) (Guenther *et al.*, 1992), which solves the basic equations of stellar structure using the Henyey relaxation technique. The input physical data of the models include the OPAL98 (Iglesias & Rogers, 1996) and Alexander & Ferguson (1994) opacity tables, and the Lawrence Livermore equation of state tables. The mixing length parameter sets the temperature gradient in convective regions according to the Bohm-Vitense mixing length theory (Böhm-Vitense, 1958). All tracks were calculated with $\alpha = 1.8$, which was obtained from a solar

calibrated model constructed using the same input physical data as the pre-main sequence grid. The atmosphere is gray and computed with the Eddington approximation. Not included in these models are convective overshoot, rotation and gravitational settling of helium and heavy elements. The PMS grids that have been computed leave room for the inclusion of more advanced physics such as different convective models and mass loss, allowing for much more refined model exploration. It is possible that the including additional physics may have a significant effect on the calculated p-modes of the models.

The models are represented by approximately 2000 shells with a high concentration of shells in the atmosphere and outer envelope. The grid of PMS models comprises evolutionary tracks separated by 0.01 Msun, with approximately 800 models computed on each track. A grid of post-main sequence models was also constructed covering the same masses and using the same physics as the pre-main sequence calculations. The post-main sequence evolutionary tracks each comprise approximately 1500 models.

To explore the general properties of pre-main sequence stars, and for comparison with post-ZAMS models, it is not necessary or practical to examine all models in the computed grid. Thus, a subset of models were selected at 1.0, 2.0, 3.0, 4.0 and 5.0 $M_\odot$. The 1 $M_\odot$ evolutionary track is below the intermediate mass range but we include it for comparison and reference. Models chosen for comparison and detailed analysis are at key points in the evolutionary sequence that have approximately equivalent structure between adjacent evolutionary tracks. Figure 2.1 shows the positions of the selected models in the HR diagram and their associated evolutionary tracks. The models on each track are broken into three stages, marked by A, B, and C, which identify the Hayashi track, the horizontal
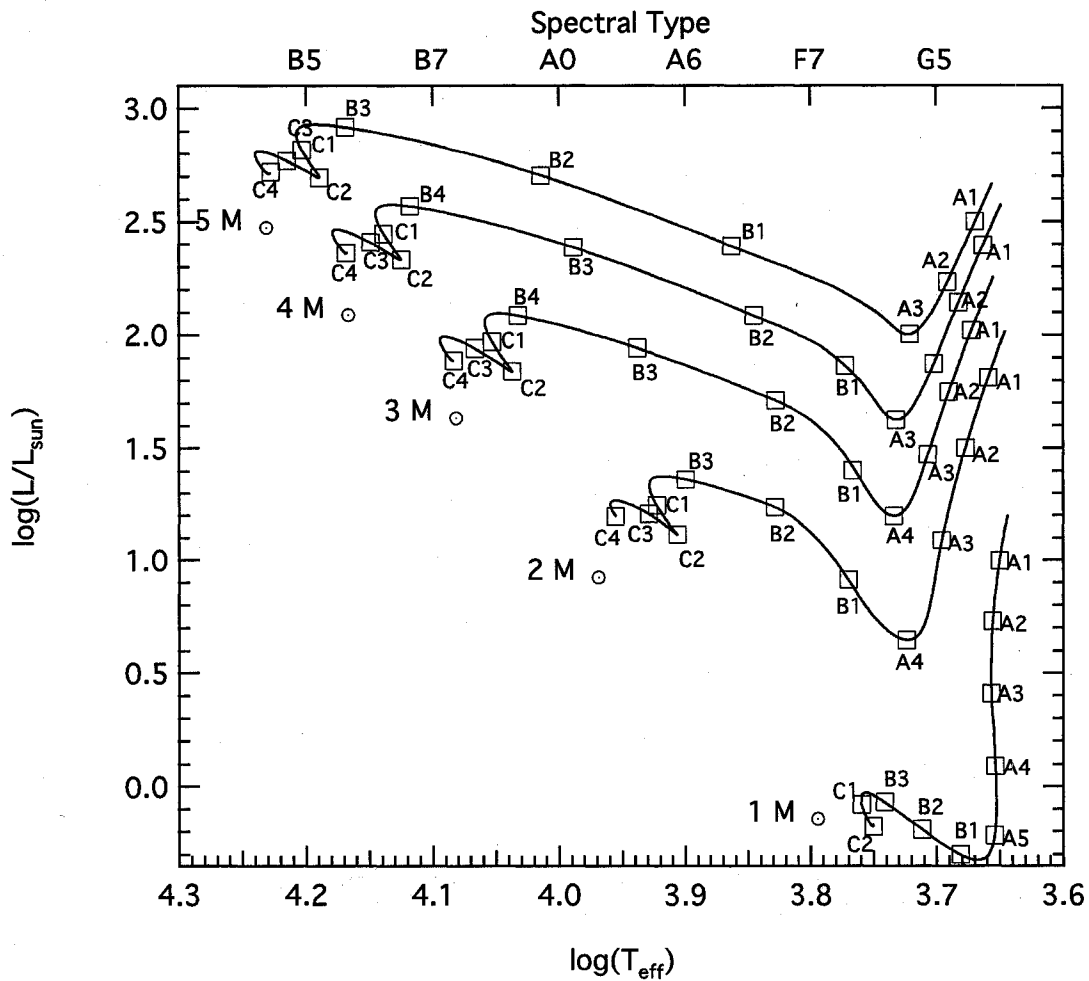
Figure 2.1 HR diagram of intermediate mass stars. Square symbols mark the sampling of models discussed in detail in forthcoming sections.

evolution phase and the approach to the ZAMS, respectively. We present properties of the models in figure 2.1 in table 2.1. In this chapter, we examine the fundamental properties of PMS models with different mass and age, as well as compare pre- and post-main sequence models of the same mass that share the same HR diagram position.

Each evolutionary sequence begins with a Lane-Emden polytropic sphere that is evolved from the Hayashi track and terminates at the ZAMS. Although most comparisons in the

following sections deal with models computed with metal and helium mass fraction abundances fixed at near solar values with $Z=0.02$ and $Y=0.27$, composition of elements heavier than helium (metals) is determined from scaling the observed solar composition of elements as described by Grevesse, Noels, & Sauval (1996). The effect of variations in metalicity and helium abundance is briefly examined in section 2.3 (refer to figures 2.11 and 2.12) and is not pursued further in this work.

The stellar evolution code calculates an appropriate time step according to various criteria and adjusts it between each pair of subsequent models in the evolution sequence. For pre-main sequence evolution, the code uses changes in luminosity and effective temperature. For main sequence evolution, the rate at which hydrogen abundance decreases in the core controls the time step and this results in an uneven distribution of models throughout a single evolutionary sequence, as well as different sets of model spacings for pre- and post-main sequence calculations.

For all evolutionary stages considered, the evolutionary time scale is considerably longer than typical pulsation periods (less than 5h for δ-Scuti stars) and growth rates. The pulsation of a star, being a hydrodynamic phenomenon, takes place on the hydrodynamic time scale, which is roughly equal to the sound crossing time. Therefore, it is prudent to assume that the pulsation modes will stabilize before stellar evolution can alter the structure of the star, which occurs on a nuclear time scale in post-main sequence stars, and on the Kelvin-Helmholtz time scale for PMS stars. This assumption permits the use of non-adiabatic and adiabatic pulsation analysis of a static model at any given stage in the evolution. Stellar rotation is not considered, and models are spherically symmetric and

in an equilibrium state, and the oscillations are assumed to be small allowing linearized equations to be used.

Adiabatic and non-adiabatic p-modes for $0 \leq l \leq 3$ and $0 \leq n \leq 20$ were calculated for all models in grid. The pulsation spectra were computed using the stellar pulsation code of Guenther (1994), which solves the linearized, non-radial, non-adiabatic pulsation equations using the Henyey relaxation method. The non-adiabatic solutions only include radiative energy gains and losses and do not include the effects of convection. Both the stellar evolution and pulsation calculations were carried out using computational facilities at the Institute for Computational Astrophysics and the Department of Astronomy and Physics at Saint Mary's University.

Table 2.1. Selected Model Structure Properties

Mass (M☉) (1)	Label (2)	Age (Gyr) (3)	$\log T_{eff}$ (4)	$\log L/L_\odot$ (5)	$\log R/R_\odot$ (6)	$\log g$ (7)	M_{cc} (8)	M_{cenv} (9)	X_{cenv} (10)	$\log P_c$ (11)	$\log T_c$ (12)	$\log \rho_c$ (13)
1.0	A1	0.000	3.652	0.927	0.684	3.070	0.000	1.000	0.000	13.248	6.212	-1.091
1.0	A2	0.000	3.656	0.656	0.539	3.359	0.000	1.000	0.000	13.813	6.353	-0.667
1.0	A3	0.001	3.656	0.384	0.403	3.632	0.000	1.000	0.000	14.348	6.487	-0.266
1.0	A4	0.002	3.654	0.110	0.272	3.894	0.000	0.985	0.138	14.867	6.615	0.123
1.0	A5	0.005	3.653	-0.183	0.126	4.186	0.000	0.682	0.411	15.500	6.737	0.635
1.0	B1	0.015	3.675	-0.314	0.016	4.406	0.000	0.254	0.588	16.336	6.881	1.325
1.0	B2	0.021	3.708	-0.205	0.006	4.426	0.000	0.118	0.639	16.749	6.969	1.649
1.0	B3	0.026	3.738	-0.084	0.007	4.424	0.000	0.060	0.672	17.024	7.043	1.848
1.0	C1	0.034	3.759	-0.086	-0.038	4.513	0.065	0.028	0.719	17.176	7.135	1.908
1.0	C2	0.054	3.750	-0.169	-0.062	4.561	0.028	0.033	0.719	17.155	7.130	1.893
2.0	A1	0.000	3.664	1.728	1.060	2.619	0.000	2.000	0.000	12.352	6.135	-1.912
2.0	A2	0.000	3.681	1.434	0.880	2.980	0.000	2.000	0.000	13.059	6.311	-1.383
2.0	A3	0.000	3.698	1.024	0.640	3.459	0.000	1.901	0.205	14.005	6.545	-0.670
2.0	A4	0.002	3.723	0.646	0.402	3.935	0.000	0.611	0.568	15.311	6.781	0.401
2.0	B1	0.004	3.767	0.884	0.433	3.873	0.000	0.055	0.730	16.087	6.940	1.018
2.0	B2	0.006	3.826	1.229	0.487	3.765	0.000	0.000	0.962	16.722	7.102	1.490
2.0	B3	0.006	3.899	1.361	0.406	3.926	0.002	0.000	0.991	17.044	7.208	1.705
2.0	C1	0.007	3.923	1.245	0.301	4.137	0.418	0.000	0.995	17.054	7.269	1.654
2.0	C2	0.008	3.907	1.118	0.269	4.200	0.271	0.000	0.992	17.045	7.267	1.647
2.0	C3	0.008	3.932	1.216	0.268	4.203	0.110	0.000	0.992	17.158	7.285	1.742
2.0	C4	0.012	3.955	1.197	0.211	4.316	0.233	0.000	0.994	17.268	7.323	1.814
3.0	A1	0.000	3.672	2.021	1.190	2.534	0.000	3.000	0.000	12.177	6.176	-2.131
3.0	A2	0.000	3.691	1.737	1.011	2.894	0.000	2.999	0.037	12.885	6.353	-1.600
3.0	A3	0.000	3.708	1.454	0.835	3.244	0.000	2.304	0.361	13.598	6.512	-1.046
3.0	A4	0.001	3.733	1.197	0.656	3.604	0.000	0.736	0.601	14.679	6.711	-0.162
3.0	B1	0.002	3.769	1.438	0.706	3.504	0.000	0.024	0.798	15.380	6.854	0.396
3.0	B2	0.002	3.845	1.751	0.710	3.496	0.000	0.000	0.990	16.022	7.012	0.880
3.0	B3	0.002	3.931	1.929	0.627	3.662	0.000	0.000	0.990	16.428	7.119	1.179
3.0	B4	0.002	4.024	2.078	0.515	3.885	0.000	0.000	0.991	16.845	7.243	1.471
3.0	C1	0.003	4.052	1.966	0.402	4.111	0.692	0.000	0.995	16.892	7.318	1.442
3.0	C2	0.003	4.037	1.840	0.370	4.176	0.517	0.000	0.995	16.884	7.318	1.433
3.0	C3	0.003	4.062	1.928	0.363	4.188	0.229	0.000	0.993	17.001	7.338	1.531
3.0	C4	0.007	4.084	1.889	0.301	4.314	0.567	0.000	0.991	17.115	7.380	1.604
4.0	A1	0.000	3.675	2.237	1.292	2.456	0.000	3.992	0.068	12.021	6.195	-2.309
4.0	A2	0.000	3.692	2.010	1.144	2.752	0.000	3.277	0.326	12.615	6.332	-1.852

Table 2.1 (cont'd)

Mass $(M_\odot)$ (1)	Label (2)	Age (Gyr) (3)	$\log T_{eff}$ (4)	$\log L/L_\odot$ (5)	$\log R/R_\odot$ (6)	$\log g$ (7)	M_{cc} (8)	M_{cenv} (9)	X_{cenv} (10)	$\log P_c$ (11)	$\log T_c$ (12)	$\log \rho_c$ (13)
4.0	A3	0.000	3.709	1.782	0.996	3.048	0.000	2.117	0.483	13.276	6.472	-1.330
4.0	A4	0.000	3.732	1.626	0.874	3.293	0.000	0.669	0.647	14.100	6.633	-0.665
4.0	B1	0.001	3.787	1.931	0.916	3.208	0.000	0.000	0.914	15.054	6.838	0.085
4.0	B2	0.001	3.892	2.191	0.836	3.368	0.000	0.000	0.988	15.656	6.985	0.539
4.0	B3	0.001	4.011	2.427	0.715	3.611	0.000	0.000	0.990	16.237	7.138	0.968
4.0	B4	0.001	4.108	2.561	0.589	3.862	0.000	0.000	0.992	16.688	7.268	1.288
4.0	C1	0.001	4.138	2.445	0.470	4.101	0.989	0.000	0.997	16.768	7.350	1.283
4.0	C2	0.001	4.125	2.332	0.440	4.161	0.774	0.000	0.997	16.765	7.352	1.278
4.0	C3	0.001	4.149	2.408	0.430	4.180	0.369	0.000	0.994	16.880	7.373	1.372
4.0	C4	0.004	4.167	2.362	0.371	4.297	0.880	0.000	0.992	16.987	7.412	1.442
5.0	A1	0.000	3.670	2.485	1.425	2.286	0.000	4.635	0.231	11.686	6.152	-2.604
5.0	A2	0.000	3.696	2.184	1.224	2.689	0.000	2.774	0.468	12.562	6.340	-1.914
5.0	A3	0.000	3.722	2.006	1.082	2.973	0.000	0.666	0.662	13.510	6.541	-1.164
5.0	B1	0.000	3.818	2.298	1.037	3.063	0.000	0.000	0.988	14.776	6.820	-0.177
5.0	B2	0.000	3.929	2.539	0.935	3.267	0.000	0.000	0.986	15.377	6.966	0.278
5.0	B3	0.001	4.046	2.763	0.814	3.510	0.000	0.000	0.989	15.963	7.118	0.712
5.0	B4	0.001	4.160	2.913	0.661	3.815	0.000	0.000	0.993	16.520	7.273	1.113
5.0	C1	0.001	4.203	2.814	0.525	4.086	1.286	0.000	0.998	16.676	7.374	1.165
5.0	C2	0.001	4.190	2.698	0.494	4.149	1.110	0.000	0.999	16.668	7.376	1.155
5.0	C3	0.001	4.216	2.774	0.479	4.178	0.492	0.000	0.996	16.801	7.402	1.262
5.0	C4	0.003	4.228	2.717	0.426	4.285	1.184	0.000	0.992	16.889	7.435	1.319

Note. — Col. (1): Mass; Col. (2): Label of the evolutionary state; Col. (3): Age; Col. (4): The log of the effective temperature; Col. (5): The log of the luminosity; Col. (6): The log of the radius; Col. (7): The log of the surface gravity; Col. (8): Mass of the convective core; Col. (9): Mass of the convective envelope; Col. (10): Radius fraction location of the base of the convective envelope; Col. (11): The log of the central pressure; Col. (12): The log of the central temperature; Col. (13): The log of the central density.

2.2 Density, Pressure, Temperature, Luminosity

We review the fundamental internal properties of our PMS models. Our results are consistent with Iben (1965). For comparison and general reference we provide plots of the interior structure of 1 and 3 $M_\odot$ models.

Figures 2.2 and 2.3 show the evolution of density for 1 and 3 $M_\odot$ models, respectively. Likewise, figures 2.4 and 2.5 show the evolution of pressure, while figures 2.6 and 2.7 show the evolution of temperature. Similarly, figures 2.8 and 2.9 show the evolution of luminosity, including nuclear and gravitational power but excluding neutrino power. These basic quantities are presented at the selected models of evolutionary sequences shown in figure 2.1 for the 1 and 3 $M_\odot$ evolutionary tracks.

The structural evolution of the 1 $M_\odot$ star is very similar to that of the 3 $M_\odot$ star. The primary difference between the 1 and 3 $M_\odot$ evolutionary tracks is the structural correction caused by ^{12}C burning prior to reaching the ZAMS which Iben (1965) identified as a consequence of the ignition of CNO burning. Because nuclear burning is not the dominant source of energy in PMS stars, the composition remains largely unchanged. This means that steep μ-gradients do not develop, so the structure is not significantly altered at any point during the evolution. As the star evolves, the core becomes more centrally concentrated, and the simple structure preserves the smooth and continuous profiles.

During Hayashi track contraction, gravity generates all power. The PMS polytropes begin evolution as completely convective envelopes and as figure 2.10 shows, the convective en-

velope mass is equal to, or nearly so, to the stellar mass throughout most of the evolution down the Hayashi track.

2.3 Convective Regions

The presence of convective regions in stars is important to examine because non-radial p-mode oscillations are believed to be driven by convective turbulence. For this reason, stars with convective envelopes are of particular interest for their possibility of exhibiting driven p-mode oscillations.

In figure 2.10 we show the evolution of convective envelopes and cores with age for the selected evolutionary tracks in figure 2.1. The models are initially completely convective and proceed to develop radiative cores as they contract and the central density grows. As the stars evolve, the temperature increases until the interior opacities decrease and the convective envelope shrinks (or, rather, a radiative core grows).

Stellar structure is heavily influenced by H- opacity throughout the early stages of PMS evolution. Further, the evolution of the convective envelope is sensitive to the metal abundance, which contributes to the H- opacity through the increased availability of electrons provided by ionization. Increasing the metal abundance results in increased opacity, effectively prolonging the life of the convective envelope in PMS evolution. We confirm this in figure 2.11, which shows the mass of the convective envelope as a function of age for the 3 $M_\odot$ evolutionary track at Z=0.01, Z=0.02 and Z=0.04 metal abundances. Increasing the
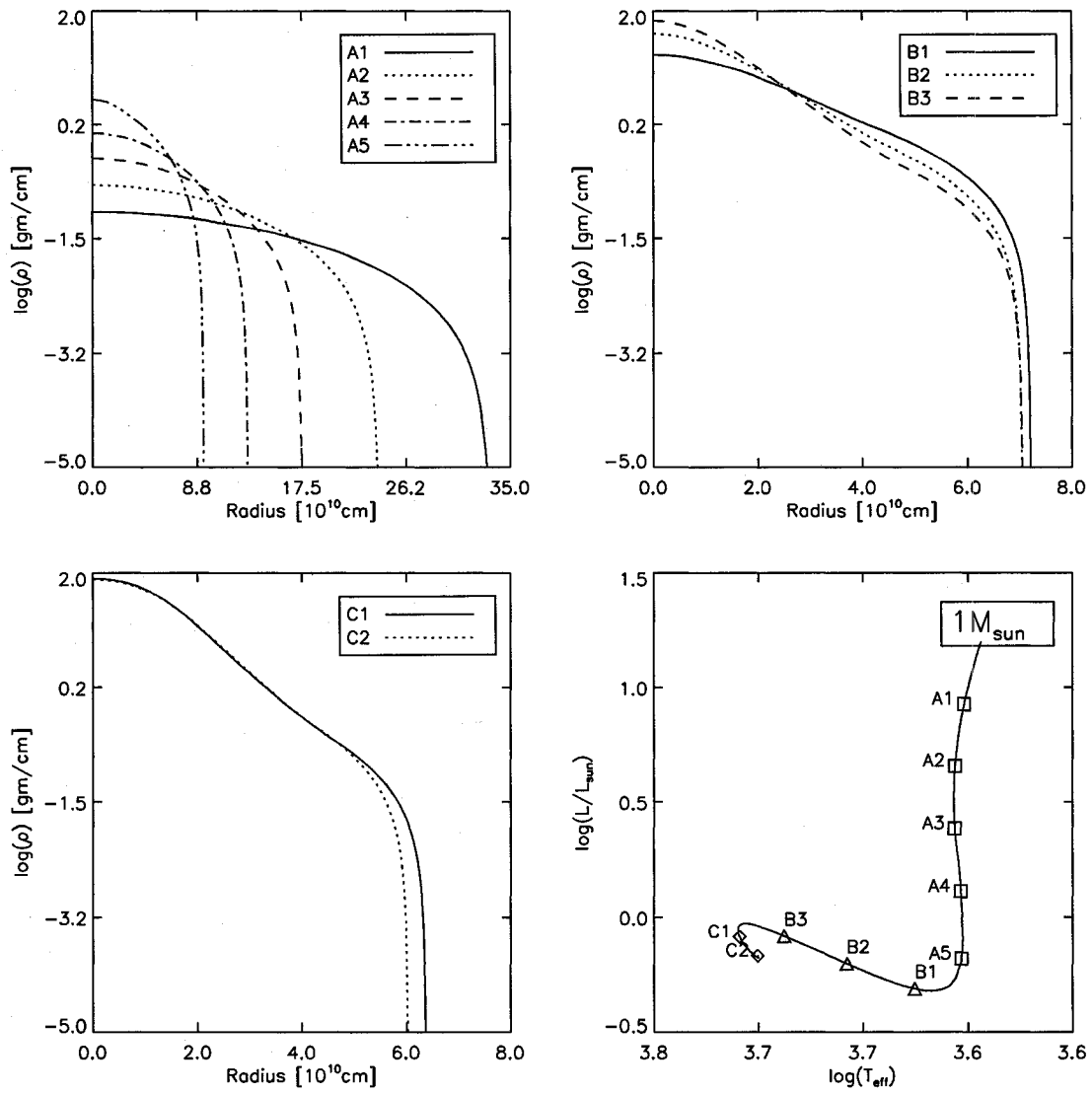
Figure 2.2 Density as a function of radius for a 1 M$_\odot$ evolutionary track.
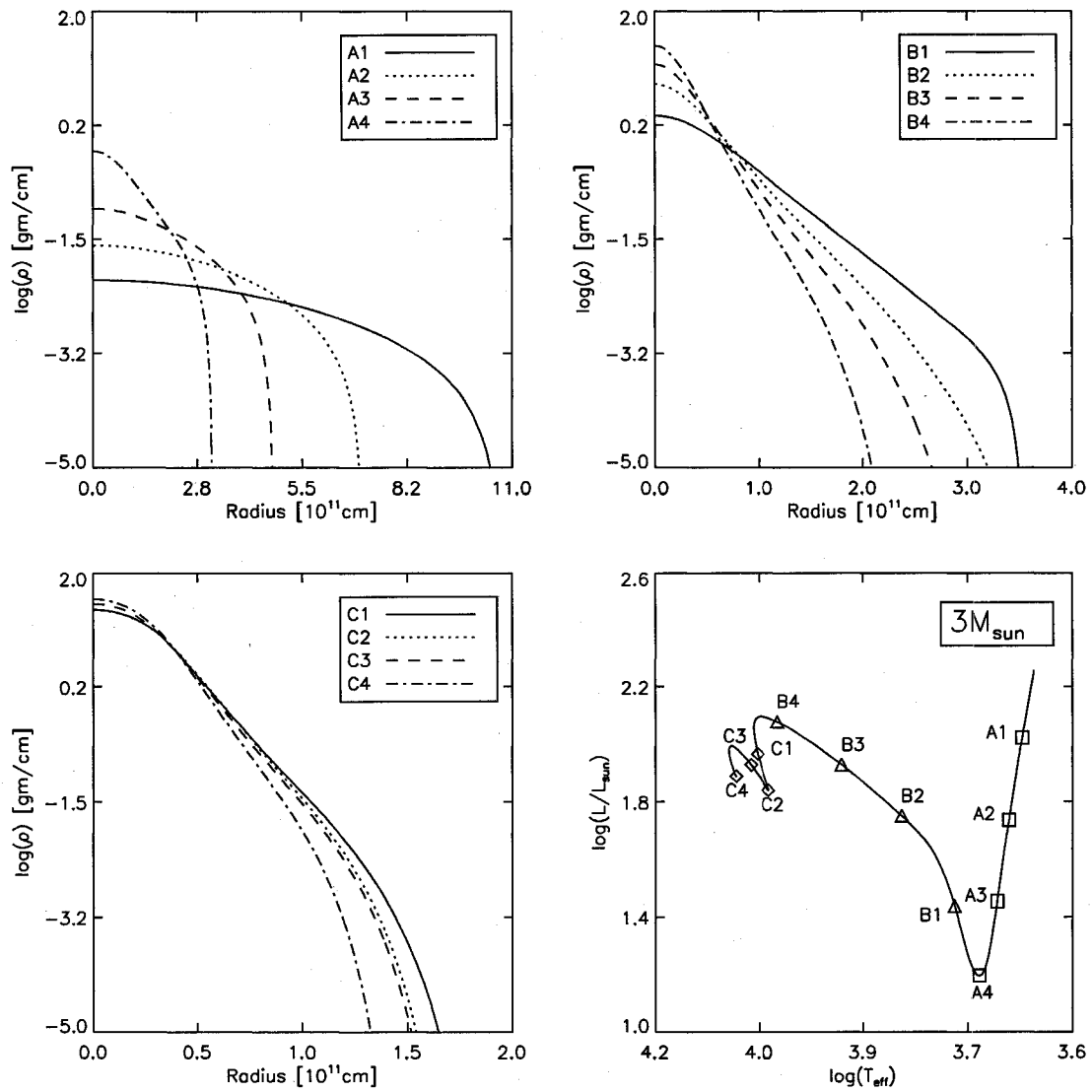
Figure 2.3 Density as a function of radius for a 3 $M_\odot$ evolutionary track.
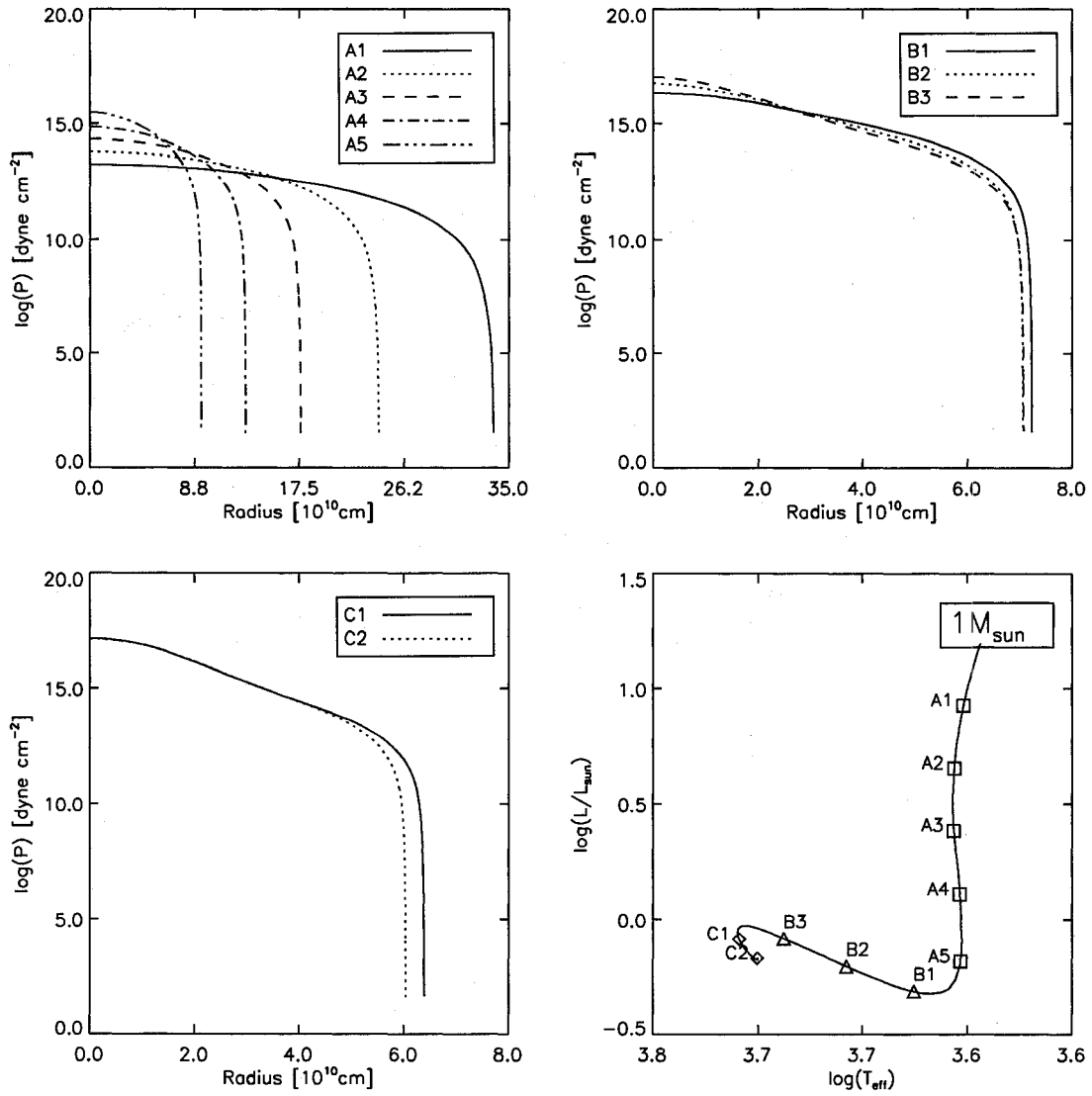
Figure 2.4 Pressure as a function of radius for a 1 M$_\odot$ evolutionary track.
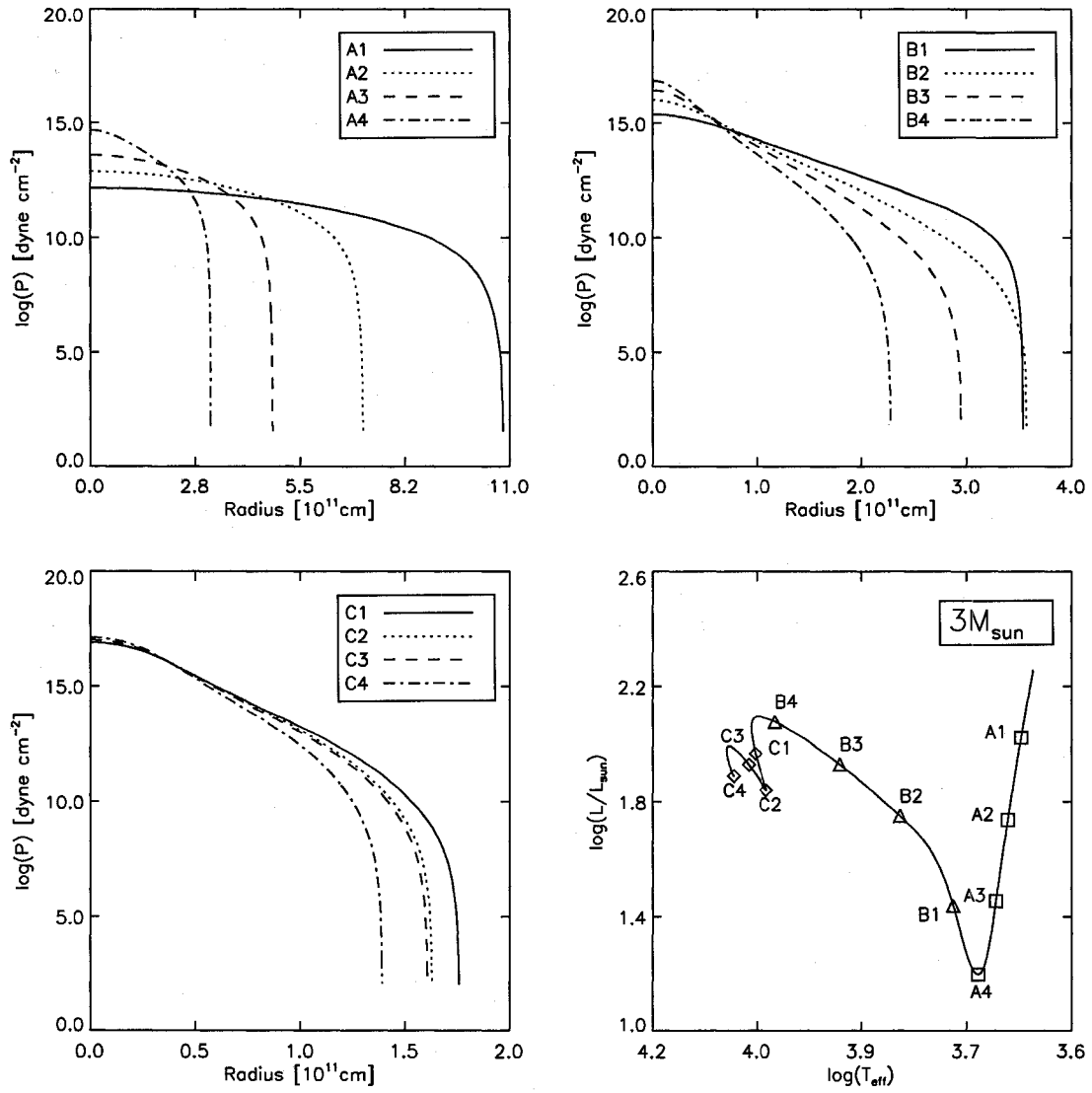
Figure 2.5 Pressure as a function of radius for a 3 $M_\odot$ evolutionary track.
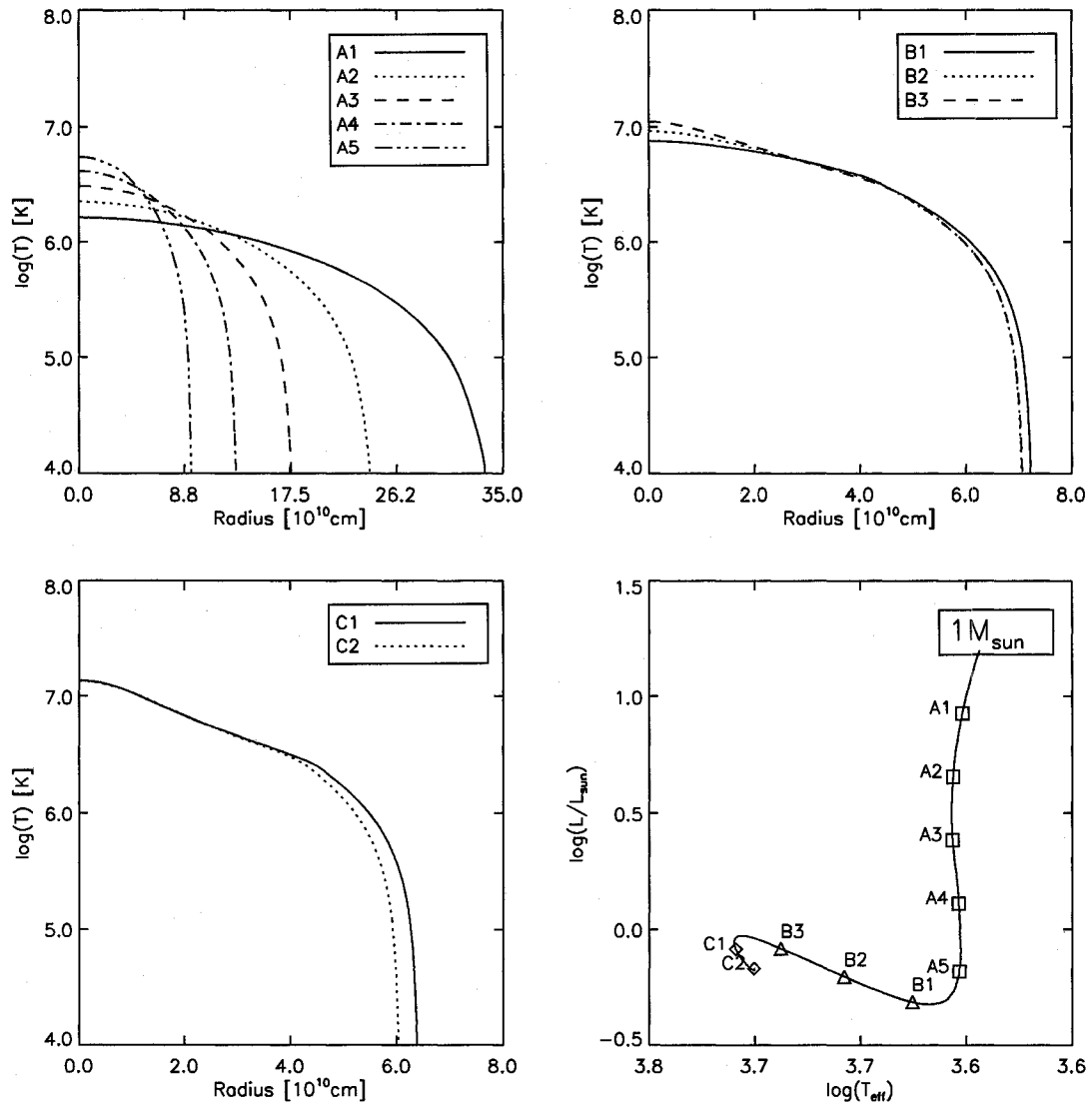
Figure 2.6 Temperature as a function of radius for a 1 M$_\odot$ evolutionary track.
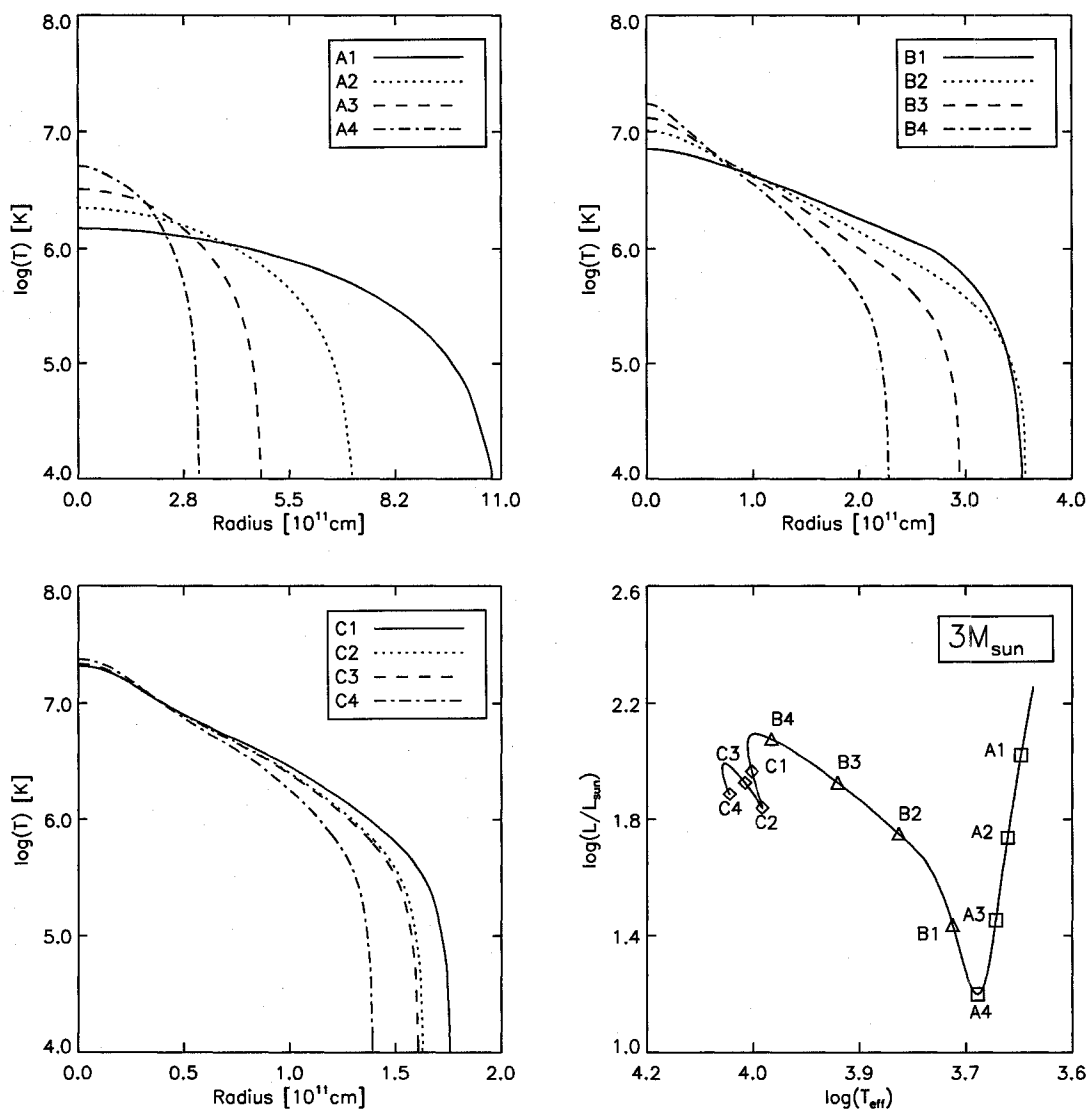
Figure 2.7 Temperature as a function of radius for a 3 $M_\odot$ evolutionary track.
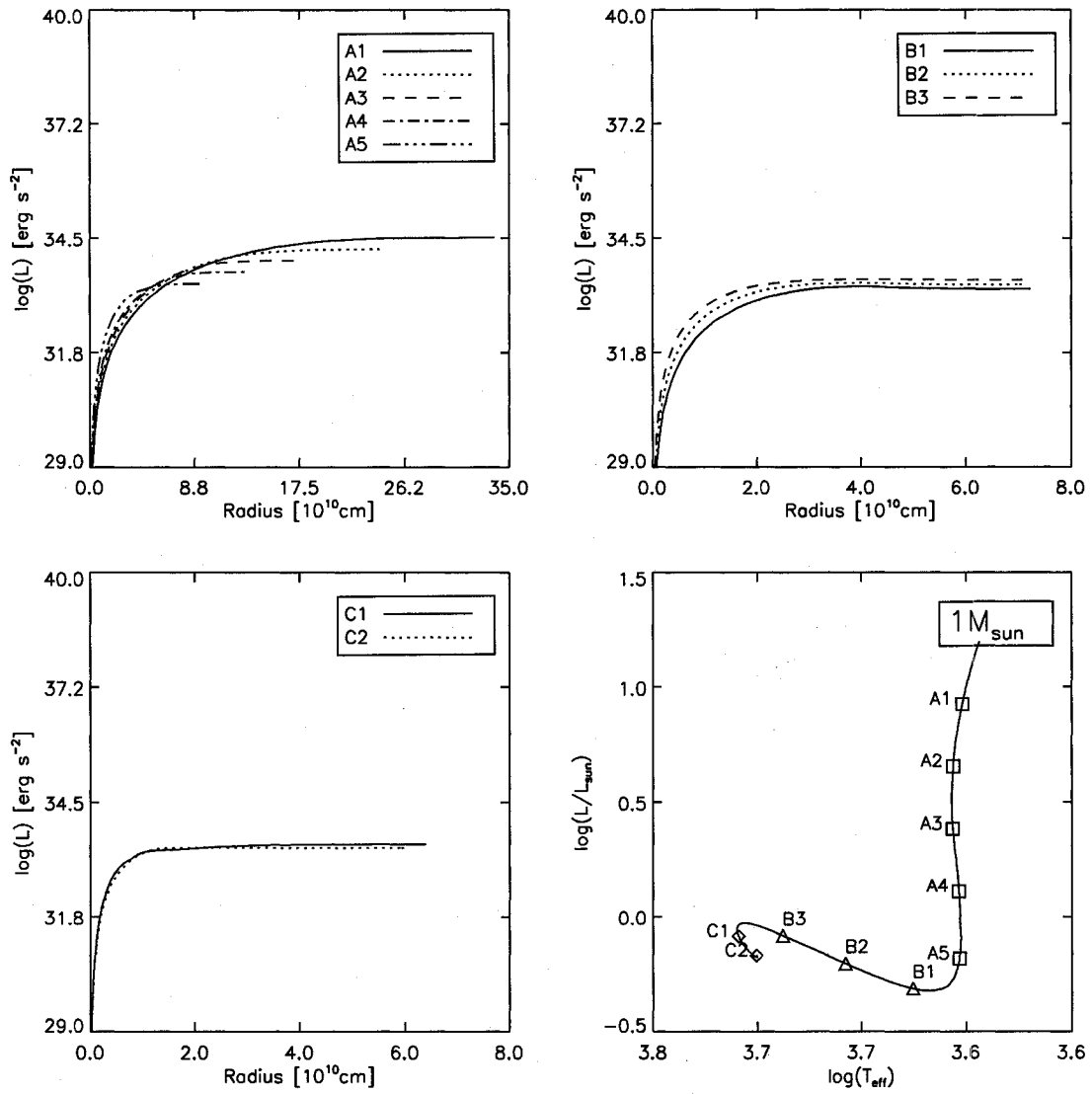
Figure 2.8 Luminosity as a function of radius for a 1 M$_\odot$ evolutionary track.
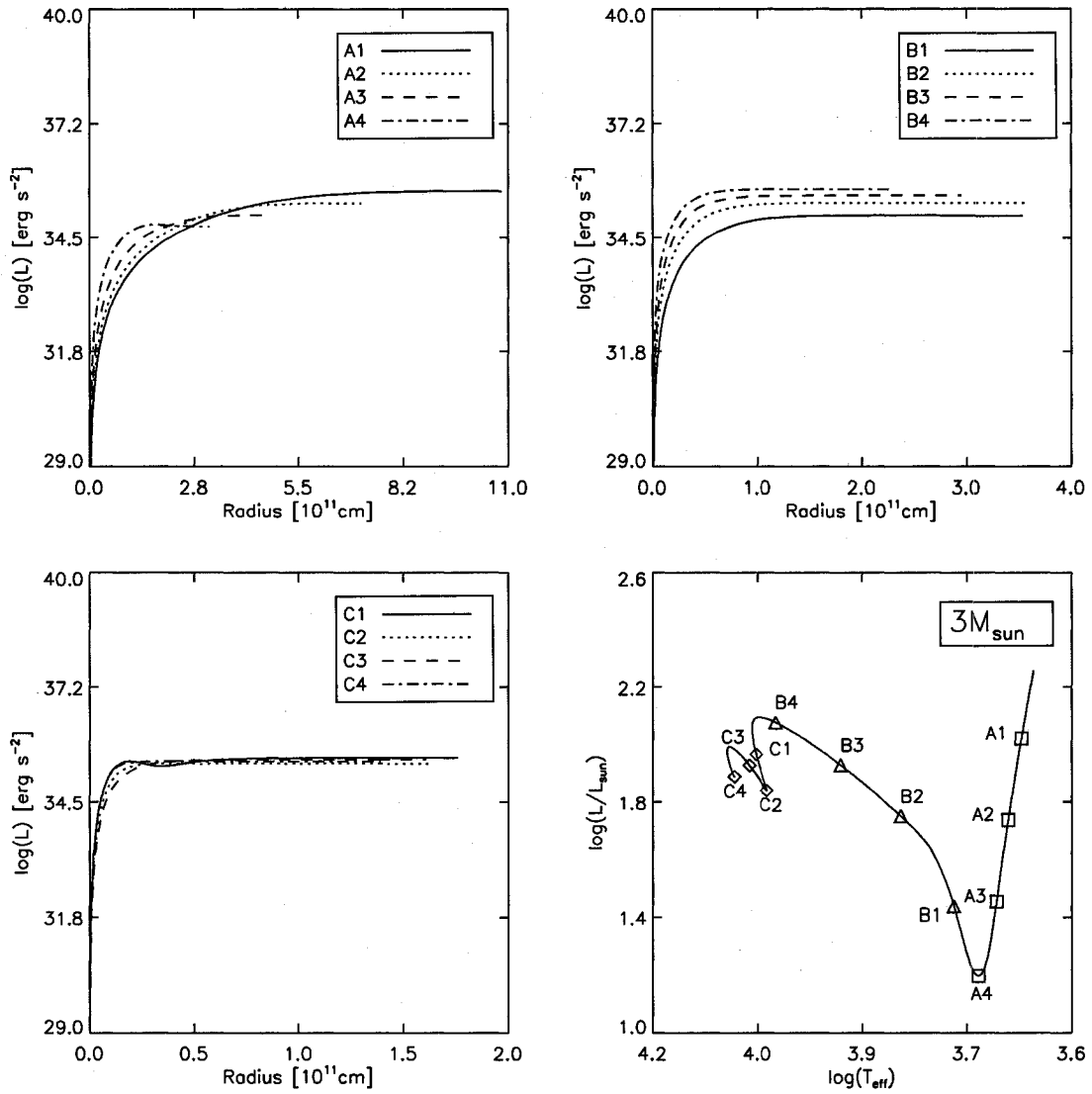
Figure 2.9 Luminosity as a function of radius for a 3 $M_\odot$ evolutionary track.

metalicity from Z=0.01 to Z=0.02, and from Z=0.02 to Z=0.04 prolongs the existence of the convective envelope by a factor of about 12% of the PMS evolution time to the ZAMS. Likewise, the increased metalicity delays the onset of development of a convective core. Decreasing the hydrogen abundance (figure 2.12) also results in a prolonged convective envelope and delays the onset of the convective core.

P-mode frequencies are sensitive to the cores in post-main sequence stars because the cores are altered by nuclear burning. Because the primary energy source of pre-main sequence stars is not nuclear burning, the models are nearly completely homogeneous. This means that the effect of convective cores in pre-main sequence stars is minimized.

2.4 Mean Molecular Weight, Adiabatic Gamma 1, Sound Speed

Stellar pulsation is more sensitive to the mean molecular weight and adiabatic exponent than to the fundamental quantities of stellar evolution discussed in section 2.2. These quantities experience significant changes in the outer regions of the star where p-modes are most sensitive.

The mean molecular weight is the average mass of all the atomic particles, including electrons, and is expressed in units of the proton mass. In stellar interiors where hydrogen and helium are completely ionized, the mean molecular weight is $\mu \approx 0.60$, while nearer the surface, μ undergoes changes due to variations in the number fractions of electrons,
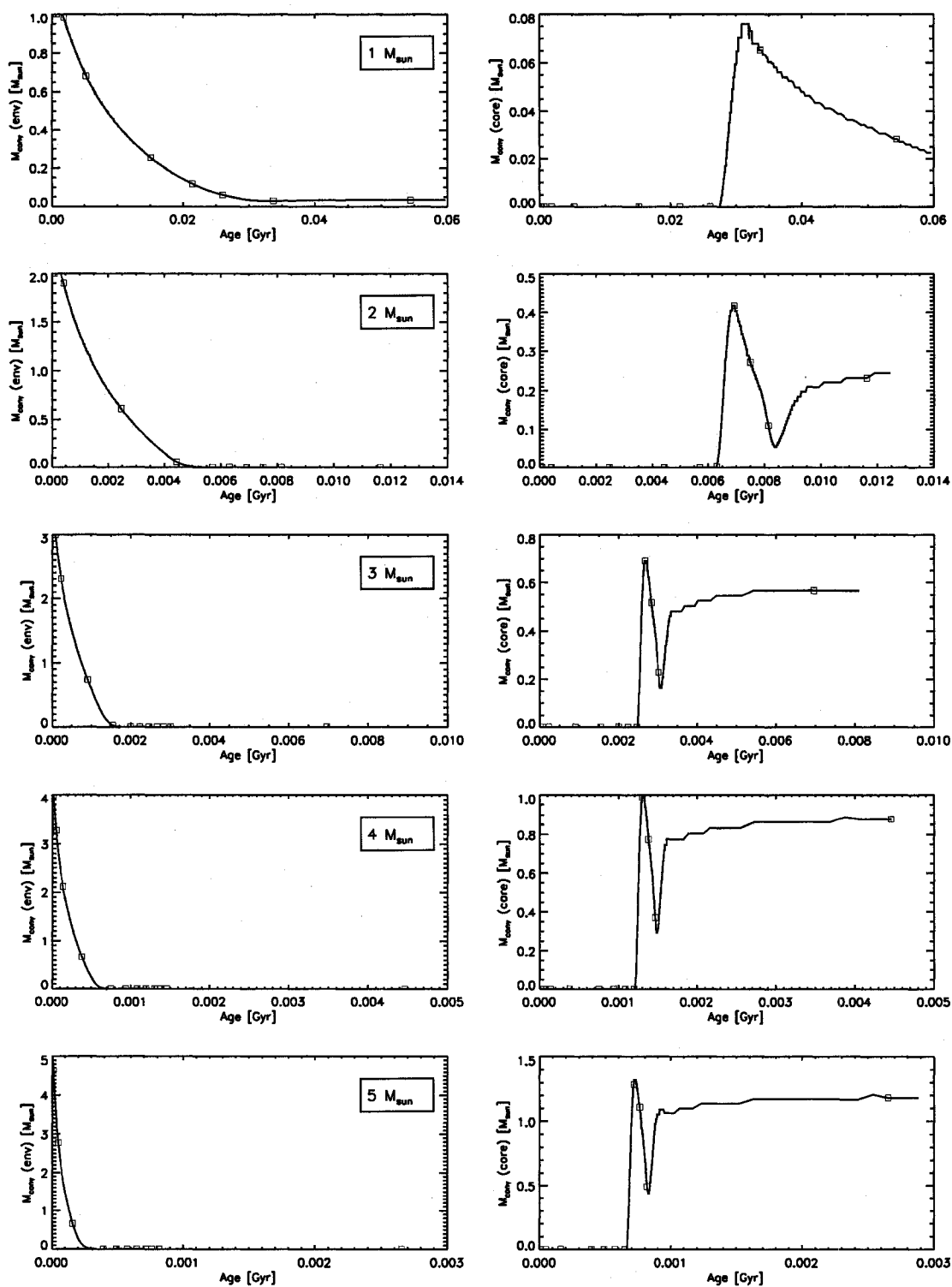
Figure 2.10 Convective envelope mass (left hand side) and convective core mass (right hand side) as functions of age corresponding to evolutionary tracks shown in figure 2.1. Squares indicate models that have properties listed in table 2.1.
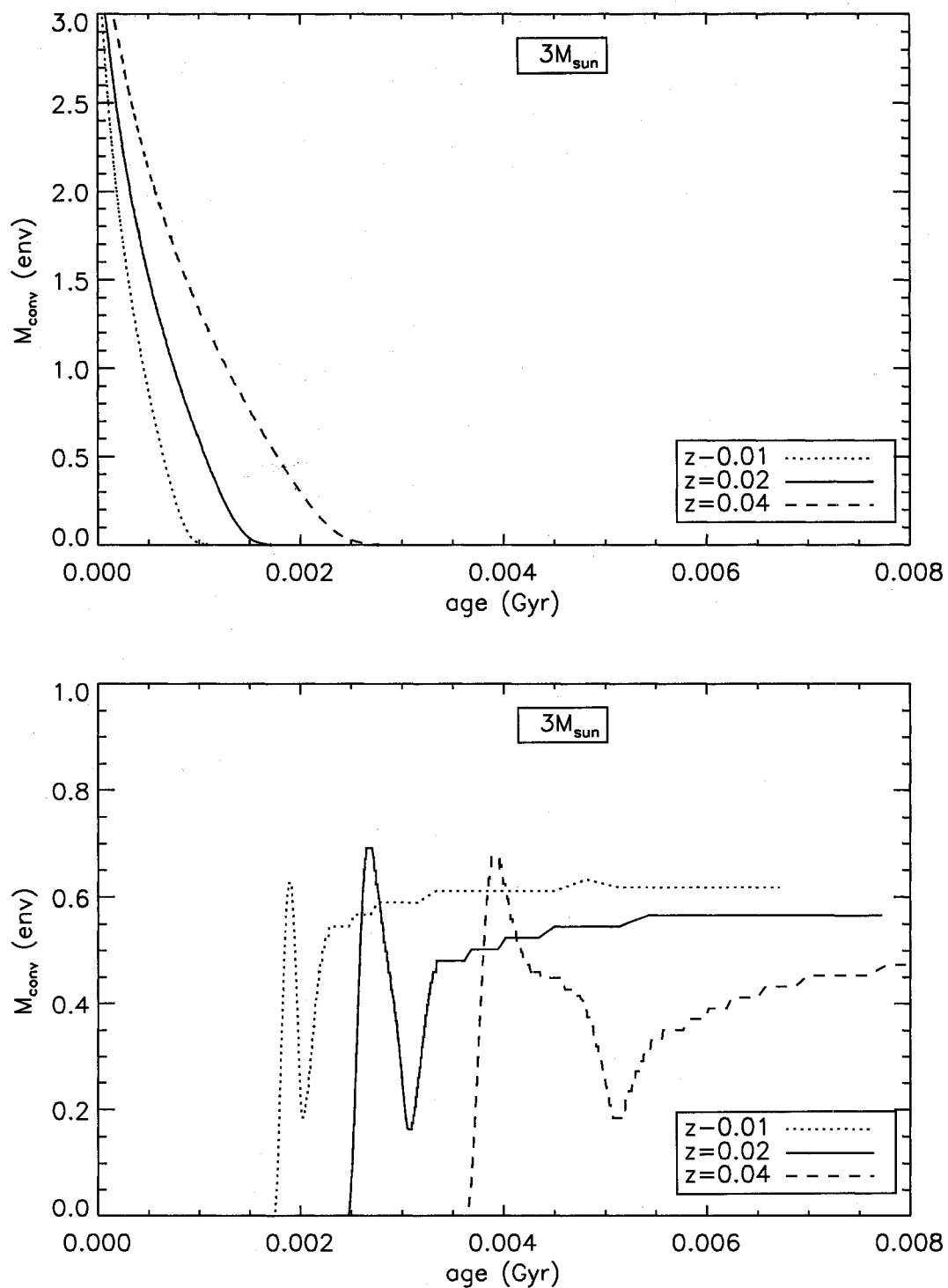
Figure 2.11 Convective envelope mass (top) and convective core mass (bottom) as functions of age for three metal abundances for a 3 M$_\odot$ evolution sequence.
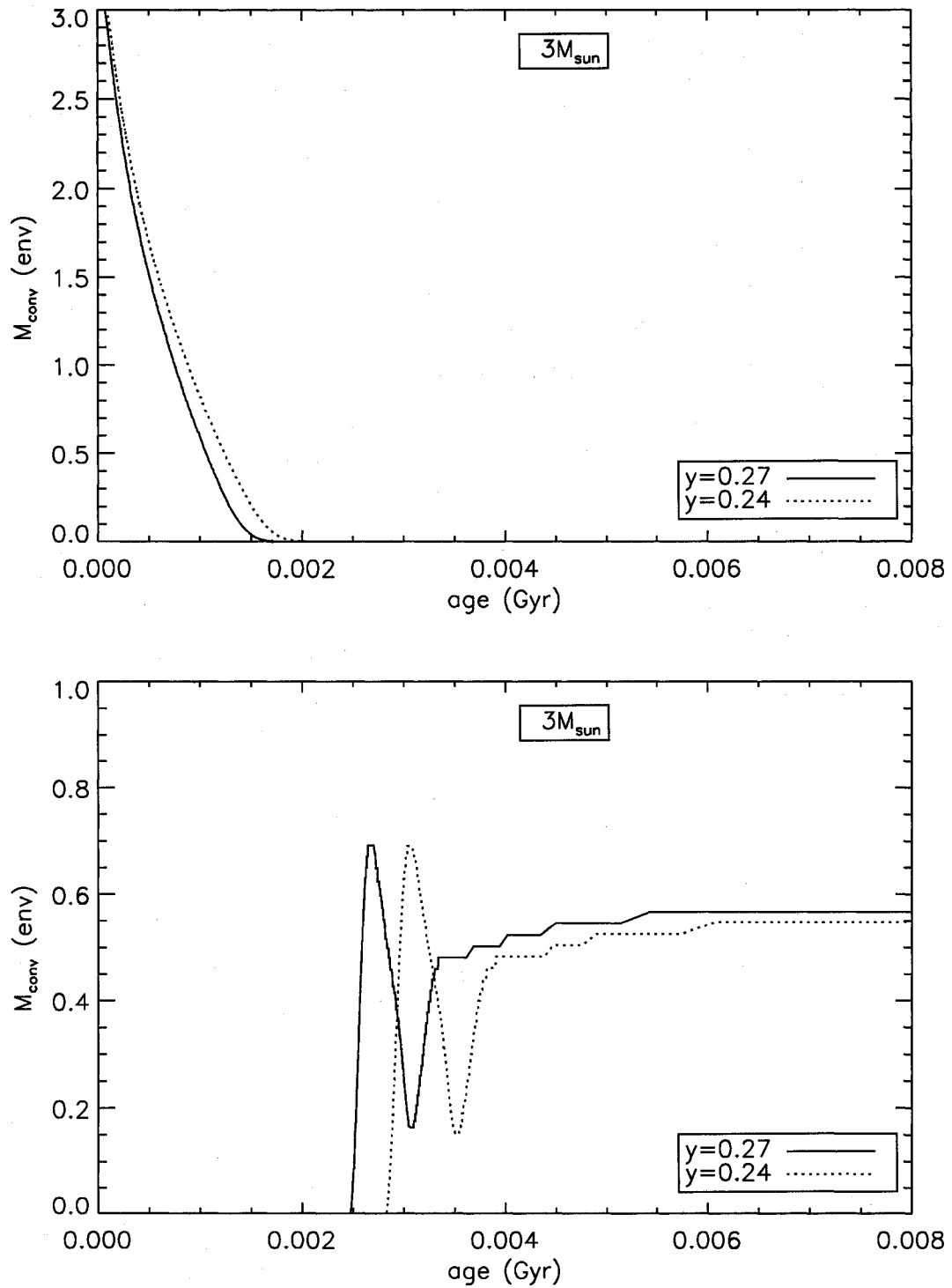
Figure 2.12 Convective envelope mass (top) and convective core mass (bottom) as functions of age for two hydrogen abundances for a 3 $M_\odot$ evolution sequence.

particularly in H and He ionization regions. Mean molecular weight is shown as a function of radius in figures 2.13 and 2.14. The rising mean molecular weight is a result of decreasing number of electrions in regions where H and He re-combine. The ionization regions occur at T=18,000 K and T=42,000 K for He, and T=10,000 for H. Recombination of H does not effect models with surface temperatures in excess of 10,000 K.

The adiabatic exponent is the logarithmic derivative of pressure with respect to density at constant entropy $[\partial \ln p / \partial \ln \rho]_S$. In the stellar interior of pre-main sequence stars, the measure remains relatively constant at 5/3, but changes significantly in regions approaching the surface where the variations occur alongside the changes in mean molecular weight. Figures 2.15 and 2.16 show the adiabatic exponent as a function of radius in the outermost regions of 1 and 3 $M_\odot$ models, respectively.

The adiabatic sound speed depends on the mean molecular weight and the adiabatic exponent according to the following relation:

$$c^2 = \frac{\Gamma_1 P}{\rho} = \frac{k_B T}{\mu m_H}. \tag{2.1}$$

where k_B is the Boltzmann constant, μ is the mean molecular weight, and m_H is the atomic weight of Hydrogen.. The sound speed decreases near the surface of the star and because p-mode frequencies are (to first order) proportional to sound speed according to $\nu \propto \left(\int \frac{dr}{c} \right)^{-1}$, the decreasing sound speed near the surface contributes more to the integral, which results in p-modes being more sensitive to the outer layers of the star. Even small variations in sound speed near the surface can significantly affect the p-mode frequencies.

Figures 2.17 and 2.18 demonstrate that the sound speed decreases from the center of the star outward. Unlike their post-main sequence counterparts, pre-main sequence stars do not experience a hydrogen burning shell, which preserves the smooth variation with radius throughout the entire star.

2.5 The Brunt-Väisälä and Lamb Frequencies

Examining the Brunt-Väisälä (N) and Lamb (L) frequencies reveals many oscillation properties and leads to a better understanding of the properties of the host star. Proportional to the fundamental buoyancy frequency at a given depth of the star, N corresponds to the oscillation frequency of a displaced fluid element that oscillates adiabatically about its equilibrium position. In convective regions a perturbed fluid element cannot oscillate, but continues rising or falling instead, with the displacement from the original position growing exponentially in time. Under such circumstances N^2 is negative, which results in an imaginary frequency. L is the frequency of a horizontal acoustic wave with wavelength $2\pi r/l$. In regions where the oscillation frequency is greater than both the L and N, p-modes can propagate, and likewise in regions where the oscillation frequency is less than both L and N, g-modes can propagate. P-modes and g-modes are evanescent in all other regions.

The Brunt-Väisälä and Lamb frequencies are given by:

$$N^2 = g(1/H - g/c^2), \tag{2.2}$$
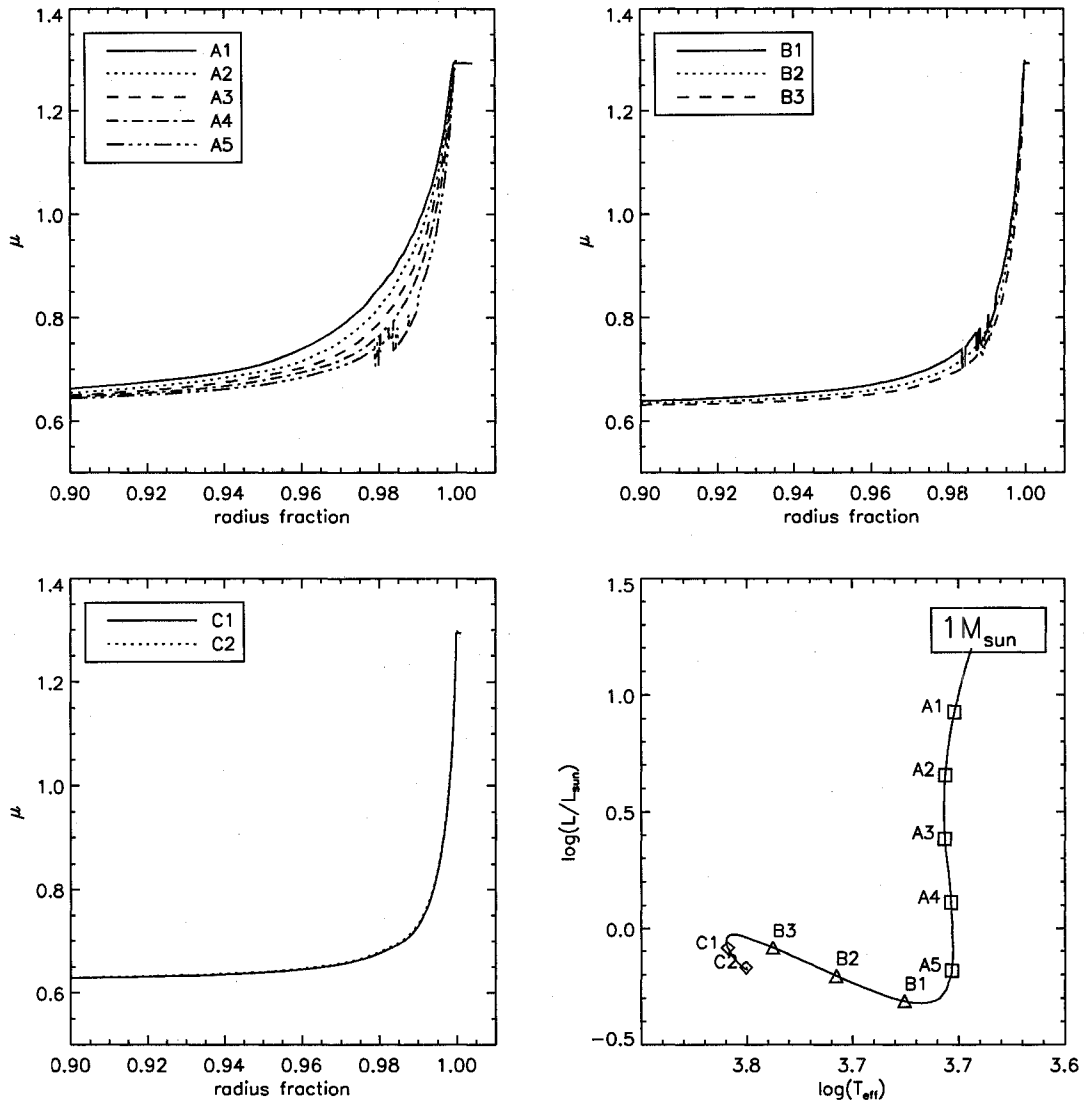
Figure 2.13 Mean molecular weight as a function of radius for a 1 $M_{\odot}$ evolutionary track.
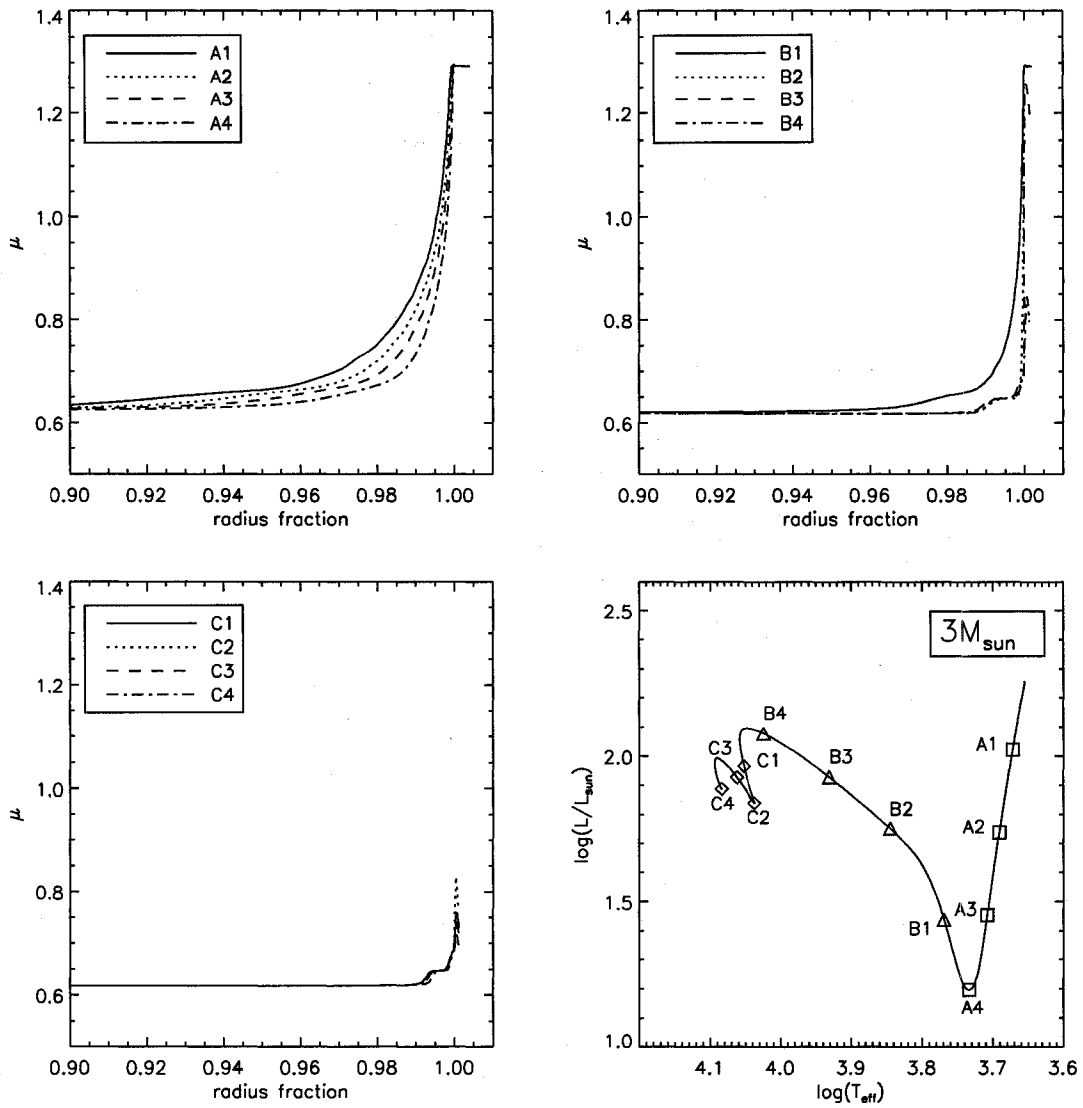
Figure 2.14 Mean molecular weight as a function of radius for a 3 M$_\odot$ evolutionary track.
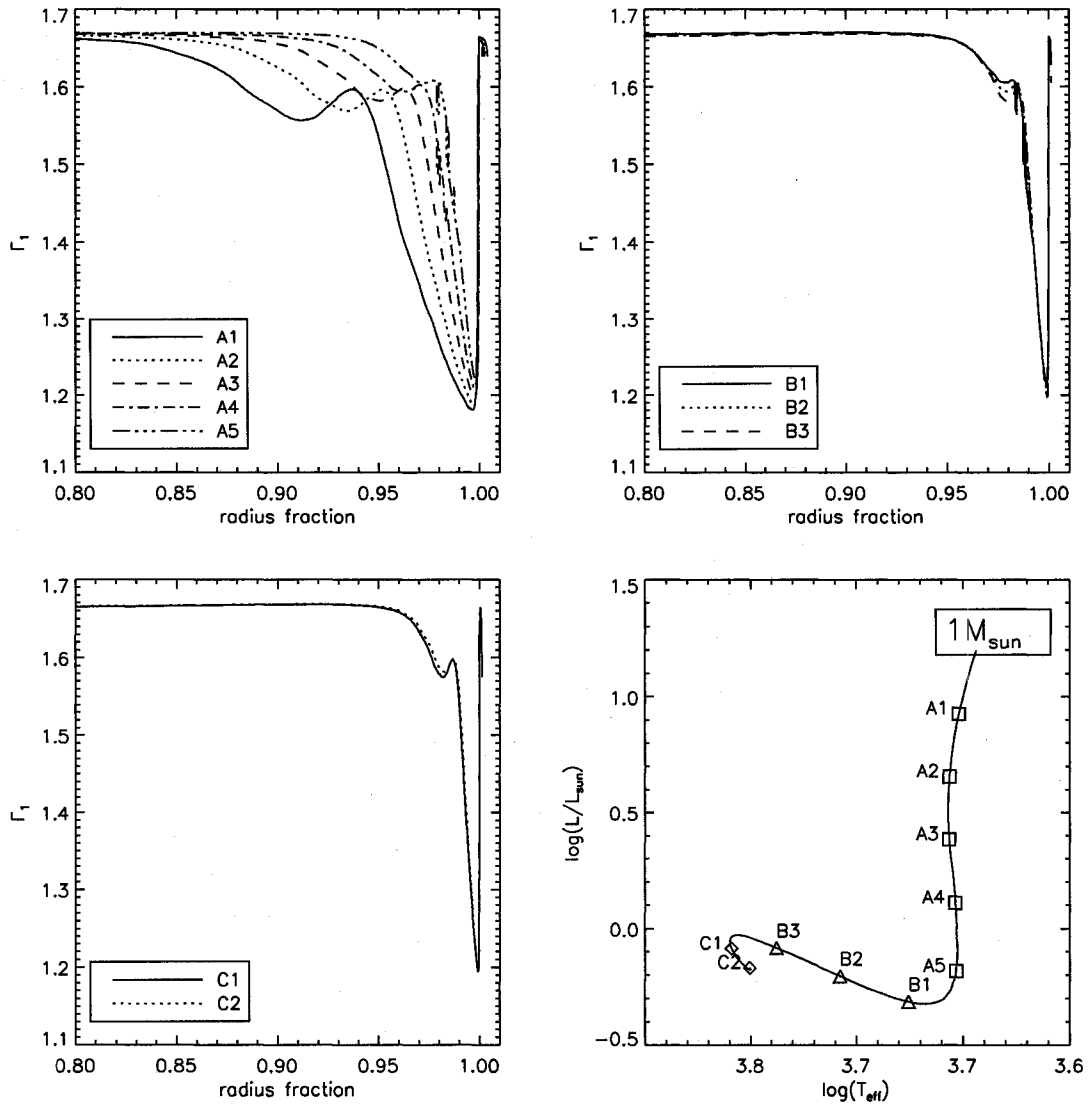
Figure 2.15 Adiabatic Γ_1 as a function of radius for a 1 $M_\odot$ evolutionary track.
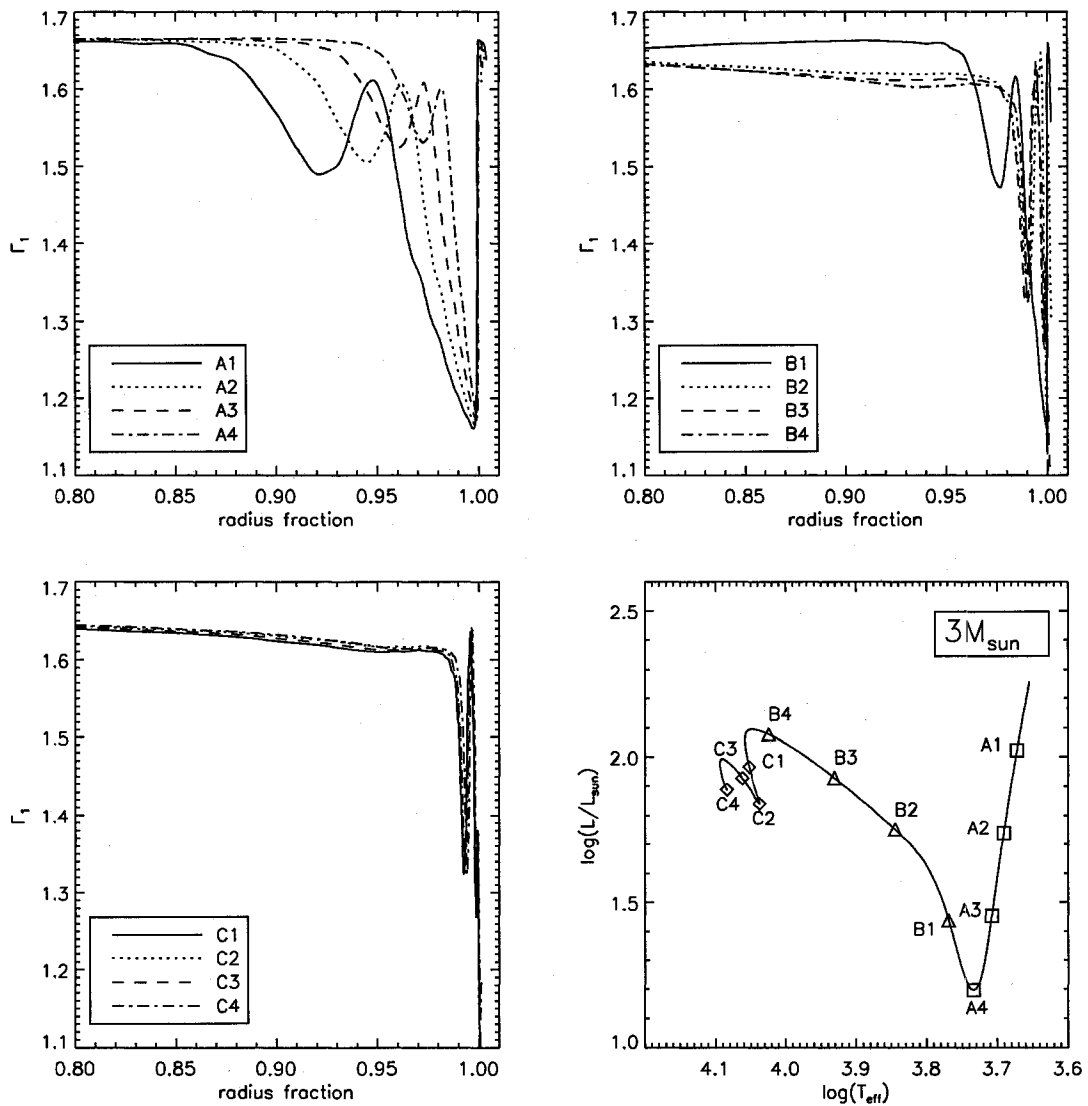
Figure 2.16 Adiabatic Γ_1 as a function of radius for a 3 $M_\odot$ evolutionary track.
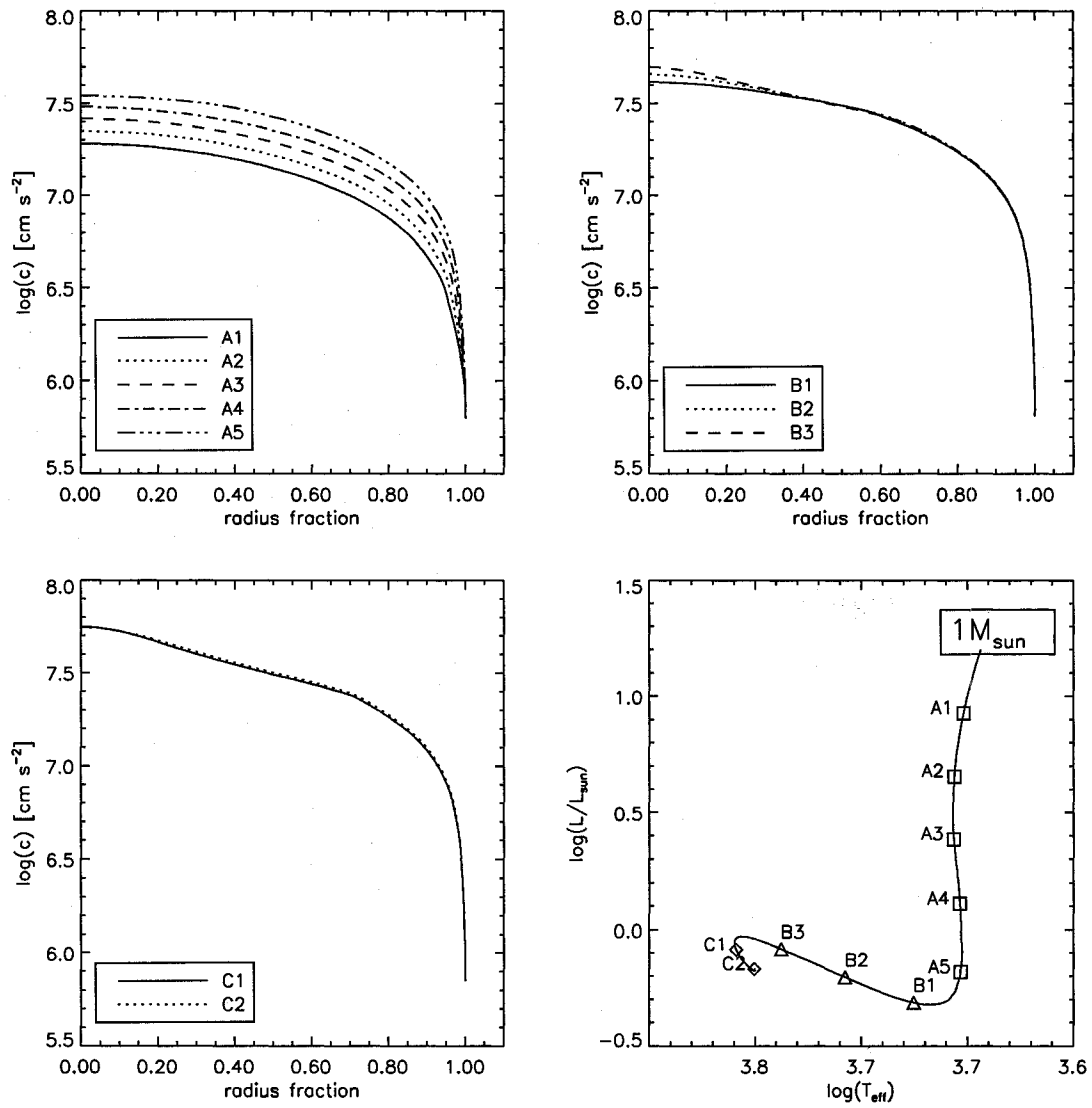
Figure 2.17 Sound speed as a function of radius for a 1 $M_\odot$ evolutionary track.
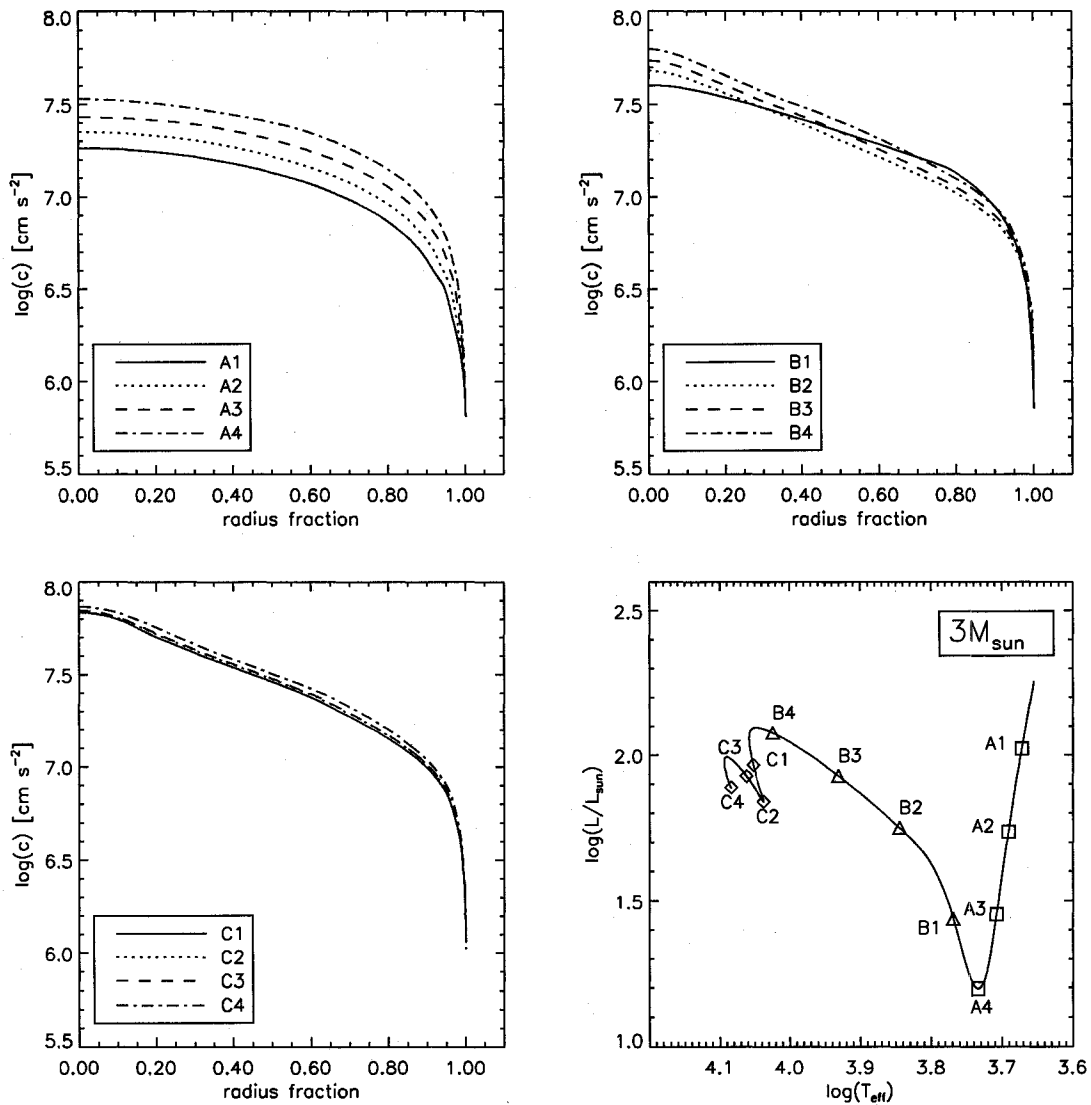
Figure 2.18 Sound speed as a function of radius for a 3 $M_\odot$ evolutionary track.

and

$$L = [l(l+1)]^{1/2}c/r, \tag{2.3}$$

where H is the density scale height, r is the radius, g is the gravitational acceleration, and c is the sound speed.

Figures 2.19 and 2.20 show N and L in real frequency units at selected points in the evolutionary tracks of 1 and 3 $M_\odot$ models. Imaginary components of the frequencies are not shown but do exist through the intervals where the N appears to be zero. As the stars evolve along the Hayashi track and the convective envelope shrinks, the positive region of N grows rapidly with time but drops abruptly to zero (becomes imaginary) at the boundary of the convective envelope. During this phase of evolution, g-modes cannot propagate through much of the star until the convective envelope shrinks. Indeed, the Lamb and Brunt-Väisälä frequencies permit g-modes to propagate in inner regions at frequencies that overlap with the frequencies of p-modes propagating in outer regions. This overlap of frequency range exists in both PMS and post-main sequence stars, and in such instances the g-modes perturb the p-mode frequencies (mode bumping). In the PMS phase, we find that the regions permitting mode bumping are smaller than in stars of similar mass and radius in the post-main sequence phase. This is due in part to the build-up of helium in the core of post-main sequence stars as the star evolves from the ZAMS, in turn producing a peak in N which provides an extended inner region where g-modes can propagate at high p-mode frequencies. This peak is visible in the first panel of figure 2.21 at a radius fraction near 0.05. The smaller overlapping frequency range means p-mode bumping from g-modes in PMS stars is less common because p- and g-mode frequencies are kept separate. The

segregation of p- and g-mode frequencies in PMS stars also affects the frequency separations discussed in chapter 3 as well as in the frequency spectra comparisons in chapter 6. In the later stages of evolution, N becomes imaginary in the convective core. Layers nearest the surface always harbour N that are real because the surface of stars are radiative.

In PMS evolution, there is an outward progression of the inner edge of the Brunt-Väisälä frequency, marked with 'e' in figures 2.19 and 2.20. We see the opposite for the model evolving from the ZAMS, where the inner edge of the Brunt-Väisälä frequency moves further inward in conjunction with the receding edge of the convective core.During post-main sequence evolution, hydrogen in the core is depleted as the star evolves, and as a consequence, the fully mixed convective core recedes. In figure 2.21 we compare the evolution of the Brunt-Väisälä frequency for a star during selected phases of its pre- and post- main sequence evolution. For pre- and post-main sequence models nearest the ZAMS the N profiles are nearly identical but the differences are greatest near the maximum value of N. Modes with frequencies in the range near the peak in the Brunt-Väisälä frequency would be most sensitive to the size of the convective core, and therefore evolutionary state.
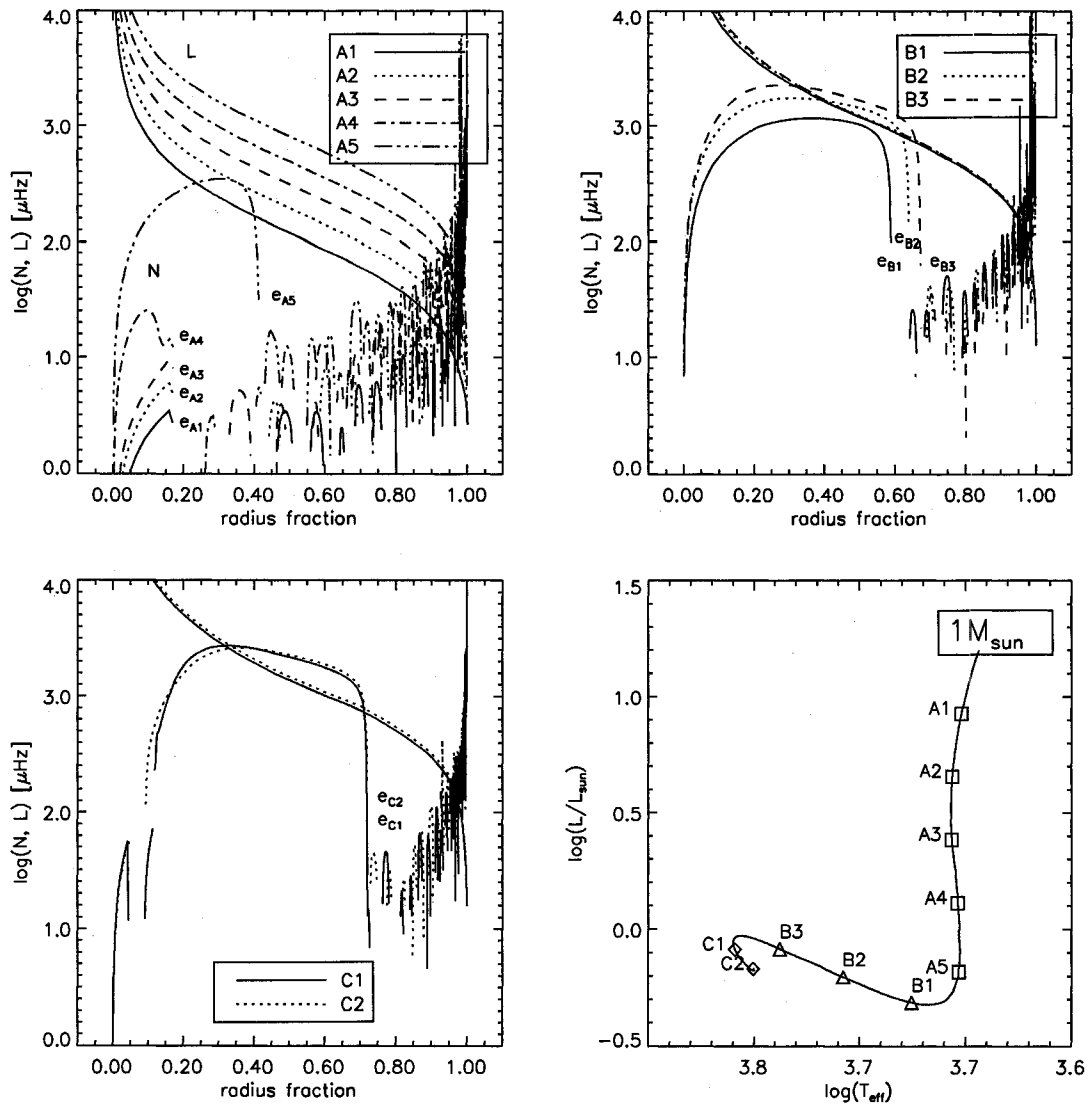
Figure 2.19 Brunt-Väisälä (N) and Lamb (L) frequencies at selected points on a 1 M$_\odot$ evolutionary track.
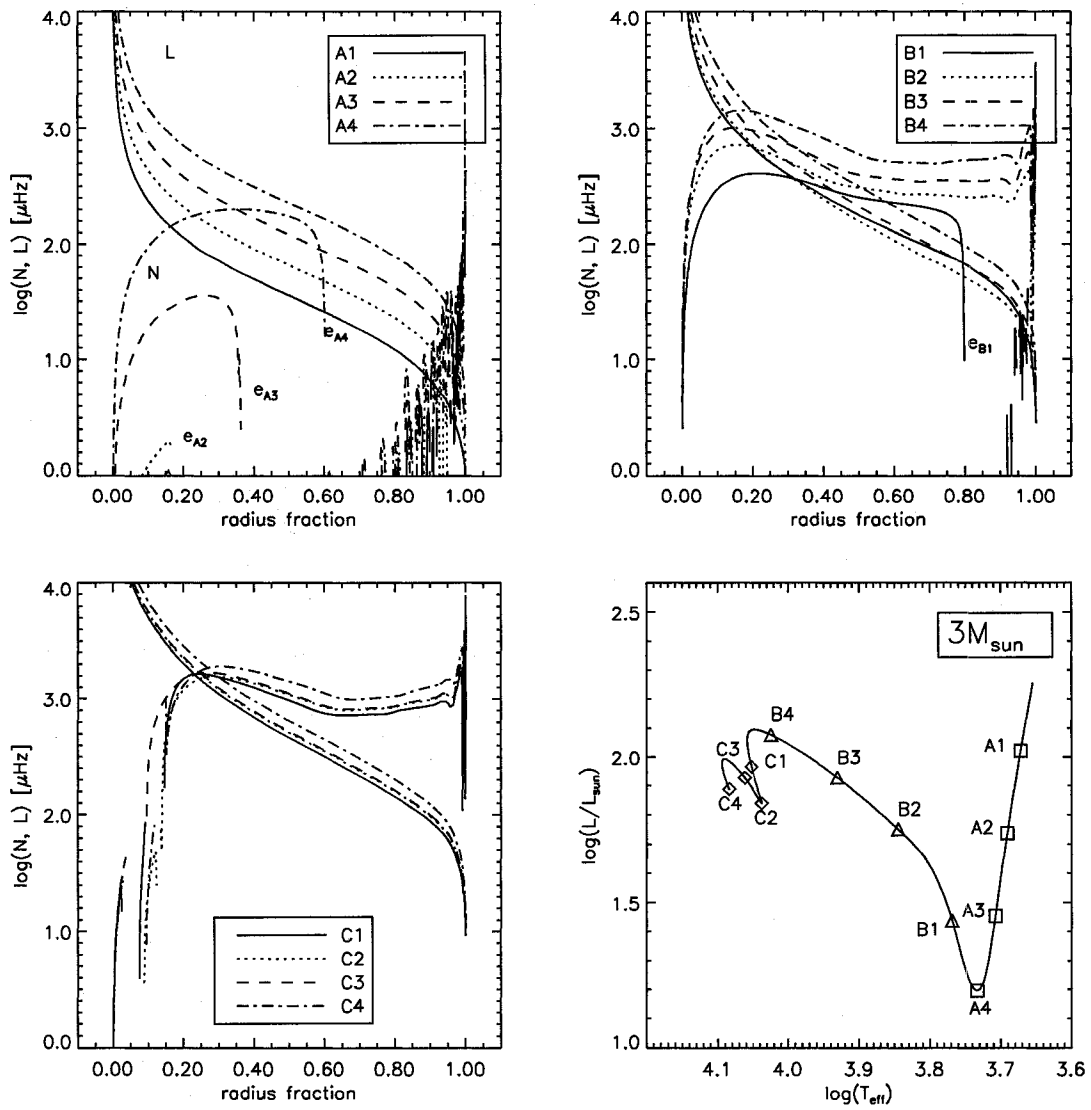
Figure 2.20 Brunt-Väisälä (N) and Lamb (L) frequencies at selected points on a 3 M$_\odot$ evolutionary track.
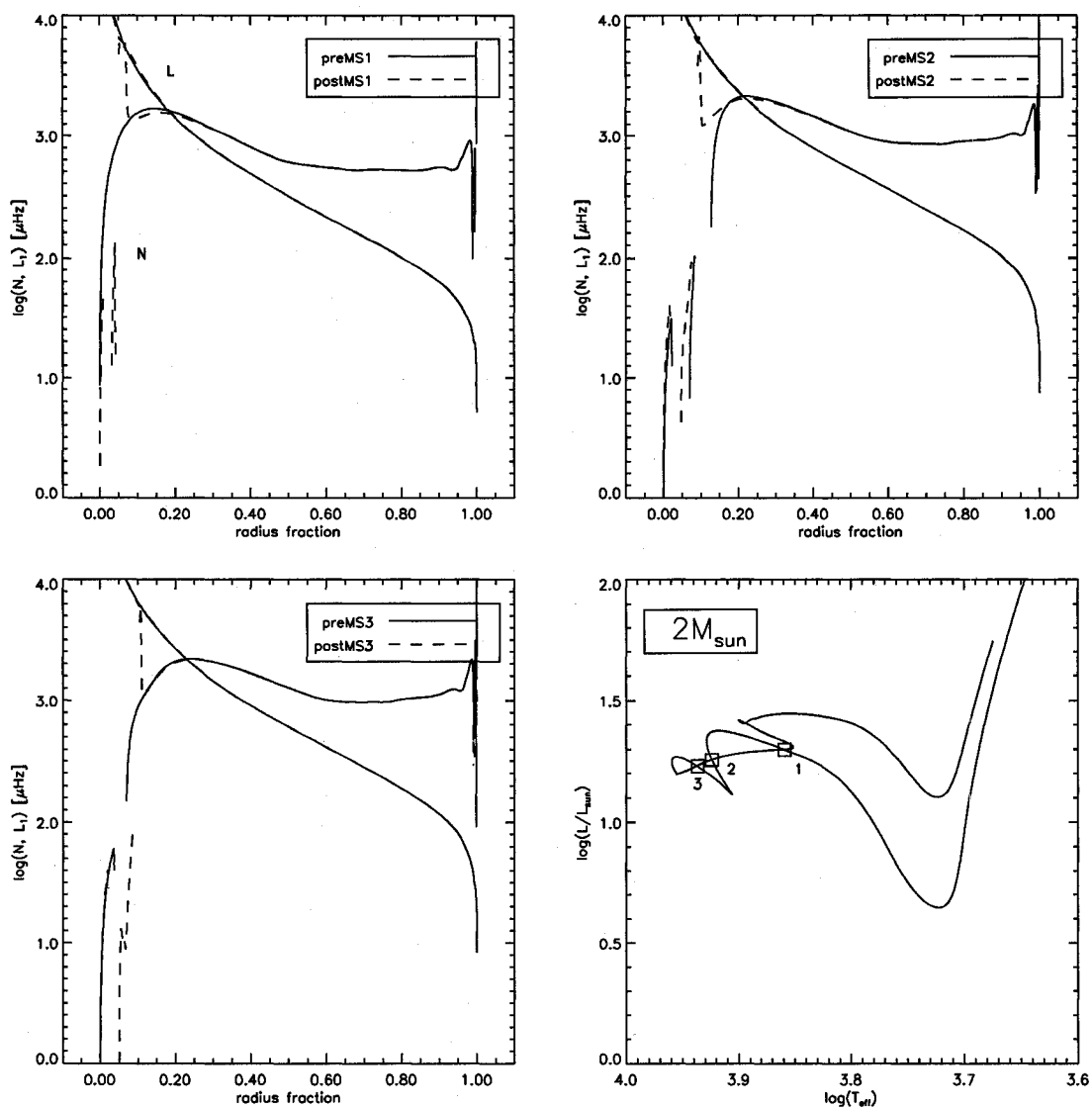
Figure 2.21 The evolution of Brunt-Väisälä (N) and Lamb (L) frequencies at selected points on a 2 M$_\odot$ evolutionary track.

Chapter 3

Large and Small Spacings

Pre-main sequence stars are not expected to exhibit visible p-mode oscillations until they reach the instability strip, and stars in evolutionary stages near or prior to the birthline are undetectable. We examine oscillation spectra of stars in all phases of stellar evolution because other mechanisims may stimulate pulsations, such as stochastic excitation by convection. In the following sections we examine the behaviour of the large and small spacings of pre-main sequence stars across the HR diagram.

3.1   Average Spacings

To examine the behaviour of frequency spacings over the HR diagram we compute an average value for each l. To avoid contamination from the low frequency modes where mode bumping occurs and $n \gg l$, we average the spacings at higher frequency modes where the spacings deviate very little from the mean. Specifically, the spacings are averaged over modes of order $n = 10 - 30$. Figure 3.1 illustrates how the large spacing is primarily an indicator of radius, with large separations for masses ranging from 1 to 5 $M_{\odot}$ compared for pre- and post-main sequence models. For post main sequence stars, with the exception

of a small dependence on mass, the large spacing remains almost entirely a function of radius, enabling it to be used as a tool in the determination of stellar radius from observed frequencies (Guenther, 2002). The PMS models show more dependence on mass, somewhat hindering the usefulness of the large spacing to be used solely as a radius indicator. Nonetheless, the mass dependence is small, and even in the absence of mass information a radius estimate can be determined from an observed large spacing, though with a greater uncertainty than in the post-MS scenario. Examining large spacings of models with varied metal and hydrogen abundance confirms a similar radius-dependant behavior, and that the large spacing is not significantly altered by changes in composition. We can conclude then, that the large spacing is an excellent measure of radius, regardless of the mass or composition of the host star.

We present the average large spacings for all solar composition models between 1 and 5 $M_\odot$ in figure 3.2. The plot shows contours ranging from 5 to 180 μHz for modes of degree $l = 0$. The average large spacing varies little about the mean for high order ($n = 10 - 30$) modes of degree $l = 0$ to 3, so the large spacing for higher degrees are not included. Similarly, figure 3.3 shows contours of large spacing for post-main sequence evolution. Although the behavior is similar for young stars near the ZAMS, the large spacing for $l > 0$ modes becomes difficult to calculate due to frequent mode bumping for models that have evolved through core hydrogen burning.

Similarly, we present contours of average small spacing across the same mass range in figures 3.4 and 3.5, corresponding to PMS and post-main sequence models, respectively. The average spacings for modes of $l > 0$ are not shown. The contours derived from the
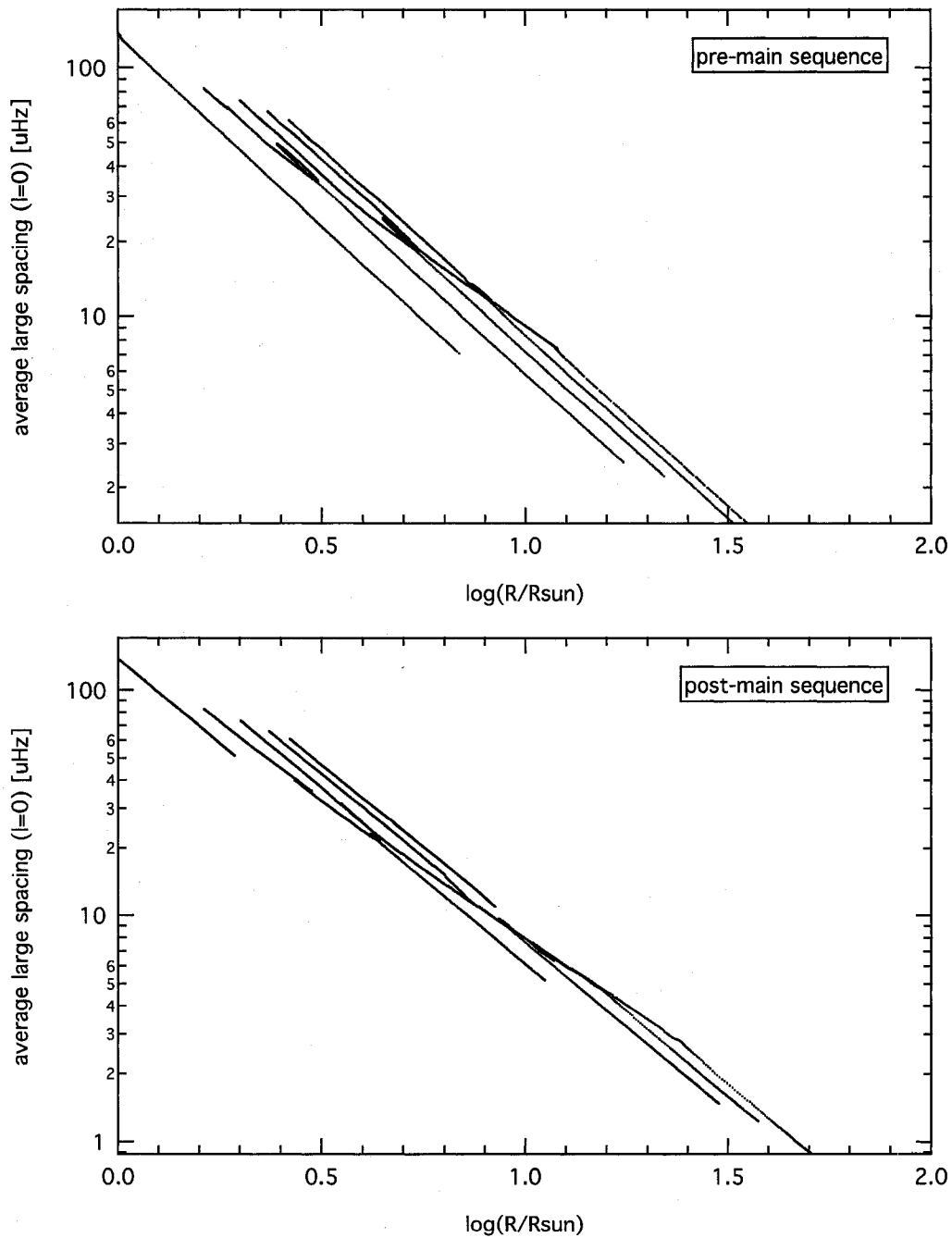
Figure 3.1 Average large spacings for pre-main sequence (top) and post-main sequence (bottom) as a function of model radius. Generally, mass increases from left to right.

post-main sequence models break down shortly after core hydrogen burning as a result of mode bumping. This effect is not present in the pre-main sequence contours, allowing average small spacings to be calculated for very young models that are much farther from the ZAMS.

We present the small spacing averaged over $n = 10$ to 30 as a function of age in figure 3.6. The top two panels display spacings for pre- and post-main sequence models ranging from 1 to 5 $M_\odot$, respectively. In evolved post-main sequence stars, mode bumping interferes with the uniformity of the small spacing so the average spacings are less well defined at these ages (Guenther, 2002). We can take advantage of the fact that mode bumping is comparatively non-existent during PMS evolution to discriminate between the two evolutionary states. To facilitate comparison between similar models, the average small spacings are plotted against model radius in the bottom panel of figure 3.6. Near the ZAMS, the average spacings converge, but diverge at larger radii illustrating the breakdown of the small spacing in evolved post-MS stars from mode bumping. At lower masses the small spacings show greater discrepancy and diverge quickly in models farther from the ZAMS.

3.2 Asteroseismic HR-Diagram

As predicted by asymptotic theory (section 1.3), regularly spaced low-l high-n p-modes produce nearly uniform frequency separations. Originally proposed by Christensen-Dalsgaard (1988), by plotting the large spacing on the abscissa and the small spacing on the ordinate, these separations can be arranged in a manner analogous to the temperature and lumi-
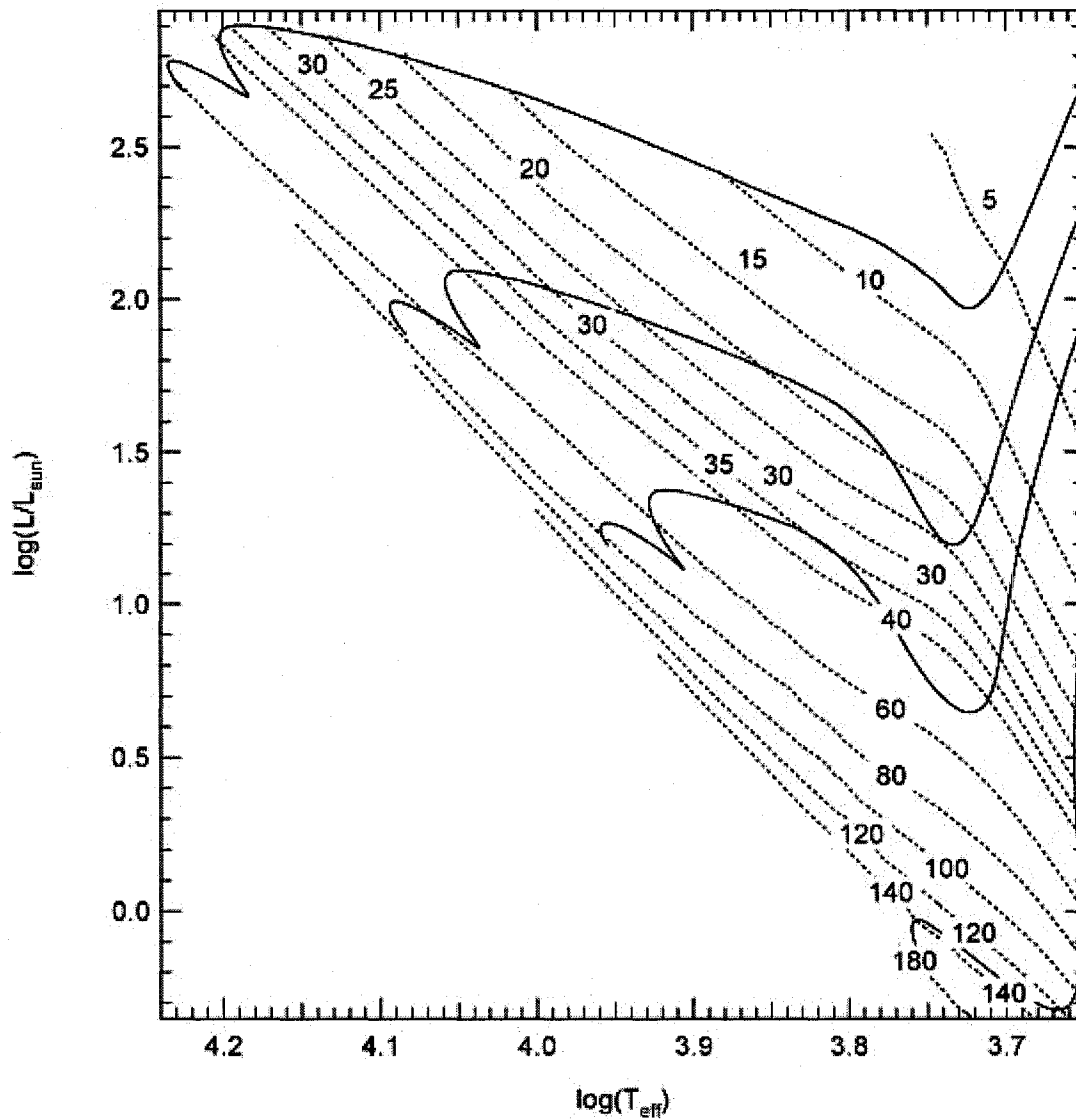
Figure 3.2 Contours of averaged large spacing for $l = 0$ modes of PMS models. Frequencies are displayed in μHz. Averaged large spacings for modes of degree $l > 0$ are similar and are not shown. PMS stellar evolution tracks at 1, 2, 3 and 5 $M_\odot$ are presented for reference.
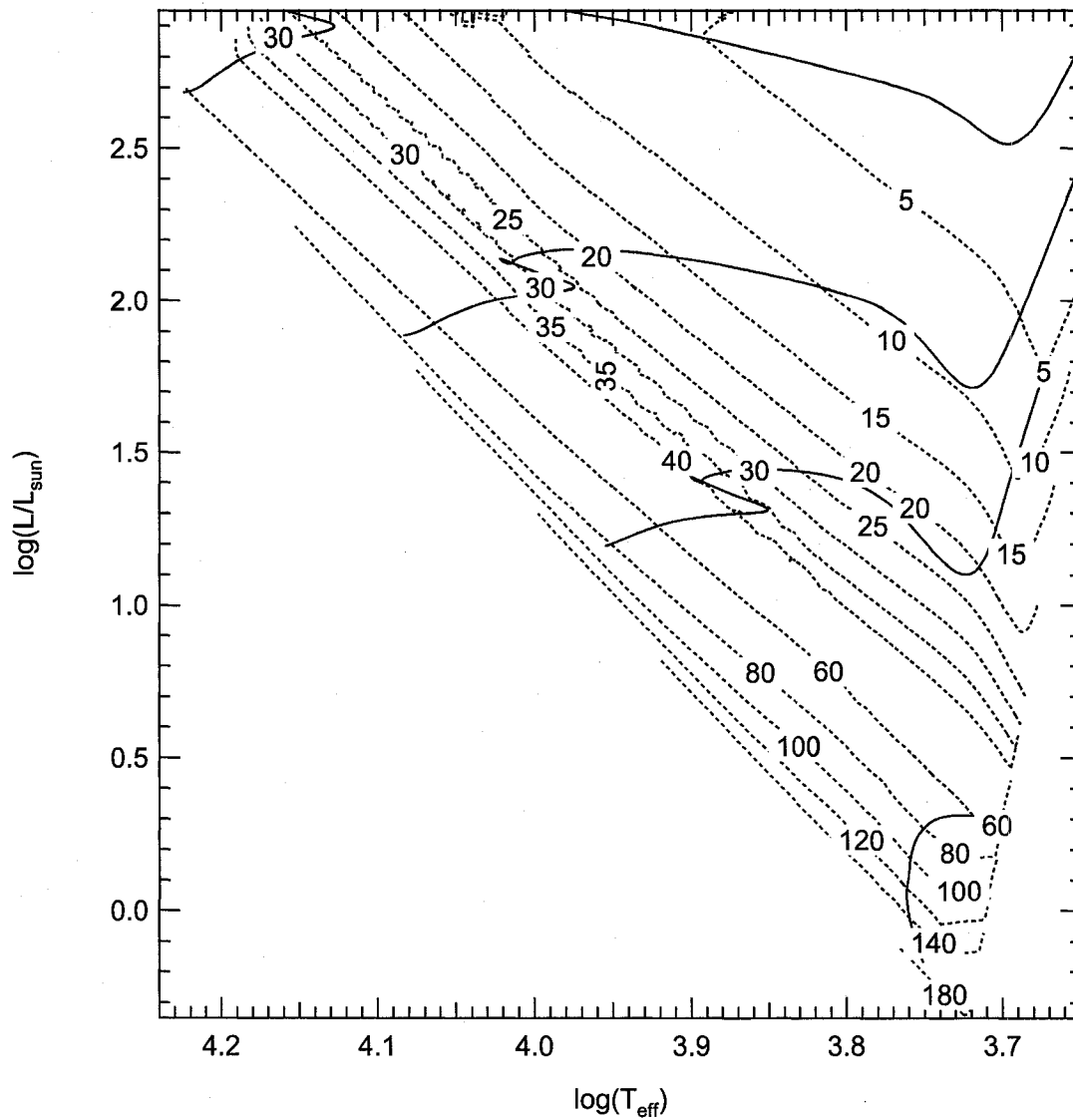
Figure 3.3 Contours of averaged large spacing for $l = 0$ modes of post-main sequence models. Frequencies are displayed in μHz. Averaged large spacings for modes of degree $l > 0$ are similar and are not shown. Post-main sequence evolution tracks at 1, 2, 3 and 5 $M_\odot$ are included for reference.
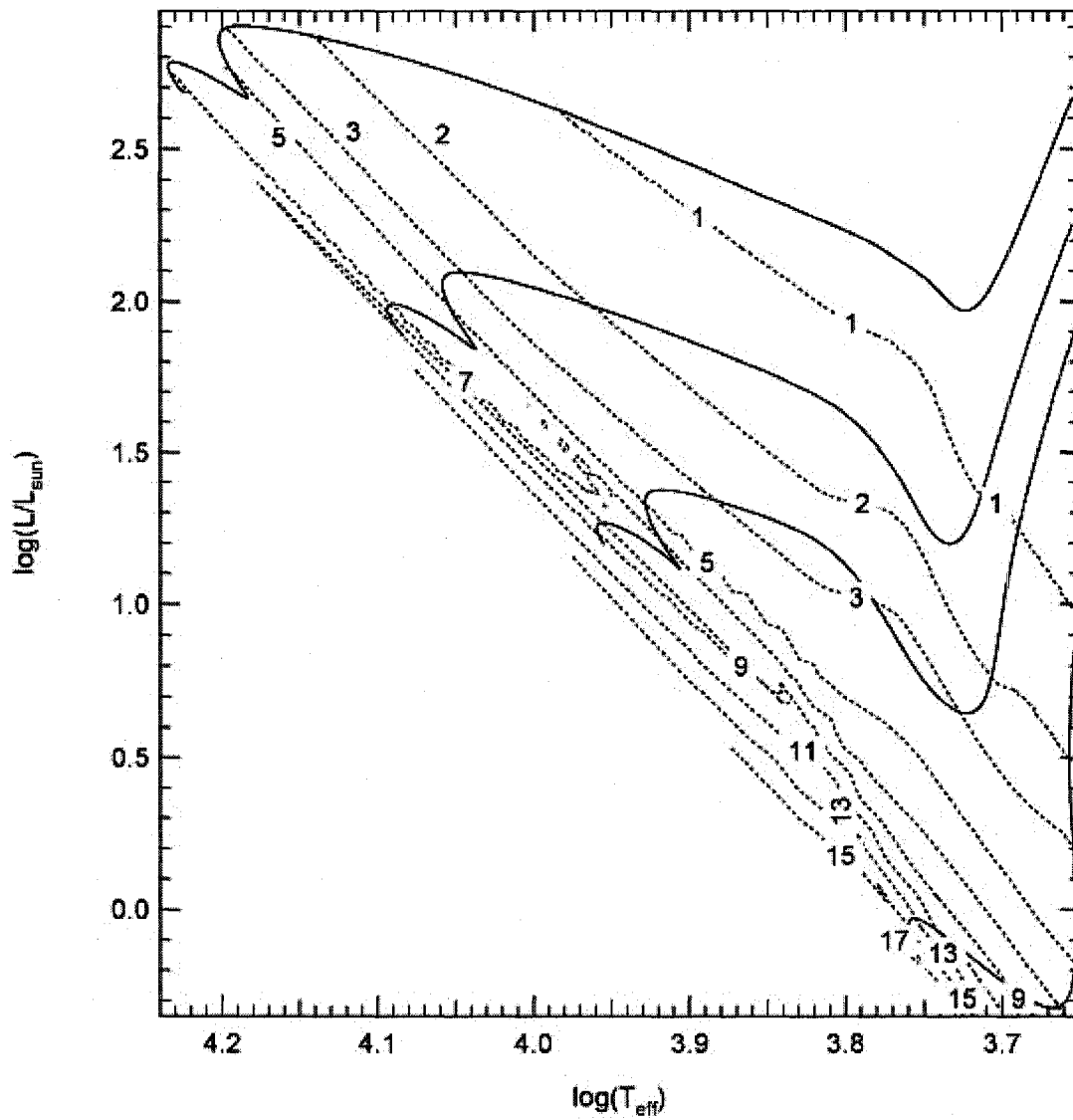
Figure 3.4 Contours of small spacing for $l = 0$ modes of PMS models. Frequencies are displayed in μHz. PMS evolution tracks at 1, 2, 3 and 5 $M_\odot$ are included for reference.
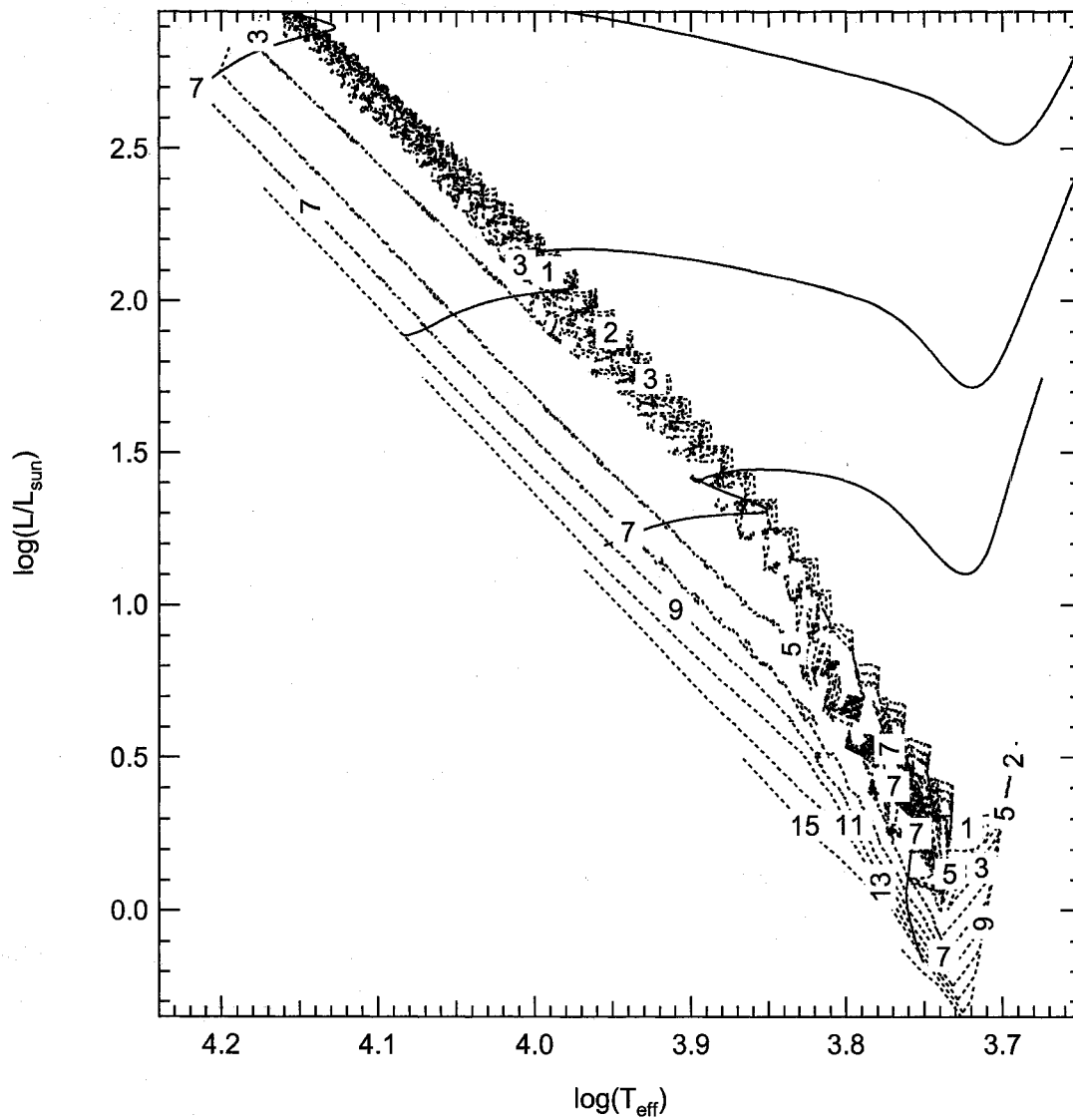
Figure 3.5 Contours of small spacing for $l = 0$ modes of post-main sequence models. Frequencies are displayed in μHz. Post-main sequence evolution tracks at 1, 2, 3 and 5 $M_\odot$ are included for reference.
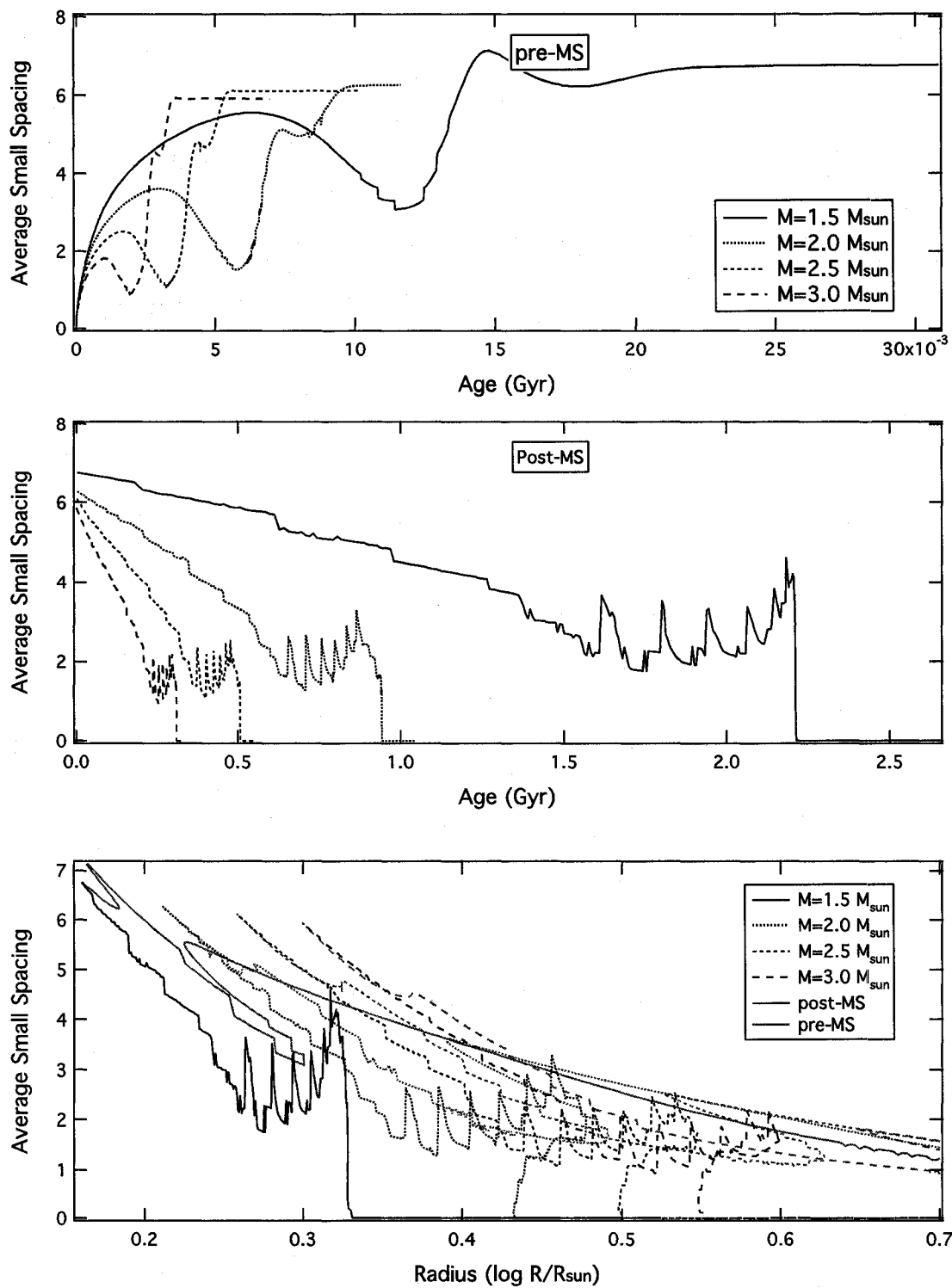
Figure 3.6 Average small spacings for 1.5, 2.0, 2.5 and 3,0 M$_\odot$ models. The top and middle panels show spacings for pre- and post-main sequence models, respectively. Spacings as a function of radius for both phases of evolution are compared in the bottom panel.

nosity evolutionary tracks of the HR-diagram. In principle, the observed large and small separations of a star can be translated into stellar mass and age via this "asteroseismic HR diagram". Like the traditional HR-diagram, the large and small frequency separations are sensitive to parameters that affect stellar structure, including chemical composition (Christensen-Dalsgaard, 1993), which in turn hinders the ability to determine stellar properties from frequencies alone and illustrates the importance of combining asteroseismic data with other information (Gough, 1987). In spite of these uncertainties, the asteroseismic HR diagram illustrates the dependence of frequency separations on stellar model parameters and demonstrates that the separations are dependent on different aspects of stellar structure.

Our asteroseismic HR diagram for post-main sequence models (Figure 3.7) is consistent with the results of Christensen-Dalsgaard (1988). In figures 3.8 and 3.9 we present our PMS large and small spacings superimposed on the post-main sequence asteroseismic HR diagram. We compute spacings for several evolutionary tracks from 1.0 to 5.0 $M_\odot$, and for spacings computed from $l = 0$ and $l = 1$ modes. These asteroseismic HR diagrams are similar to those in Christensen-Dalsgaard (1993), showing contours of mass and core hydrogen abundance (isopleths), except during PMS evolution. We compute spacings by averaging high order modes ($n = 20 - 30$) because the frequency spacings are nearly uniform in this range. The evolution of pre-main sequence stars begins with low averaged large and small seperations that increase with stellar age (decreasing radius) until the model contracts to the ZAMS. Post-main sequence evolution follows the opposite general trend as the stellar radius increases with age. Mass contours are identified as pre- and post-main

sequence by dotted and solid lines, respectively. Isopleths are used as an indicator of the stage of post-main sequence evolution and are related to the age of the models; contours are shown for central abundances ranging from $X_c = 0.20$ to $X_c = 0.70$. Isopleths for PMS stars are not shown because PMS stars do not experience core hydrogen burning during their evolution, so isopleths are not an indicator of age.

The evolutionary state of models with stellar masses below 1.5 $M_\odot$ is clearly distinguished with mass contours and isopleths. The large spacing is largely a function of the mean density and scales approximately as $\rho^{-1/2}$. For models more massive than 1.5 $M_\odot$, the large separation becomes less dependant on the mass, adding to the difficulty in distinguishing the evolutionary state in this manner, while the small separation remains largely independent of mass through the entire mass range.

Nuclear burning causes the post-main sequence mass contours to experience frequent departures from the otherwise smooth profile, especially during the latter stages of evolution where mode bumping is common. Contrasting this, the lack of core nuclear burning in their pre-main sequence counterparts preserves the smooth profile throughout the entire PMS evolution for all modes.
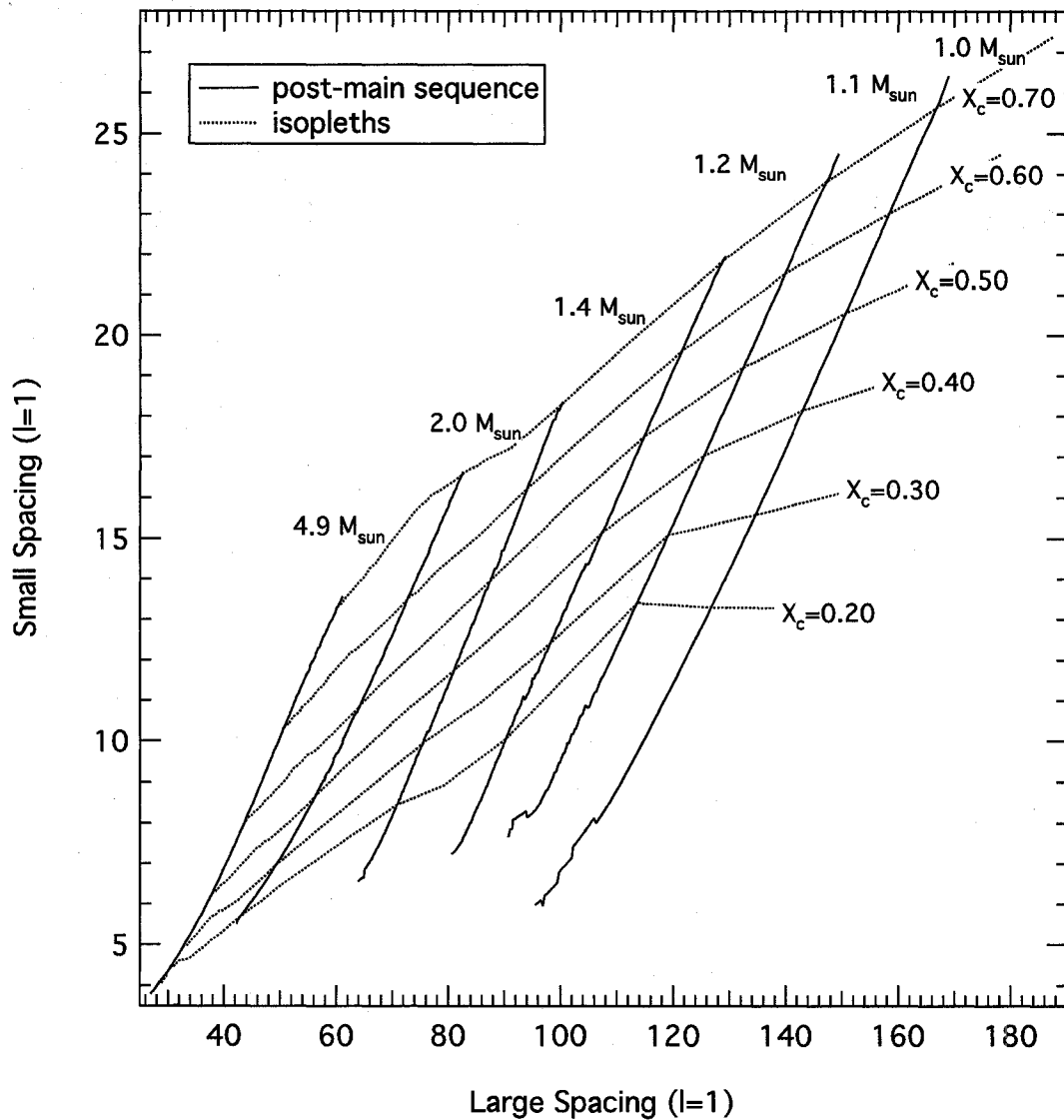
Figure 3.7 Asteroseismic HR-diagram showing small ($\delta\nu$) versus large ($\Delta\nu$) frequency spacing for $l = 1$ modes of post-main sequence evolutionary tracks. Contours of constant mass are presented at $M_\odot = 1.0$, 1.1, 1.2, 1.4, 2.0 and 5.0. Isopleths of $X_c = 0.7$, 0.6, 0.5, 0.4, 0.3 and 0.2 are represented with dotted lines.
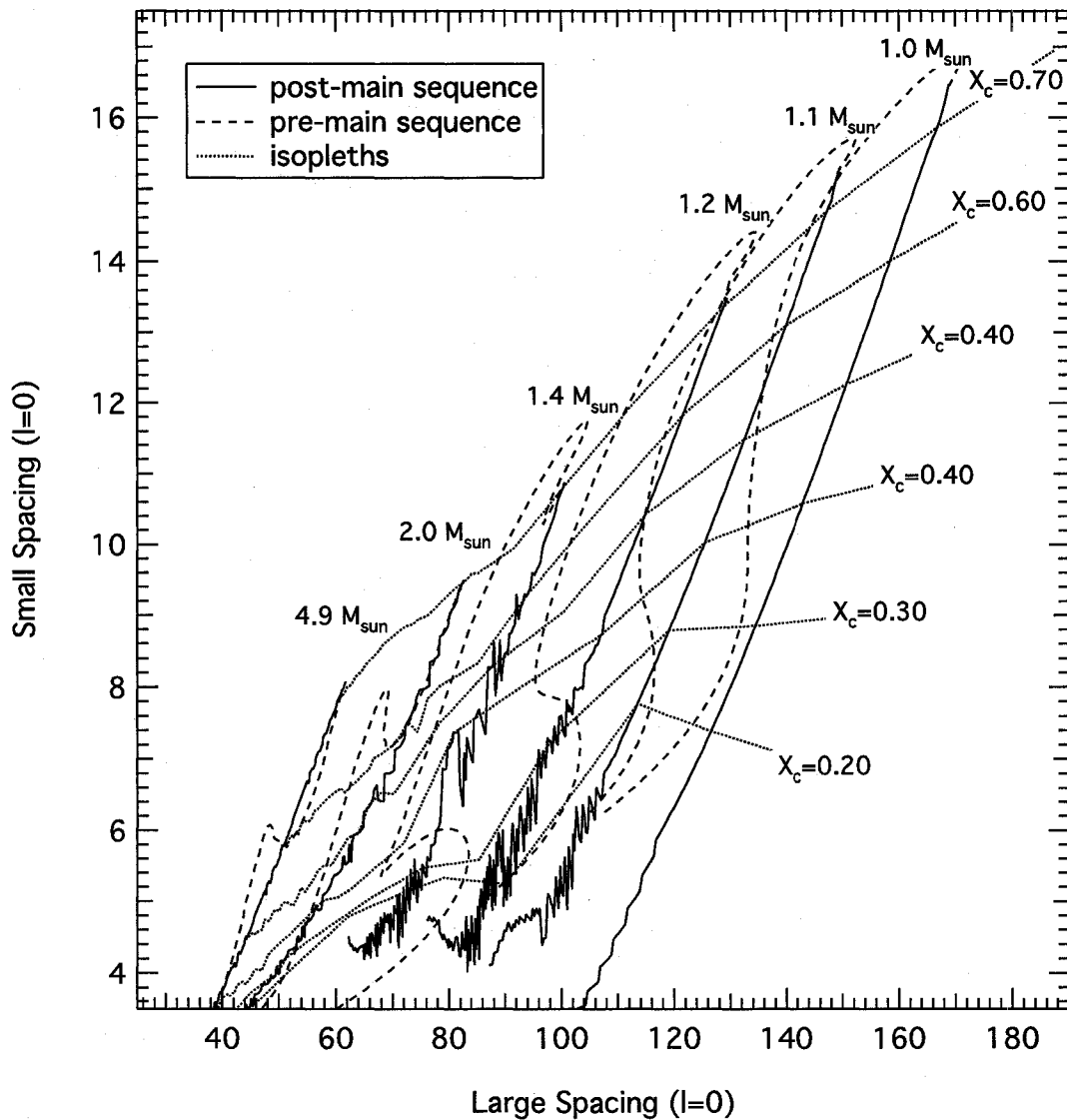
Figure 3.8 Asteroseismic HR-diagram showing small ($\delta\nu$) versus large ($\Delta\nu$) frequency spacing for $l = 0$ modes. Contours of constant mass are indicated with solid (post-main sequence) and dashed (pre-main sequence) lines at $M_\odot = 1.0$, 1.1, 1.2, 1.4, 2.0 and 5.0. Isopleths of $X_c = 0.7$, 0.6, 0.5, 0.4, 0.3 and 0.2 are represented with dotted lines.
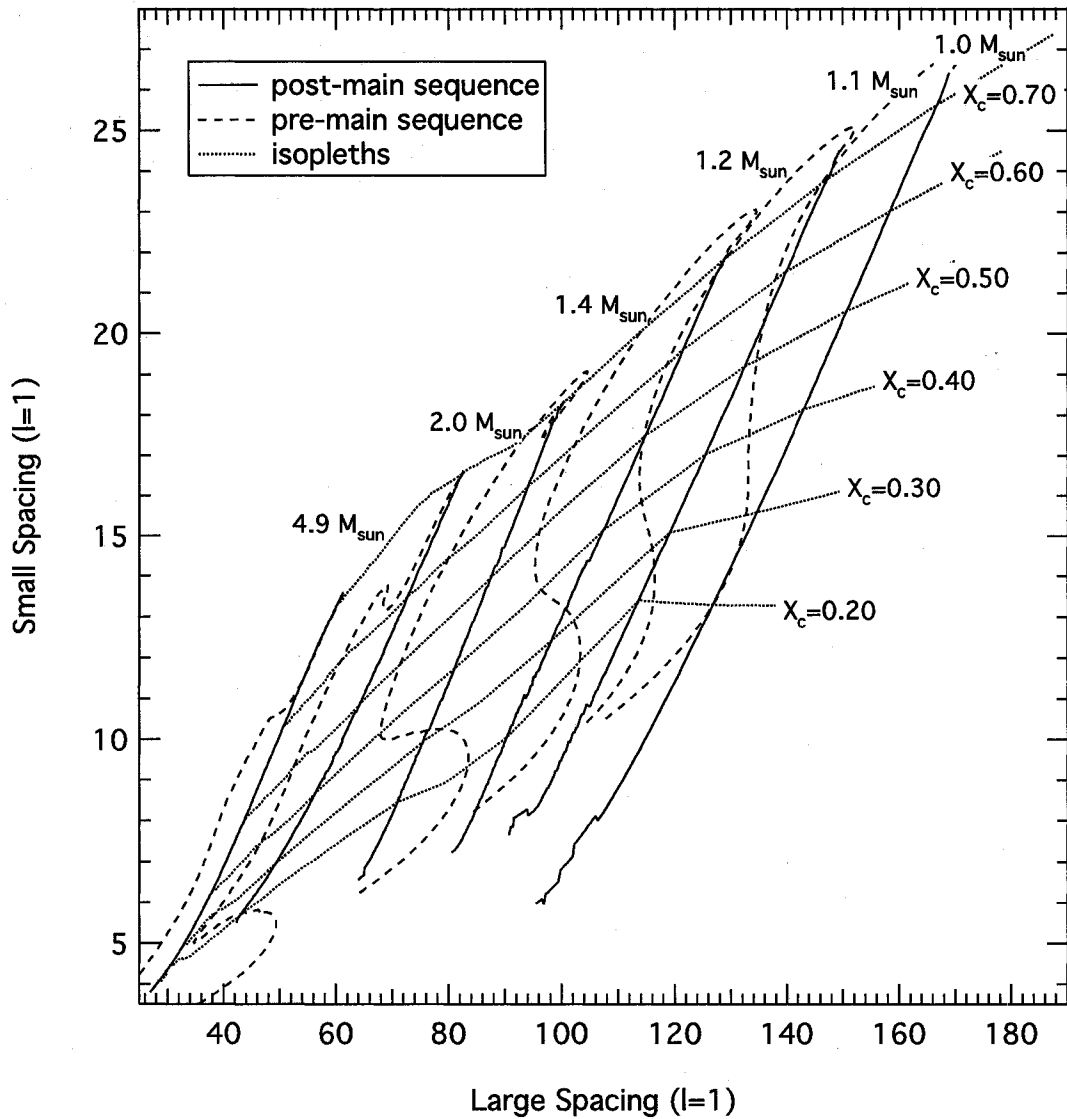
Figure 3.9 Asteroseismic HR-diagram showing small ($\delta\nu$) versus large ($\Delta\nu$) frequency spacing for $l = 1$ modes. Contours of constant mass are indicated with solid (post-main sequence) and dashed (pre-main sequence) lines at $M_\odot = 1.0$, 1.1, 1.2, 1.4, 2.0 and 5.0. Isopleths of $X_c = 0.7$, 0.6, 0.5, 0.4, 0.3 and 0.2 are represented with dotted lines.

3.3 PMS and Post-MS Frequency Spectra

In regions of the HR diagram near the ZAMS, stars that have similar surface properties share the same HR diagram location despite differences in internal structure. We examine model pairs of the same mass and radius in the pre- and post-main sequence phase so that we can consider changes in oscillation spectra from internal structure alone. Figure 3.10 illustrates examples of these model pairs, showing that there can be up to three locations where pre- and post-main sequence evolutionary tracks cross.

From examining the Brunt-Väisälä frequency at various stages of pre- and post-main sequence evolution (refer to section 2.5), we expect low frequency modes to be most sensitive to changes in the convective core and evolutionary state of the model. Figure 3.11 compares mode frequencies of degree $l = 0, 1, 2$, and 3 for a pre- (diamonds) and post- (squares) main sequence model. The oscillation spectra are from the 2 $M_\odot$ model pair comprising a young PMS star and a post-main sequence star nearing core hydrogen burning turnoff. Nuclear burning in the post-main sequence model causes a μ-gradient to develop near the edge of the convective core, which causes some frequencies to be bumped. Because the μ-gradient is less significant in younger post-main sequence stars, frequency spectra of model pairs closer to the ZAMS will be similar. Of course, at the ZAMS the two frequency spectra are identical.

Because both models in figure 3.11 have the same mean density and are similar on the surface layers, both sets of $l = 0$ frequencies are the same over this range. The greatest differences appear at low frequencies, in the $l = 1, 2$ and 3 modes, and although it is
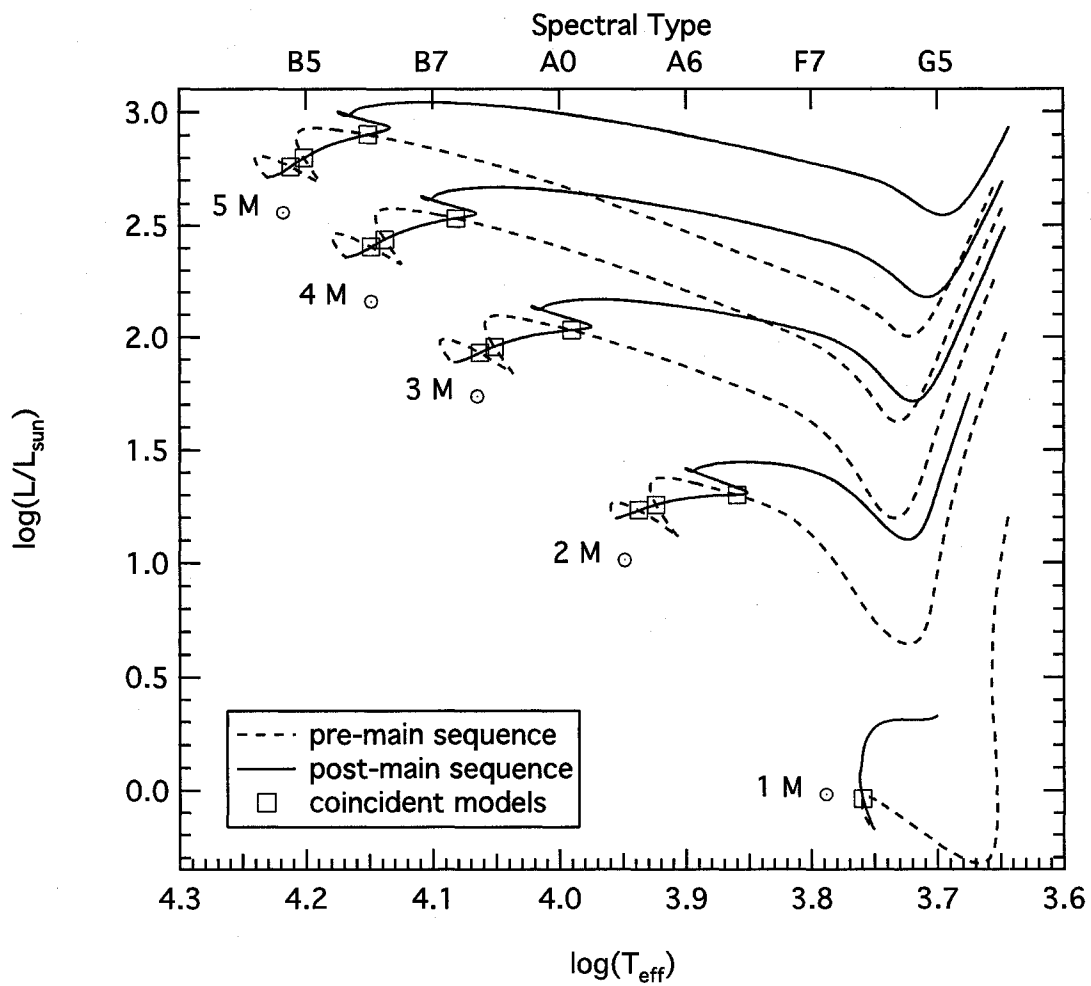
Figure 3.10 Pre- and post-main sequence evolutionary tracks at 1, 2, 3, 4 and 5 $M_\odot$. Coincident models that have the same mass and radius are indicated with squares.
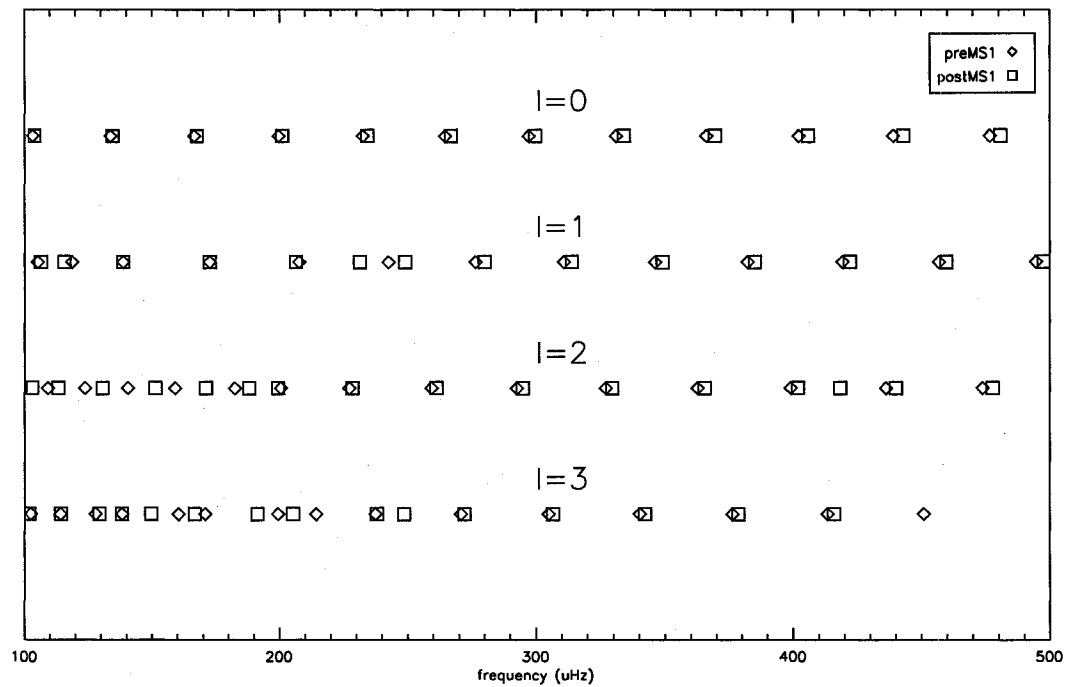
Figure 3.11 Frequency distribution for the $l = 0$, 1, 2 and 3 modes from 2 M$_\odot$ models that occupy the same position in the HR diagram. Pre- and post-main sequence frequencies are identified with diamonds and squares, respectively.

clear that the two spectral patterns vary significantly enough to discriminate the pre-main sequence stage from the post-main sequence stage when the complete spectrum is available, successful use of observed frequencies for this purpose will depend on which frequencies are observed. It is not difficult to select a subset of frequencies from figure 3.11 that match well both pre- and post-main sequence spectra. We compare in greater detail the oscillation spectra of pre- and post-main sequence models across the HR-diagram in chapter 6.

Defined in section 1.3 (equation 1.7), the large frequency spacing is the difference in the frequencies of two modes that are adjacent in order. When comparing pre- and post-main sequence model pairs that share a common HR diagram location, we expect the large separations to be similar because the stars have the same mean density and similar surface layers. Because the large separation scales as $(GM/R^3)^{1/2}$, it decreases with age (radius) for post-main sequence evolution and increases with age (radius) during pre-main sequence evolution. For a given mass, the separations are smallest for the models with the largest radii, and largest for the model at the ZAMS, where the radius is the smallest. It is clear then, that the large separations grow throughout pre-main sequence evolution, and shrink again during post-main sequence evolution away from the ZAMS.

First identified by Osaki (1975) and Aizenman *et al.* (1977), variations in the large separation of nonradial modes in post-main sequence stars are attributed to a mode bumping resulting from the development of a gradient in μ at the edge of the convective core. Aside from this, there is no significant difference in the large separations of pre- and post-main sequence model pairs. The frequency at which this bumped mode occurs is correlated with the peak of the Brunt-Väisälä frequency at the edge of the convective core. Higher degree

modes ($l = 2$ and $l = 3$) are more affected by mode bumping.

We show the large separations for $l = 2$ and $l = 3$ modes from a 2 $M_\odot$ model at the ZAMS and three model pairs in figures 3.12 and 3.13. The bumped mode does not exist in the ZAMS model because the μ-gradient does not yet exist. The frequency of the bumped mode is observed at higher frequencies with age, and when a star reaches an evolutionary state near core hydrogen burning turnoff, a second or even third bumped mode can be seen at lower frequencies, also propagating to higher frequencies with age. The age at which the subsequent mode bumpings appear and how numerous they are depends on the mass of the model. We present the frequency of the first and second mode bumpings as a contour plot in figure 3.15, which shows bumped modes from $l = 2$ and $l = 3$ modes. These contour plots correspond to the bumped modes marked MB_1 in figures 3.12 and 3.13. Frequencies are in μHz with a scale factor of GM/R^3. We do not track the mode bumping beyond core hydrogen turnoff because considerable mode bumping produces a chaotic large spacing profile, and instances of mode bumping cannot be isolated and tracked. It is in these later stages of post-main sequence evolution that the pre- and post-main sequence p-mode spectra differ the most. In figure 3.14, we compare the large spacing of a pre- and post- main sequence models pair during the horizontal phases of evolution. Note that these two models have the same radius but not the same mass. The more complex internal structure of the giant star results in numerous bumped modes, but the simple structure of the pre-main sequence star keeps the asmyptotic p-mode spectrum intact and free from mode bumping.

The small spacing is more sensitive to structural changes in the stellar core, and therefore
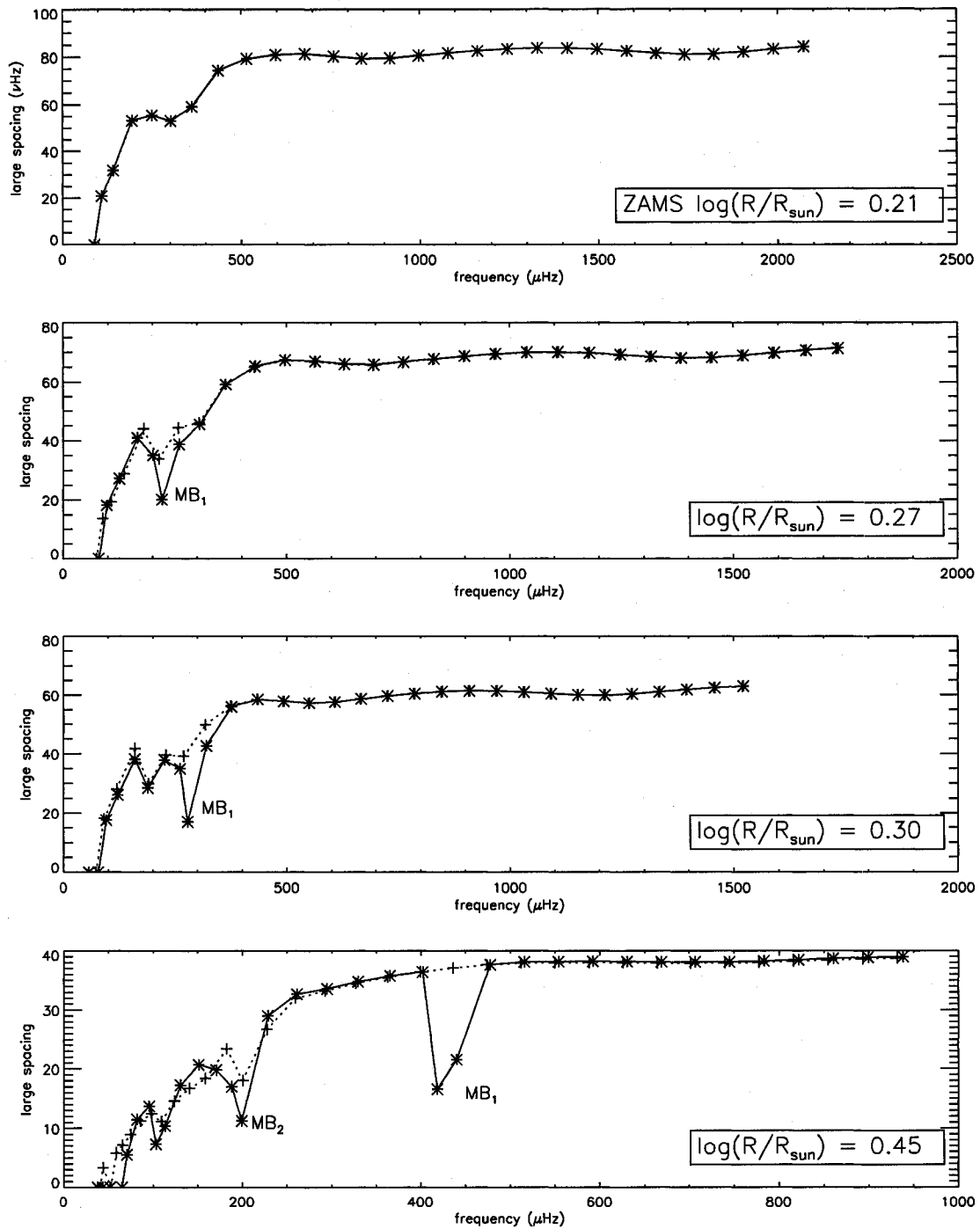
Figure 3.12 Large frequency spacings for $l = 2$ modes of PMS (dotted line) and post-main sequence (solid line) model pairs from the 2 $M_\odot$ evolutionary tracks in figure 3.10. Frequencies of bumped modes (MB$_1$ and MB$_2$) increase with age through post-main sequence evolution.
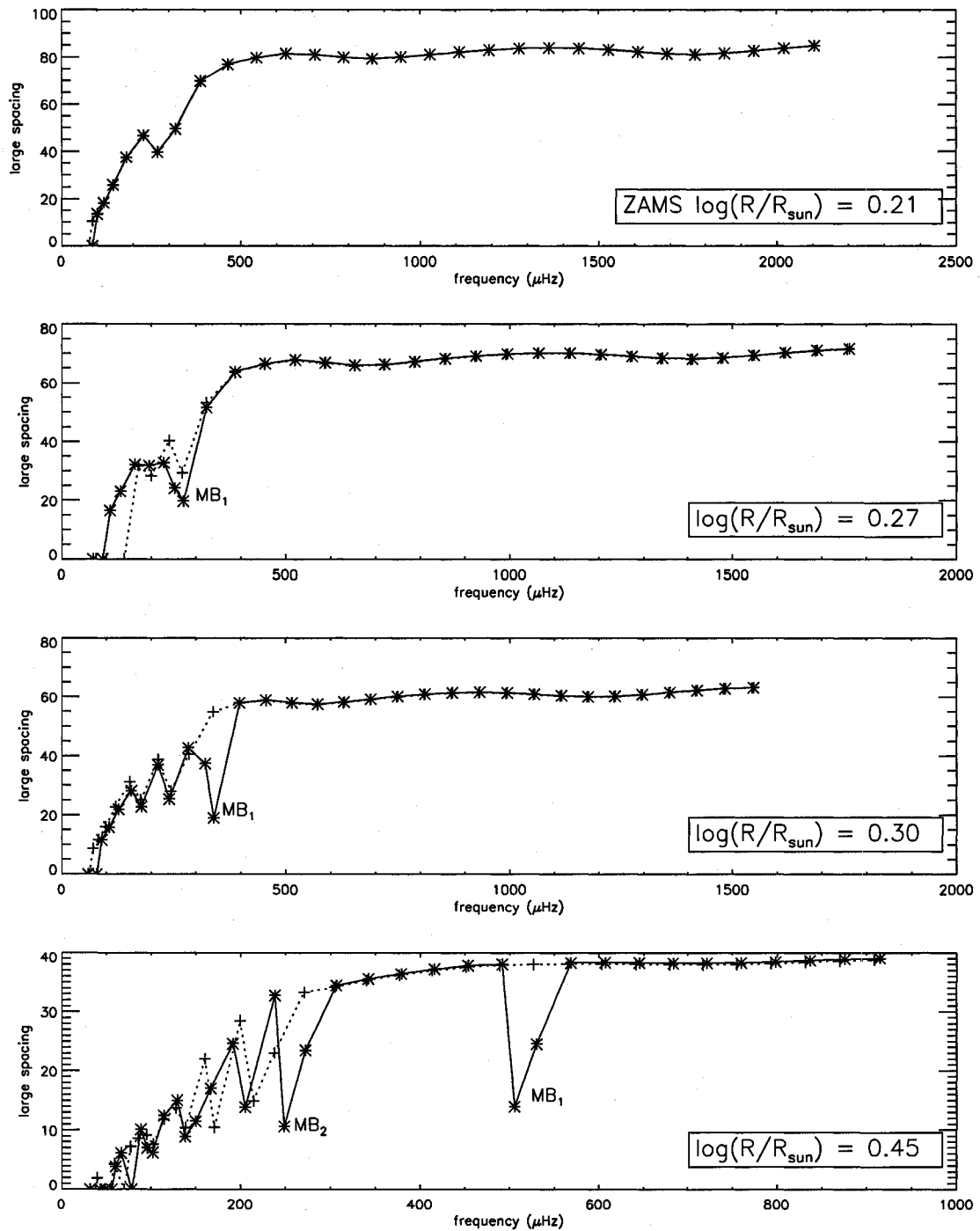
Figure 3.13 Large frequency spacings for $l = 3$ modes of PMS (dotted line) and post-main sequence (solid line) model pairs from the 2 $M_\odot$ evolutionary tracks in figure 3.10. Frequencies of bumped modes (MB$_1$ and MB$_2$) increase with age through post-main sequence evolution.
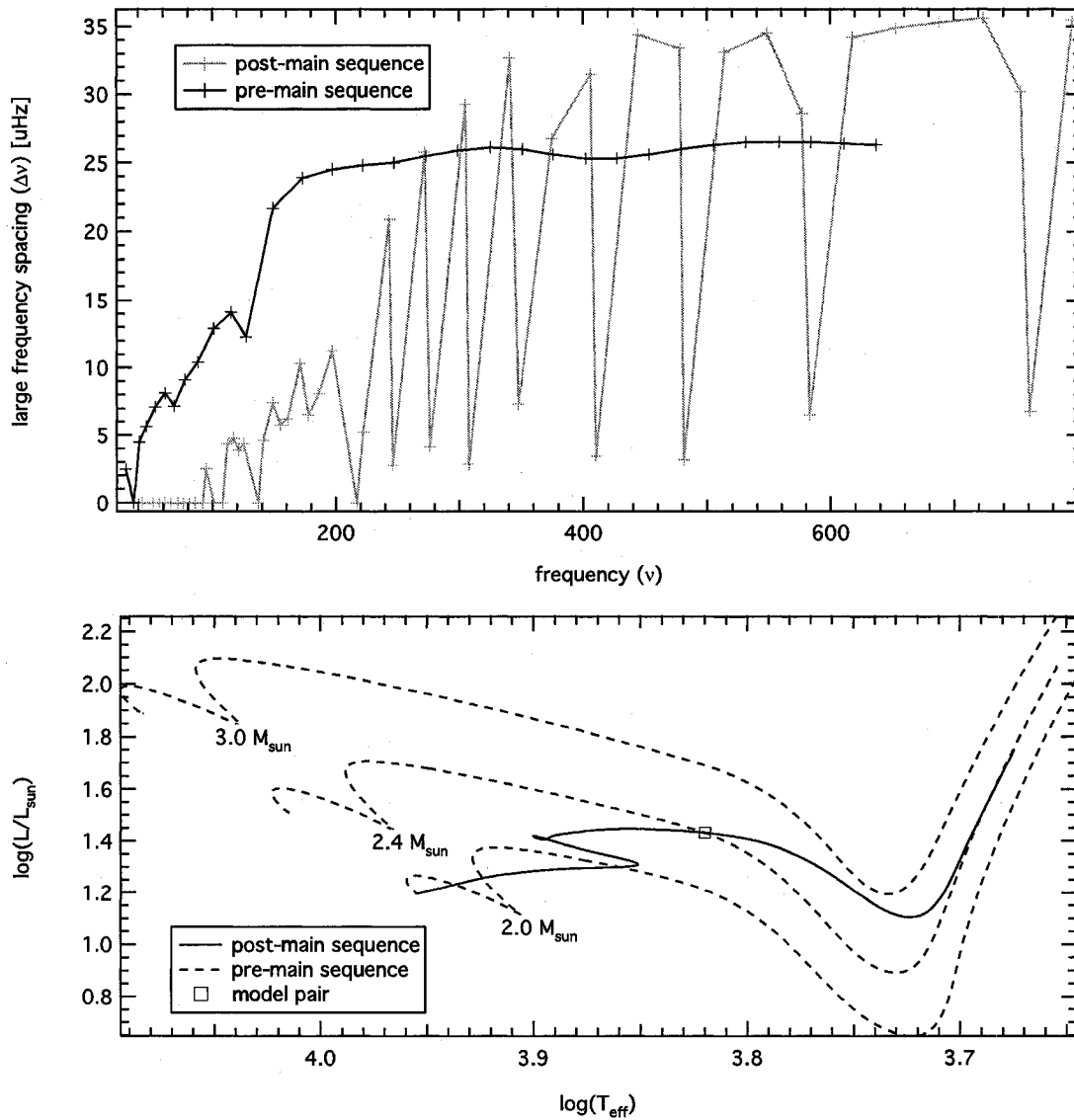
Figure 3.14 Large spacings (upper panel) for $l = 2$ modes of a PMS and post-MS model pair. Both models are coincident in the HR diagram (lower panel) with $Log(T_{eff} = 3.82)$ and $log(L/L_\odot) = 1.43$. Unlike figures 3.12 and 3.13, these models do not have the same mass.
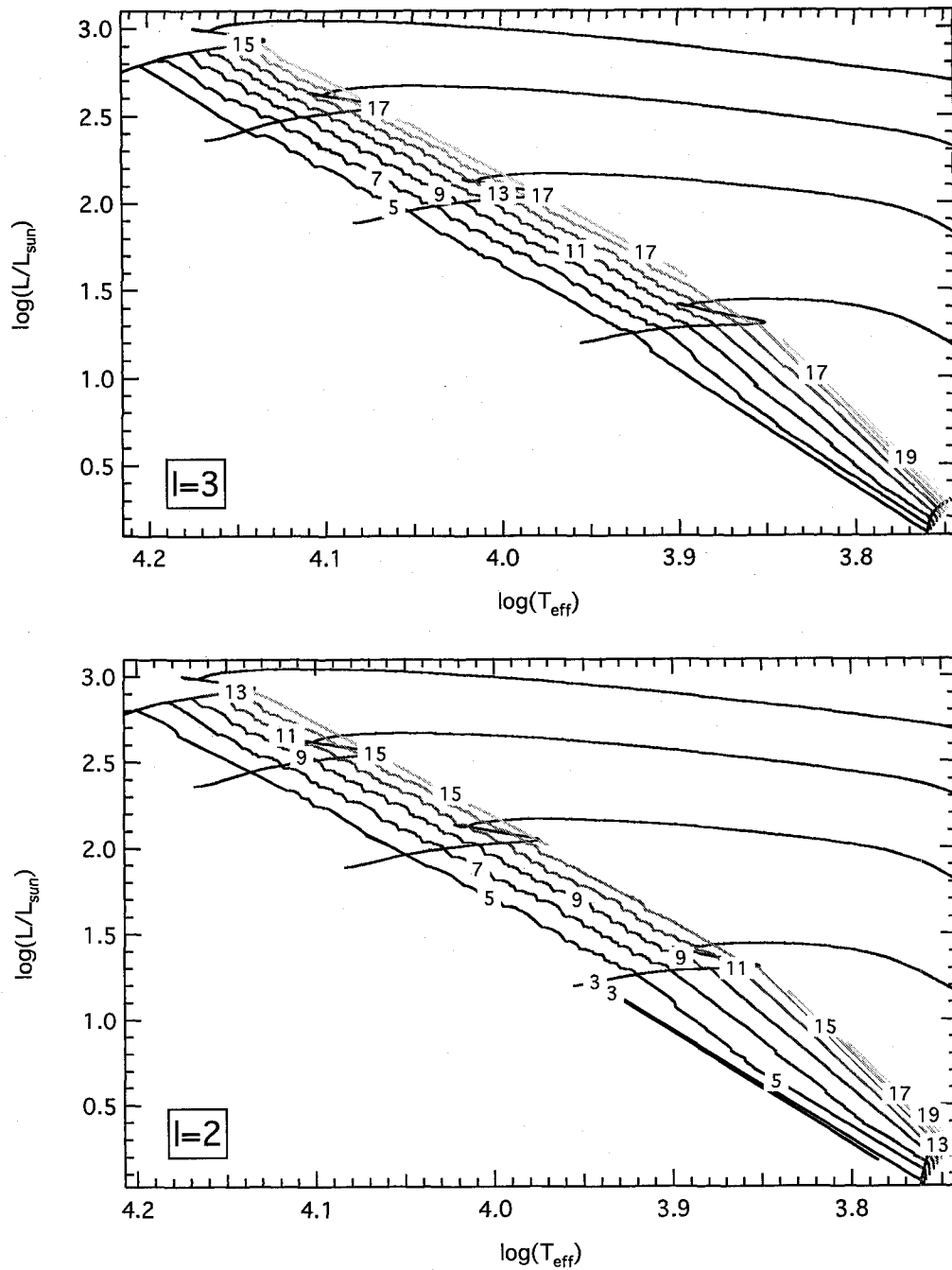
Figure 3.15 Contours showing the frequency of the first mode bumping (MB$_1$ in figures 3.12 and 3.13) for all post-main models between the ZAMS and core hydrogen burning turnoff. Frequencies are in μHz with a scale factor of to GM/R^3.

is a more suitable measure of the evolutionary state of the star than the large spacing. The small spacing follows core density changes with evolution, resulting in a decrease in small spacing during post-ZAMS evolution, and a concomitant increase in small spacing through pre-main sequence evolution. For models pairs near the ZAMS, inner structural differences are not large so the small spacings are comparable, but model pairs farther from the ZAMS have very different internal structure which results in different small spacings.

We show small spacings for model pairs nearest the ZAMS for 1, 2 and 3 $M_\odot$ models in figure 3.16. Unlike the large spacing, the small spacings exhibit discernable differences between pre- and post-main sequence structure models in both $l = 0$ and $l = 1$ degree modes. This difference is largest at lower masses, and exists throughout modes of $n \gg l$, allowing small spacing averages to be effectively used as a tool in the discrimination of pre- and post-main sequence stars.
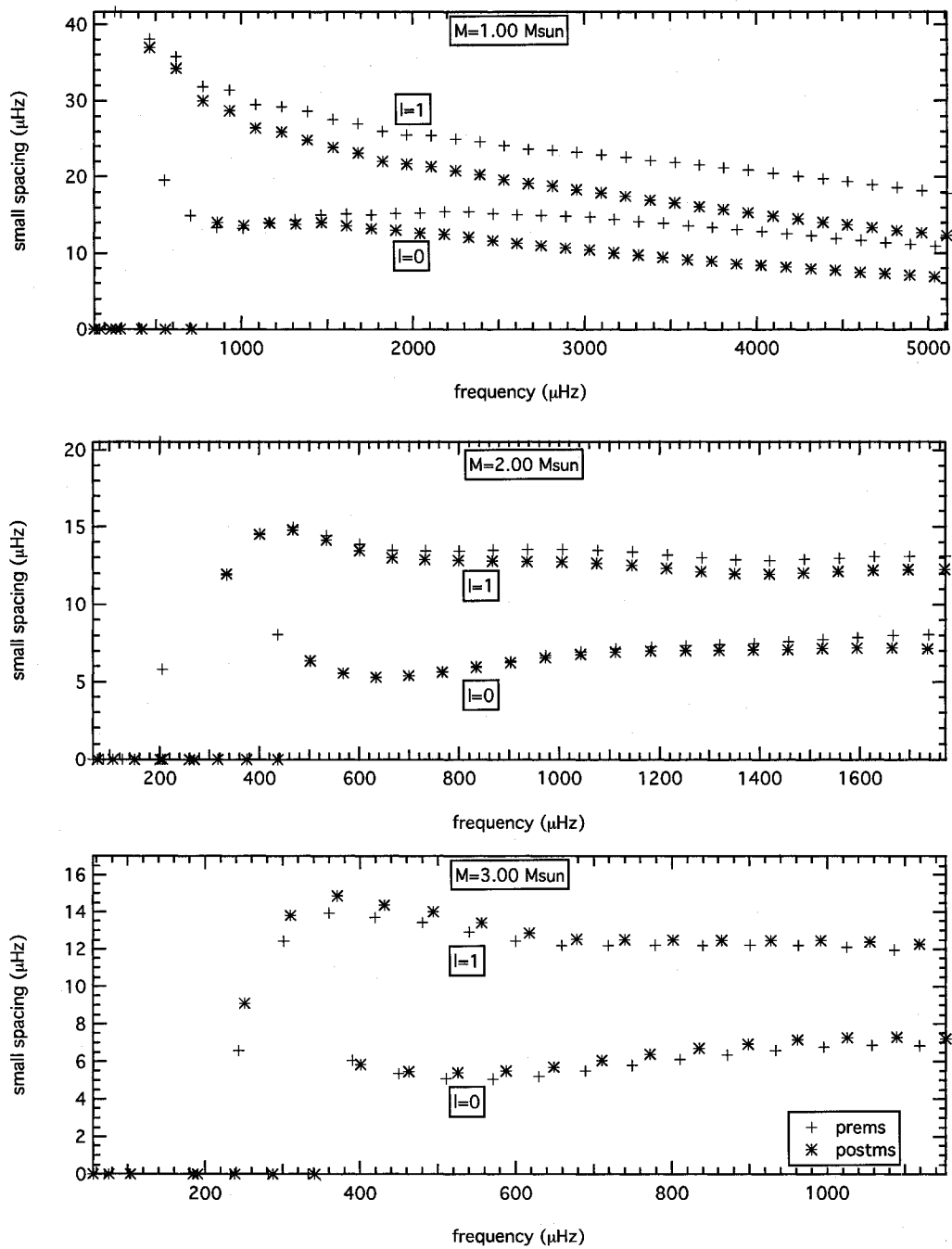
Figure 3.16 Small spacing vs frequency for 1, 2 and 3 M$_\odot$ models. Models correspond to the crossing of pre- and post-main sequence evolutionary tracks that is nearest the ZAMS.

Chapter 4

Analysis of P-mode Frequencies

Recall that the time dependence of complex non-adiabatic eigenfunction has the form:

$$\xi(t) \propto e^{i\omega t}, \tag{4.1}$$

where $\omega = 2\pi\nu$. From equation 4.1 we see than a negative imaginary component ($IM(\nu) <$ 0) in the frequency corresponds to a mode that is driven. Likewise, a positive imaginary component ($IM(\nu) > 0$) corresponds to a damped mode. The imaginary component of the non-adiabatic frequencies must be examined while affording proper consideration to the model physics, namely that modes were calculated taking into account radiative gains and losses and not convective-mode interactions (Guenther, 1994).

4.1 Non-Adiabatic P-modes

Examining the real component of frequency reveals the trend of p-mode frequencies with evolution, while the imaginary component indicates whether or not the mode is radiatively driven. In general, p-mode frequencies increase in conjunction with the contraction of radius through PMS evolution and then decrease through the subsequent expansion of radius

during evolution away from the ZAMS. In figures 4.1 and 4.2 we show non-adiabatic frequencies for a 3 $M_\odot$ evolutionary track with age set to zero at the ZAMS. In this convention, post-main sequence models evolve with a positive age, and pre-main sequence models are treated as initially having negative ages. The adiabatic and non-adiabatic frequencies are nearly identical throughout pre-and post-main sequence evolution. Although non-adiabatic and adiabatic frequencies differ the most at high n, this does not present a problem for modeling real oscillation spectra because the large spacings are preserved in both calculations. Matching an observed spectrum to adiabatic and non-adiabatic models will result in slightly different HR-diagram positions derived from the formal statistical best fit to each model, but this discrepency is smaller than typical observational uncertainties.

The gap in the evolution of non-adiabatic modes is a numerical artifact and a consequence of the way the pulsation code uses the adiabatic solution as an initial guess to solve the non-adiabatic equations. If the non-adiabatic eigenfunction is not sufficiently similar to the adiabatic solution, the code will fail to converge on a solution. To verify that the gap is indeed an artifact, the mode calculation was performed on tweaked models for select evolutionary sequences through the grid. The tweaked models in the gap region were found to be radiatively excited; this issue is discussed in greater detail by Guenther (2002) and is not pursued further here.

In figure 4.3, we show all frequencies for pre- and post-main sequence models of a 2 $M_\odot$ evolutionary track. The figure shows both real and imaginary components of non-adiabatically calculated frequencies for all modes from pre-main sequence through post-main sequence evolution. Mode frequencies are plotted against model number and age, with pre-main
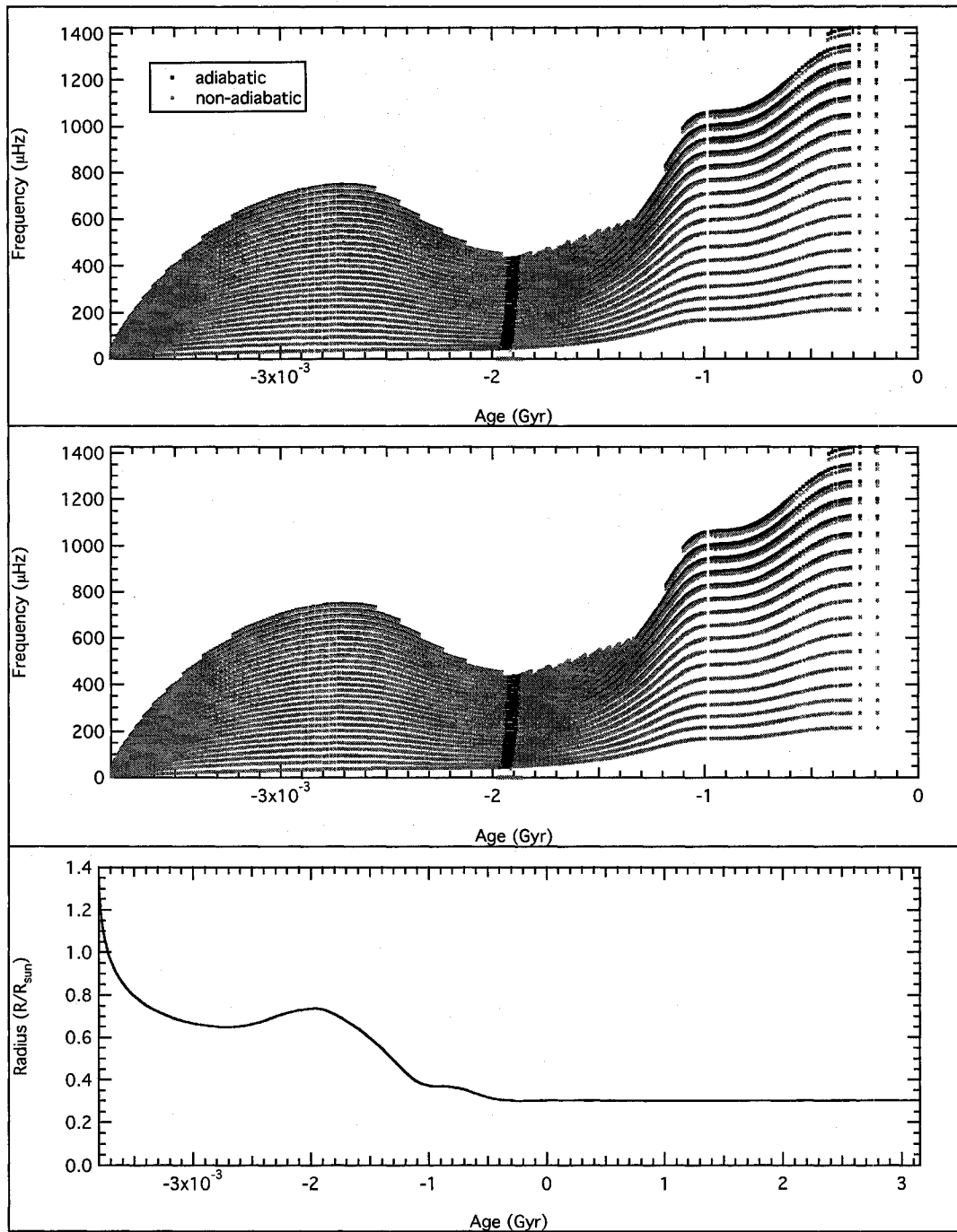
Figure 4.1 Adibatic and non-adiabatic frequencies for all models in a 3 $M_\odot$ PMS evolutionary sequence. The top and center panels show $l = 0$ and $l = 1$ frequencies changing with age, respectively. The bottom panel shows radius changing with age.
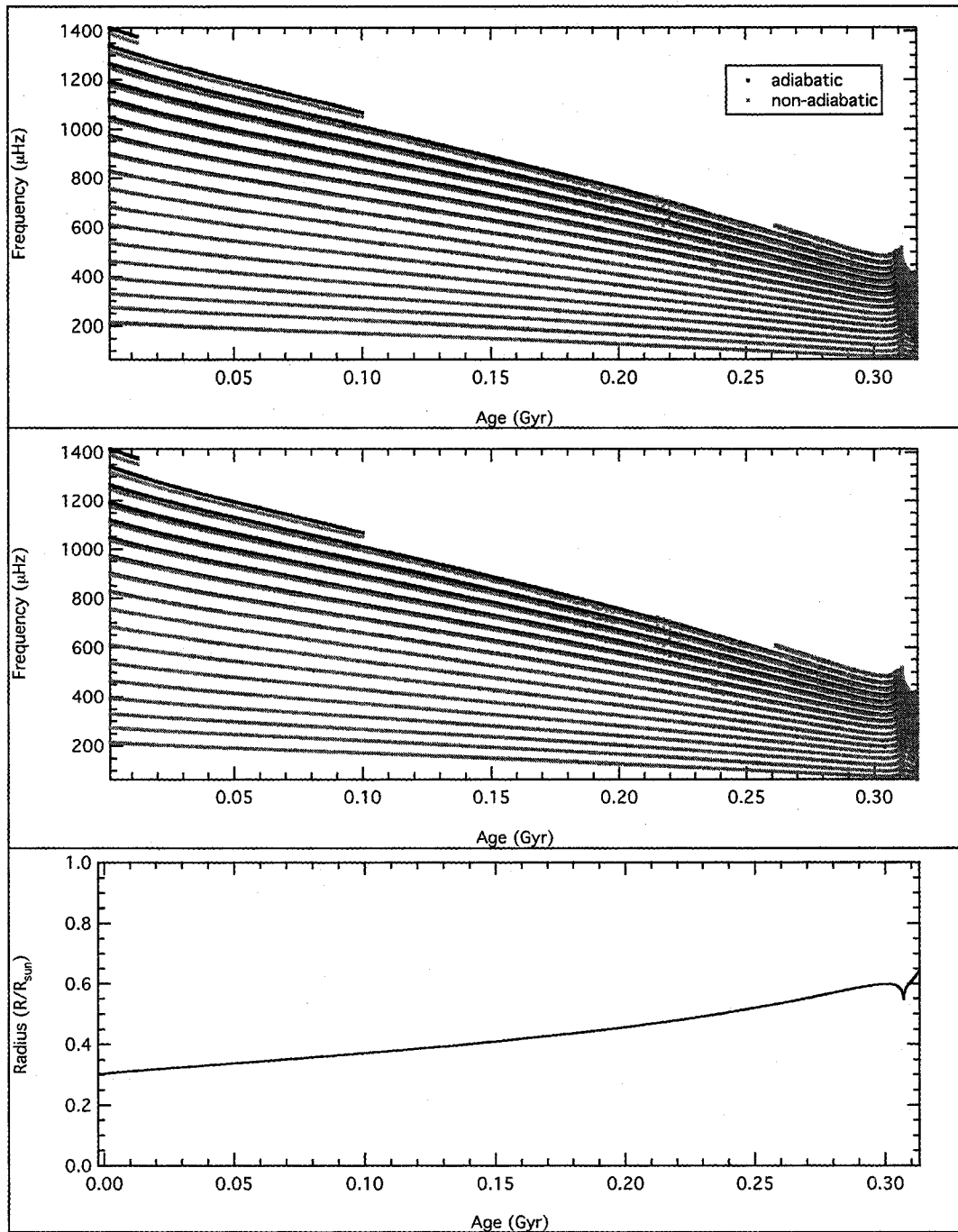
Figure 4.2 Adibatic and non-adiabatic frequencies for all models in a 3 M$_\odot$ post-main sequence evolutionary sequence. The top and center panels show $l = 0$ and $l = 1$ frequencies changing with age, respectively. The bottom panel shows radius changing with age.

sequence model numbers and ages defined to be negative and approaching zero at the ZAMS. The models are spaced in a uniform fashion in each stage of evolution, permitting the model number to be regarded in some fashion as proportional to evolutionary arc length in the HR diagram. Because the time steps are defined differently for pre- and post-MS evolution, the arc lengths differ for pre- and post-MS models but are self-consistent within each evolutionary regime. Note as well that the frequencies in the gap are not visible, but are expected to be radiatively excited. Common bands of excited modes exist in both stages of evolution, including the band corresponding to δ-Scuti stars.

4.2 The Instability Strip

To compute the theoretical instability strip we exploit the dense grid of computed PMS and post-MS evolutionary tracks. For each model, non-adiabatic pulsation calculations were performed, enabling driven modes to be detected. The resulting boundary of the instability strip is subject to the input physics of the models, the most important limitation being that modes are restricted to radiative gains and losses.

We show all PMS and post-main sequence models that have radiatively excited modes in figures 4.4 and 4.5, respectively. Darker regions indicate a higher number of radiatively excited modes regardless of degree or order. Both figures show a sharp increase in the number of possible radiatively driven modes for models that lie in the classical instability strip. Pre- and post- main sequence instability regions are coincident in HR diagram location, and the edge defined by a sharp rise in excited modes could correspond to the
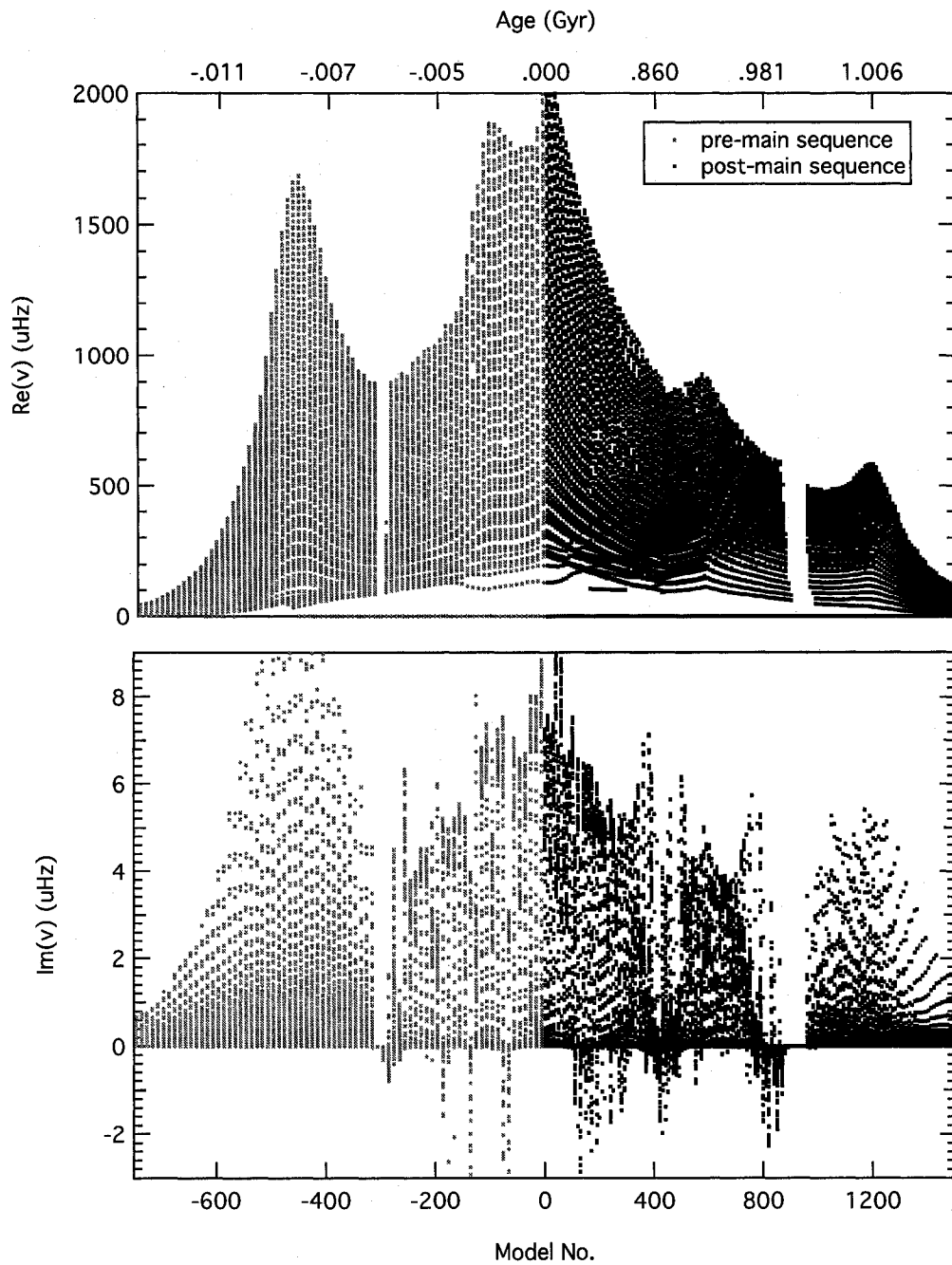
Figure 4.3 Real (top) and imaginary (bottom) components of non-adiabatic frequencies for 2 M$_\odot$ evolutionary tracks. The age of the models are shown on the uppermost axis. PMS model numbers and ages are presented as negative numbers with zero fixed at the ZAMS.

boundary of the instability strip. Figure 4.6 compares the instability strip boundaries derived from our models with the empirically determined edges and all the known PMS pulsators (Zwintz *et al.*, 2005b). The blue edge is in good agreement with the empirically determined edge, and in fact includes several PMS pulsators that the empirical blue edge does not. Because of the low number of observed PMS pulsators, the empirical PMS blue edge is not well determined. It is expected that convective effects determine the red edge, hence it cannot be accurately determined with these models. Nonetheless, the models confirm the possibility of radiaively-excited modes throughout the δ-Scuti instability strip, and include all PMS pulsators within its blue edge.

The instability region in figures 4.4 and 4.5 above was derived by examining models for radiatively excited modes of any l and n but the instability region can be further broken down into regions defined by radiatively excited modes for specific n and l. Performing the same analysis outlined above but separately on modes of degree $l = 0$ to $l = 3$ yields no significant global dependence on n or l.
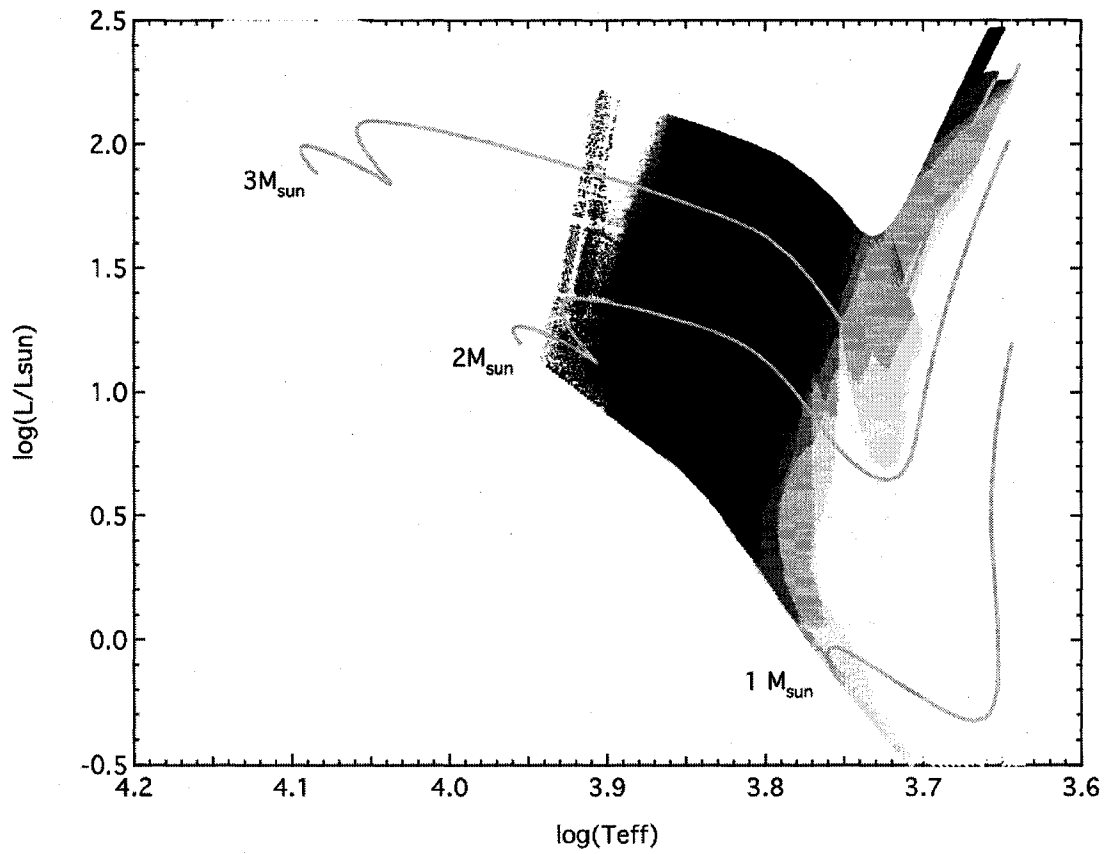
Figure 4.4 PMS models with modes that are radiatively driven. Darker shades indicate models with more driven modes.
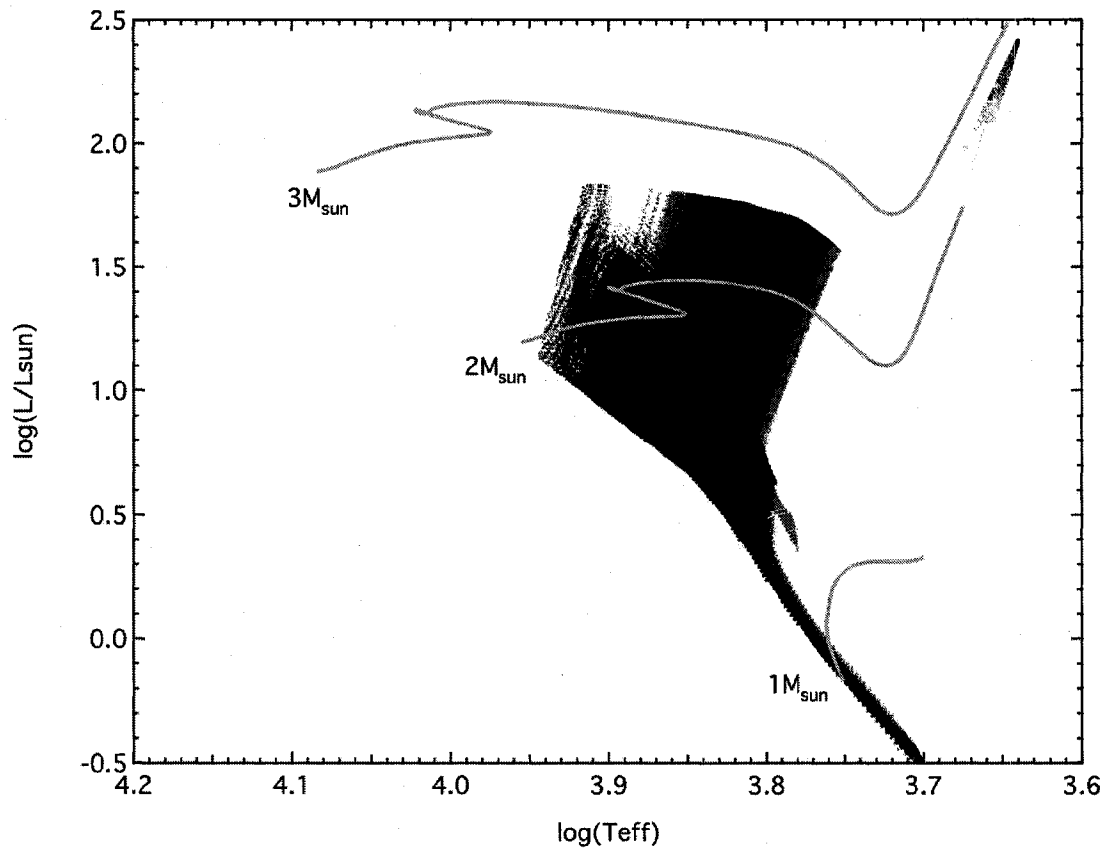
Figure 4.5 post-main sequence models with modes that are radiatively driven. Darker shades indicate models with more driven modes.

1 M ⊙
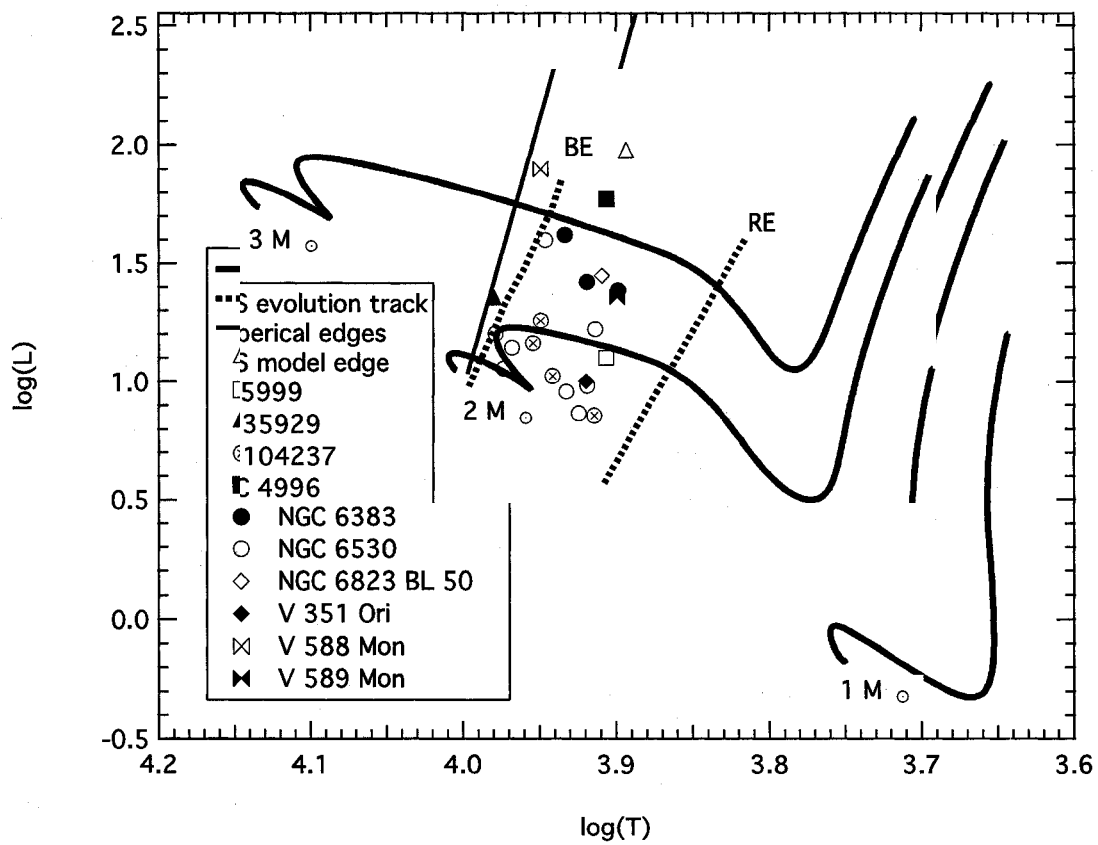
Figure 4.6 Empirical instability strip boundary compared with the boundary derived from our models. Known PMS pulsators are shown for reference.

Chapter 5

Pre-Main Sequence Isochrones

5.1 Computing Isochrones

The dense grids enable us to calculate very precise isochrones. From a coarse grid of models, Palla & Stahler (1990) computed isochrones that were accurate from the birthline through the horizontal evolution. Their isochrones have been successfully matched to observed young clusters (Guetter & Turner, 1997), but they were unable to resolve the features resulting from the structural correction caused by ^{12}C burning between the PMS ZAMS and the ZAMS. In this chapter, we present new PMS isochrones with improved resolution and match them with photometry from two young open clusters.

In figure 5.1 we present a sample of the isochrones computed from the PMS grid. The isochrones have been converted from luminosity and effective temperature to color and magnitude through the semi-emperical tables of Lejeune (1997). When computing post-main sequence isochrones, the zero age is defined by the ZAMS. This approximation is sufficient because post-main sequence lifetimes are much longer than the time required for star formation and PMS evoluton. Unlike post-main sequence evolution, PMS stars do not experience a similar stage of nuclear burning that halts evolution in the HR-diagram, so a

zero age must be defined in a different way. Palla & Stahler used the birthline (section 1.1) as the zero age, but this location is uncertain due to a high sensitivity to mass flow rates. For our calculation, we define the zero age as the point where nuclear burning accounts for 0.1% of the total generated energy. The new isochrones are in good agreement with those of Pallah & Stahler, with the chief difference being the resolved nuclear burning "bump" near the ZAMS in the final stages of PMS evolution. The absolute ages are offset by a factor corresponding to the difference between our zero age and the birthline used by Pallah & Stahler. Due to the uncertainty inherent in the definition of the birthline, this discrepancy is not pursued further. At cooler temperatures, the agreement between our isochrones and those of Palla & Stahler breaks down, which is primarily a consequence of the Eddington approximation that we employ in our calculations of the atmosphere. Differences between our adopted zero age and the birthline defined by Palla & Stahler do not contribute significantly to the discrepancy at cool temperatures.

For stellar evolution calculations, the atmosphere is constructed from temperature laws derived from theory or from full atmosphere calculations. Because the temperature law depends on temperature and gravity, it is contingent on the evolutionary state of the model. Inside a stellar model, the medium is optically thick and the radiative flux can be derived from the diffusion approximation:

$$H_\nu \approx \frac{1}{3} \frac{dB_\nu}{d\tau_\nu}, \tag{5.1}$$

where H_ν is the second momentum of the monochromatic specific intensity, B_ν is the monochromatic Planck function, and τ_v is the optical depth. This approximation becomes valid at large optical depths (ie: many mean free paths) because it requires thermody-
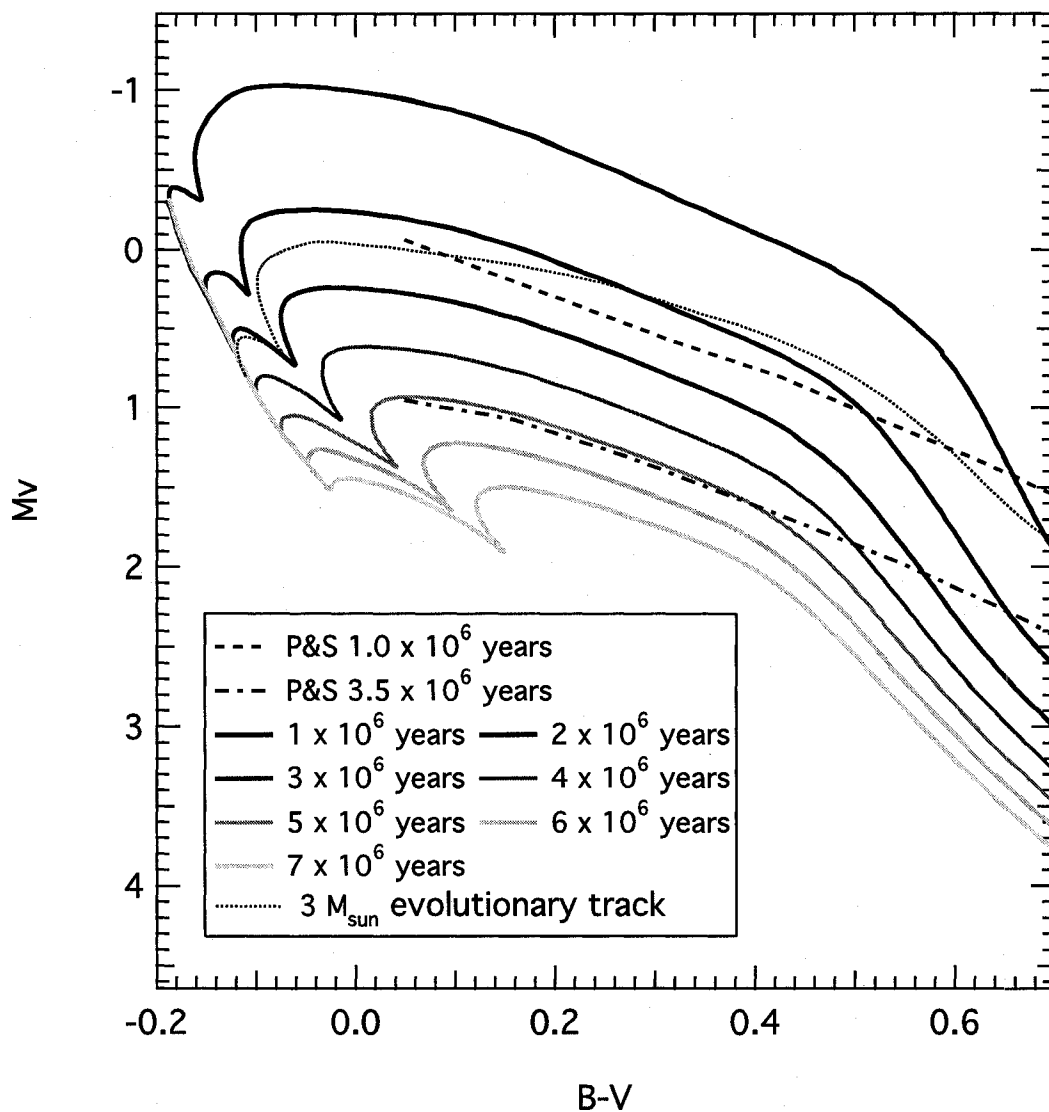
Figure 5.1 A sample of isochrones derived from the dense grid of solar abundance pre-main sequence models. Two isochrones derived from the models of Palla & Stahler (1993) are included for comparison. A 3 $M_\odot$ PMS evolutionary track is shown for reference.

namic equilibrium. Typically, the internal structure is calculated separately from the outer regions, where a simplified atmosphere calculation is employed. The two must meet at a location with an optical depth that is at a large enough Rosseland mean optical depth for the diffusion approximation to be valid, often taken to be $\tau = 2/3$. Several elements contribute to the inadequacy of the gray atmosphere approximation, the first of these being that the diffusion limit of the transfer equation used in stellar structure is only valid at Rosseland mean optical depths much greater than $\tau = 2/3$. Morel *et al.* (1994) found the diffusion approximation to be valid at optical depths down to $\tau \approx 10$, which falls within the convection zone for the sun. Second, onset of convection is affected by frequency dependant opacities so that errors are introduced in the effective temperature and colors of low mass stars under the gray approximation (Baraffe *et al.*, 1995). For more accurate computation of stellar models, the boundary conditions at the surface of our models should be supplied by a more realistic atmosphere that takes into account the opacity frequency dependence and convection.

The profile of PMS isochrones is more sensitive to evolutionary state than isochrones that trace a post-main sequence population. Because the PMS evolution proceeds rapidly, the ambiguity of zero age as well as range of ages in a given stellar population contribute to the uncertainty of the isochrone. Post-main sequence isochrones are matched to photometric data of star clusters with the presumption that the stellar population has a singular age. Under this scenario, the stars in the cluster began in a single burst of formation. Although the formation is not truly instantaneous, it is not important for post-main sequence isochrones because the epoch of star formation is small relative to the nuclear burning life-

time on the ZAMS. However, our isochrones show that a starburst formation that lasts even 0.5 million years contributes significantly to the uncertainty in a PMS isochrone.

Our isochrones include uncertainties that reflect non-instantaneous star formation and the uncertainty in defining the birthline. We approximate this by taking the isochrone uncertainty to be time from the end of mass accretion to our zero age. We also present our isochrones as a region in the HR-diagram rather than a discrete line, with the width of the region determined by the uncertainty. The younger isochrones are prone to have larger width because the more massive stars require less time to contract to the ZAMS. Two examples of these isochrones are displayed in figure 5.2.

We compare our isochrones to the young open clusters IC 1590 and NGC 2264. Fitting them to photometry is not intended to be a rigorous examination of cluster age, rather, it provides a comparison of our isochrones with the labors of several other authors and highlights the large uncertainties in PMS isochrones.

5.2 IC 1590

The distance to IC 1590 is based on identified ZAMS cluster members and has been determined by Guetter et al. to be 2.94 ± 0.15 kpc, with a corresponding distance modulus of $V_o - M_v = 12.34 \pm 0.11$. When adjusted for this distance modulus, our isochrones match the hot stars well and conform with Pallah & Stahler's isochrones at hot temperatures. Guetter & Turner (1997) estimate a maximum age of $3.5 \cdot 10^6$ years by identifying an
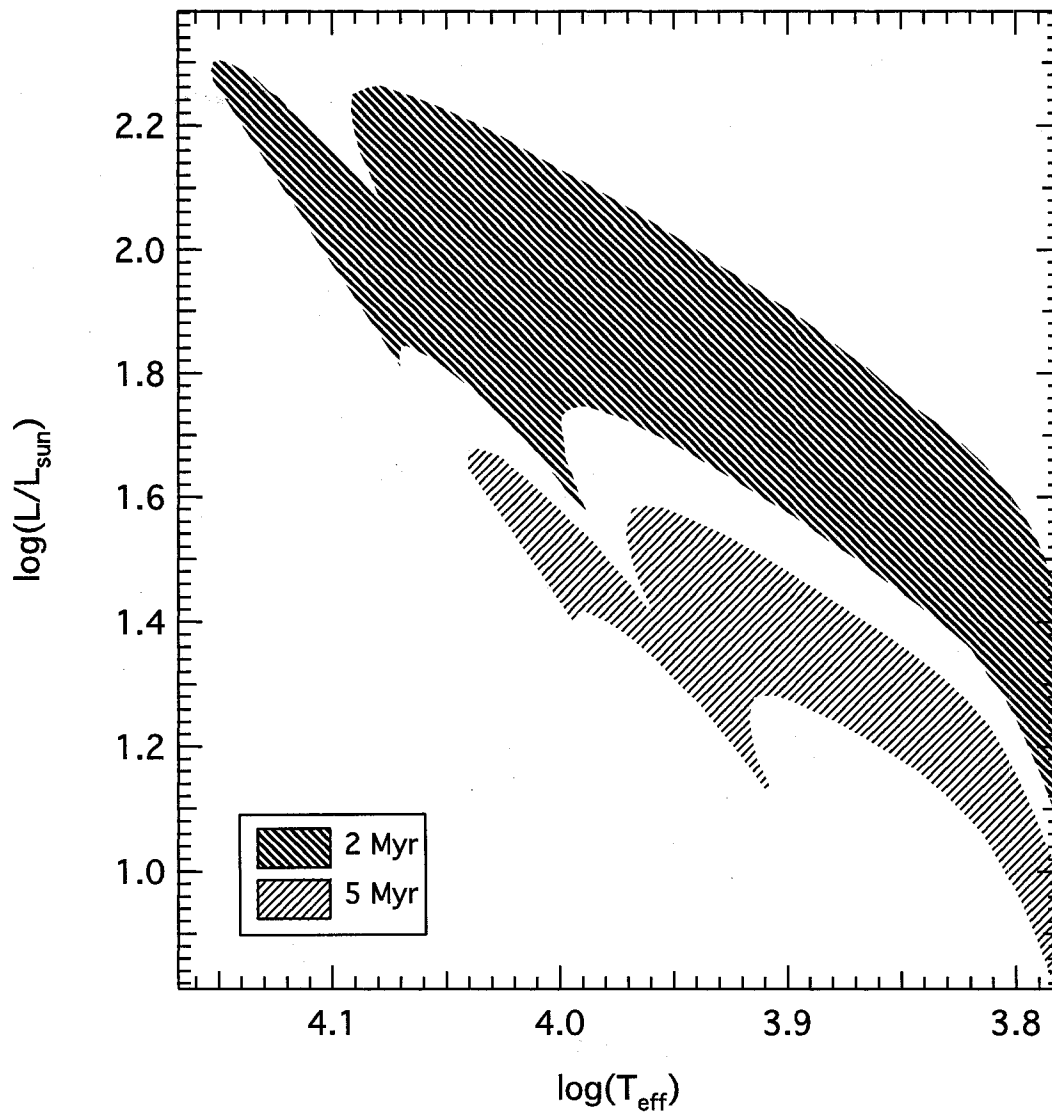
Figure 5.2 PMS isochrones for ages of $2 \cdot 10^6$ and $5 \cdot 10^6$ years with uncertainties included. Younger isochrones include massive stars that evolve faster so the uncertainty is larger in the HR-diagram.

O-type trapezium system in the cluster. The width of our isochrone all but spans the observed range in color and magnitude of the cluster members, and from it we estimate the age of the cluster to be $3.0 \pm 1.0 \cdot 10^6$ years. Our age estimate is in agreement with previous work, and in particular, the large uncertainty underscores the limitations of PMS isochrones arising from the weakly defined zero age.

Because the resolution of our isochrones is higher than any other published isochrones, we can resolve the ^{12}C hook onto the ZAMS. *When compared to observations we can see this in the cluster as a widening of the ZAMS toward lower mass stars.* Scatter outside of the predicted widening from the isochrones could be attributed to a number of factors, including binarity, contamination from circumstellar disks, or rotation (Roxburgh & Strittmatter, 1965). In fact, Guetter & Turner point out that the 13 pre-main sequence stars lying above Pallah & Stahler's $3.5 \cdot 10^6$ year isochrone fall within the difference corresponding to an unresolved pair of equally-bright stars or to contamination light equal to that of the star from a circumstellar disk. Further, spectroscopic observations indicate that rapid rotation is relatively common among the main sequence cluster members.

5.3 NGC 2264

Discovered by Breger (1972), NGC 2264 includes the earliest examples of PMS pulsators (V588 Mon and V589 Mon), and is a target in the ongoing COROT mission. The age of NGC 2264 has been estimated by the main sequence turn-off as approximately $1.5 \cdot 10^6$ years by Sung *et al.* (1988), however most stars in the cluster are in the PMS stage. The
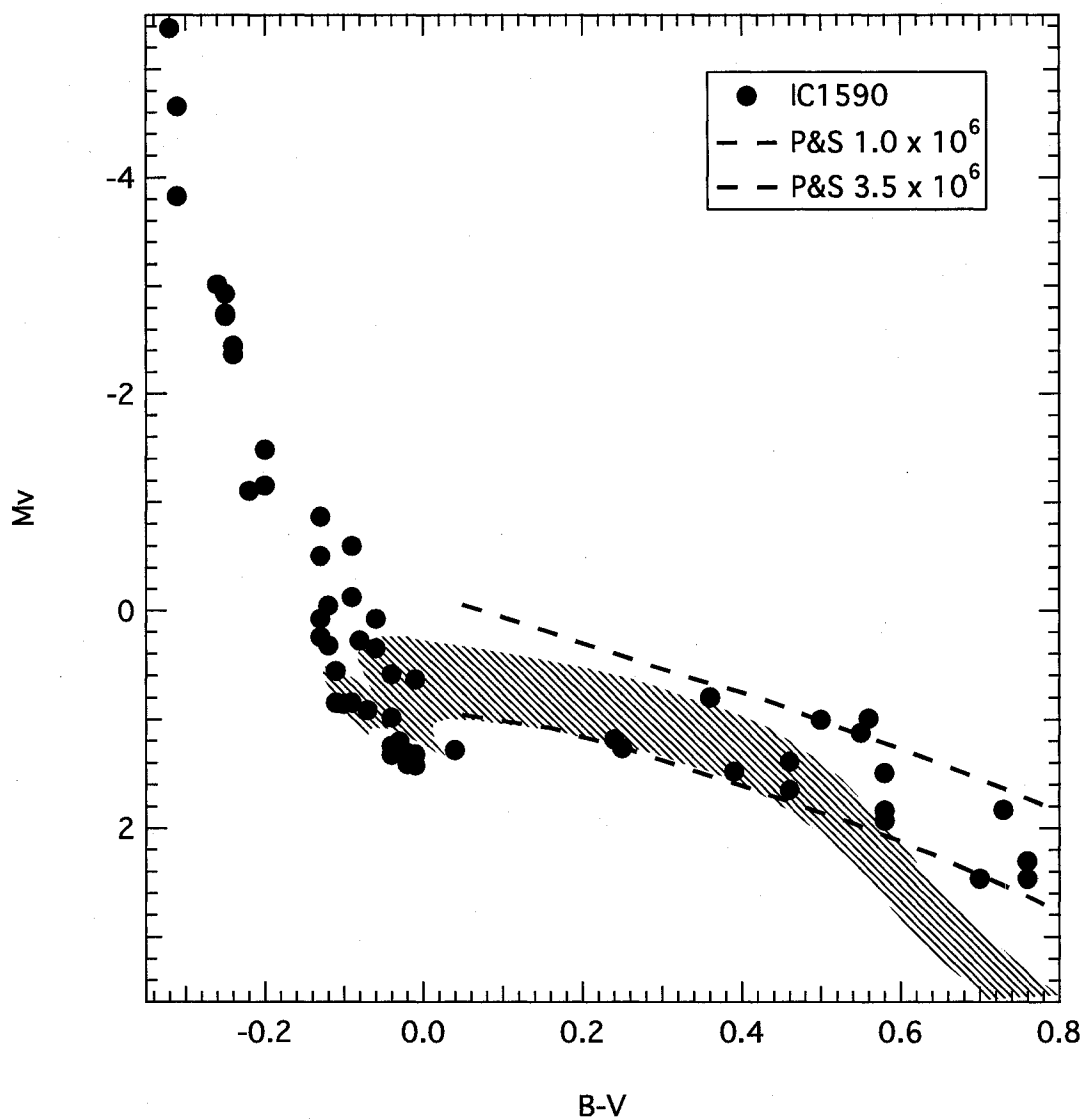
Figure 5.3 Color-corrected photometric data (Guetter & Turner, 1997) of the open cluster IC1590 showing a $3.0 \cdot 10^6$ year isochrone with uncertainty. Bracketing the data are isochrones of Palla and Stahler at $1.0 \cdot 10^6$ and $3.5 \cdot 10^6$ years.

photometry presented here has been de-reddened by Turner (private communication) using an improved reddening solution. An isochrone of $5 \cdot 10^6$ years provides a satisfactory fit to the data but the scatter in the photometry allows for isochrone ages as young as $2.5 \cdot 10^6$ years. Age estimates for this cluster range from $1 \cdot 10^6$ to $5 \cdot 10^6$ years. In particular, the age determination of Park *et al.* (2000), which is based on isochrones derived from the models of Swenson *et al.* (1994), is significantly younger than ours but the data used by Park *et al.* suffers from larger scatter, resulting in an uncertainty of a few million years. The increased scatter could be due to incorrect member identification and the applied de-reddening technique, and it is worth noting that while Park *et al.* employed individual reddening corrections for massive stars, a mean reddening correction was used at low and intermediate masses. The discrepancy in the age estimates could also be attributed to differences in the models, specifically the opacity and treatment of convection. Results of a comparative study by Hillenbrand (1997) of the PMS models of D'Anotona & Mazzetelli (1994) and Swenson *et al.* (1994) suggest that convection and opacities can significantly alter the models of low mass stars, but have less of an effect on higher masses. Our models compare well with those of D'Anotona & Mazzetelli (1994). Regardless of specific ages for NGC 2264, the large range in age estimates underscores the uncertainty that is inherent in PMS isochrones, whether it is from photometry or stellar models. Neglecting the ambiguity of the zero age, age estimates for PMS populations in young clusters remain uncertain, which is a consequence of the short time scales on which they evolve coupled with non-instantaneous star formation. Ultimately, PMS isochrones should not be interpreted as distinct ages, but rather as limits on the epoch of star formation and the uncertainties therein.
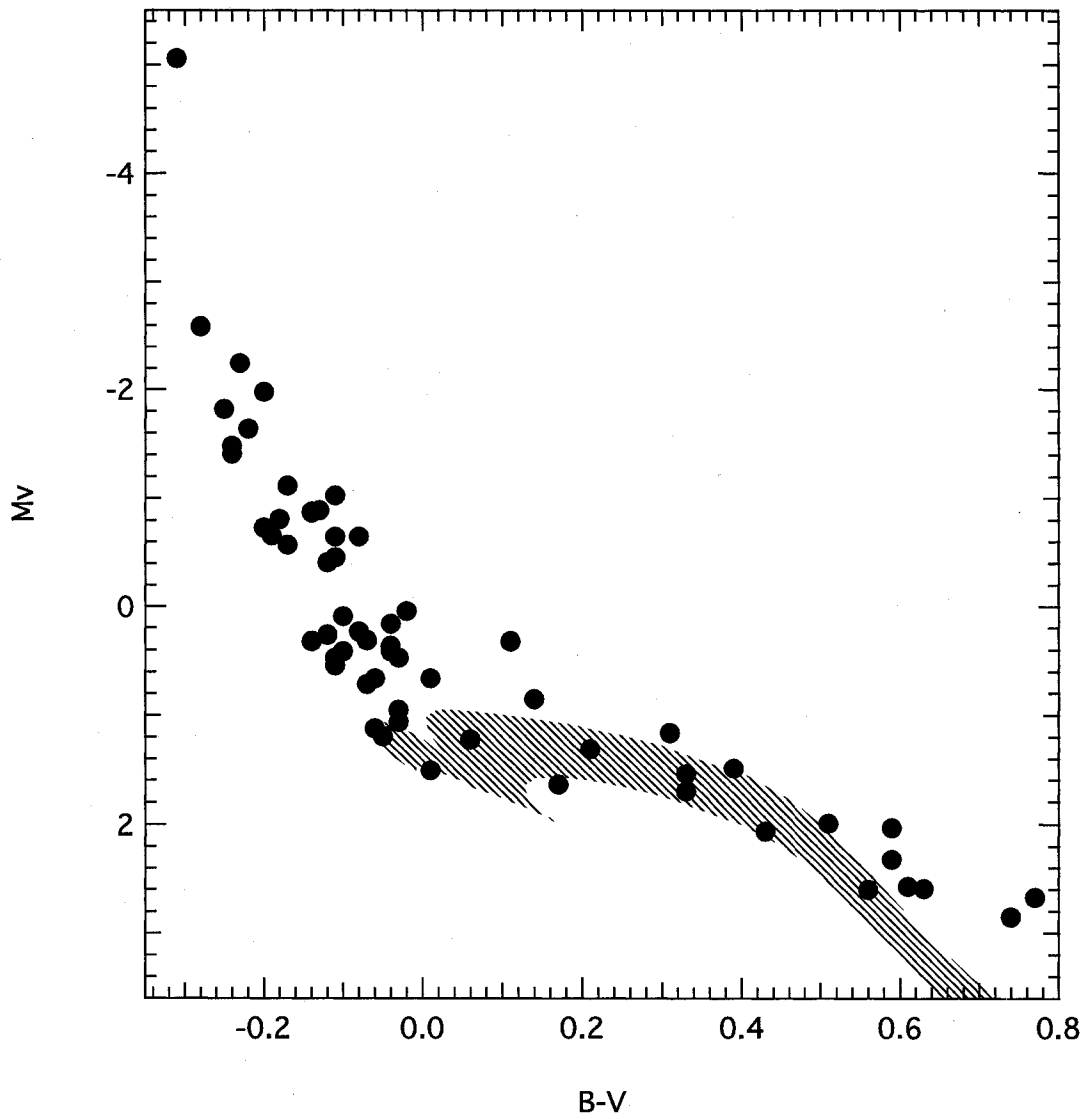
Figure 5.4 Color-corrected photometric data (Turner, 2007) of the open cluster NGC 2264 showing a $5.0 \cdot 10^6$ year isochrone with uncertainty.

Chapter 6

Pre- and Post-main Sequence Oscillation Spectra

In this chapter we probe our ability to use asteroseismology to constrain properties of PMS stars. We endeavor to determine whether an oscillation spectrum can reveal the evolutionary phase of a star, and how well stellar properties can be constrained as a function of the number of observed modes and their uncertainty. To address these questions we construct artificial 'observed' oscillation spectra, that is, spectra taken from our models to which we have perturbed the frequencies to mimic observational uncertainties. We characterize our artificial spectra by two parameters: the number of frequencies and the uncertainty in the frequencies. We examine how well we can locate the model in the grid that corresponds to the artificial spectrum for a variety of artificial spectra. When the uncertainties are high or the number of frequencies are low we expect the ability to unambiguously constrain the model to deteriorate.

6.1 Synthetic Oscillation Spectra

We generate a small sample of artificial PMS oscillation spectra corresponding to 'observed' stars at two locations in the HR diagram. We assess the usefulness of each spectrum by comparing the matched models (the models whose oscillation spectra match the artificial spectrum within the uncertainties) to the model used to produce the artificial spectrum. Basic properties for each of our test models is presented in table 6.1.

Table 6.1 Properties for the PMS stars selected as templates for generating the synthetic test spectra.

	star1	star2
$Log(T_{eff})$	3.85	3.87
$Log(L/L_\odot)$	1.35	1.76
$log(R/R_\odot)$	0.49	0.67
$Mass(M_\odot)$	2.10	2.90

We construct each artificial spectrum with a randomly selected subset of frequencies taken from a complete computed model, with the frequencies randomly perturbed. Frequencies below the acoustic cutoff are randomly selected with no preference given to models of any particular l or n. We then compare this frequency spectrum to the complete oscillation spectrum of each model in the pre- and post-main sequence grids. We measure the quality of a match by the χ^2 relation:

$$\chi^2 = \frac{1}{N} \sum_{i=1}^{N} \frac{(\nu_{obs,i}^2 + \nu_{mod,i}^2)^2}{\sigma_{obs,i}^2 + \sigma_{mod,i}^2},\tag{6.1}$$

where $\nu_{obs,i}$ is the observed frequency for the ith mode, $\nu_{mod,i}$ is the corresponding model frequency, $\sigma_{obs,i}$ is the observational uncertainty for the ith mode, and N is the total number of modes that are matched observed frequencies. The model uncertainty $(\sigma_{mod,i})$

is estimated from fitting models to the solar oscillation spectrum (Guenther & Brown, 2004). We assume that all modes in the 'observed' spectrum are real, that is, we make no allowance for contamination from instrumental effects, or misidentified modes. Values of χ^2 below 1.0 are deemed to be a good match, and all good models comprise the solution space that can further constrain stellar properties beyond the HR-diagram constraints. Each good model presents a possible solution for the structure of the star, so fewer good models represent better constrained properties. To avoid spurious results from a single artificial spectrum we derive 50 artificial spectra from each of the template stars in table 6.1. We construct artificial spectra with the number of frequencies ranging from 5 to 20. In total 750 specta were created for each template star.

6.1.1   Results of Mode Matching

We explore how the solution space is affected by the precision and size of the artificial frequency spectrum by fitting frequency spectra derived from *star1* and with 4 different imposed uncertainties: 1.5, 1.0, 0.5 and 0.25 μHz. The artificial spectra are fit to grid models that lie within $\Delta log(T_{eff}) = 0.10$ and $\Delta log(L/L_{\odot}) = 0.50$ of the template model. Figure 6.1 presents an echelle diagram for a single artificial spectrum derived from *star1* and two models that most closely match it. In this example, the artificial spectrum has an uncertainty of 1.0 μHz and is matched very well by both pre- and post-main sequence models.

In figure 6.2 we show an example of the solution space from fitting one of the artificial
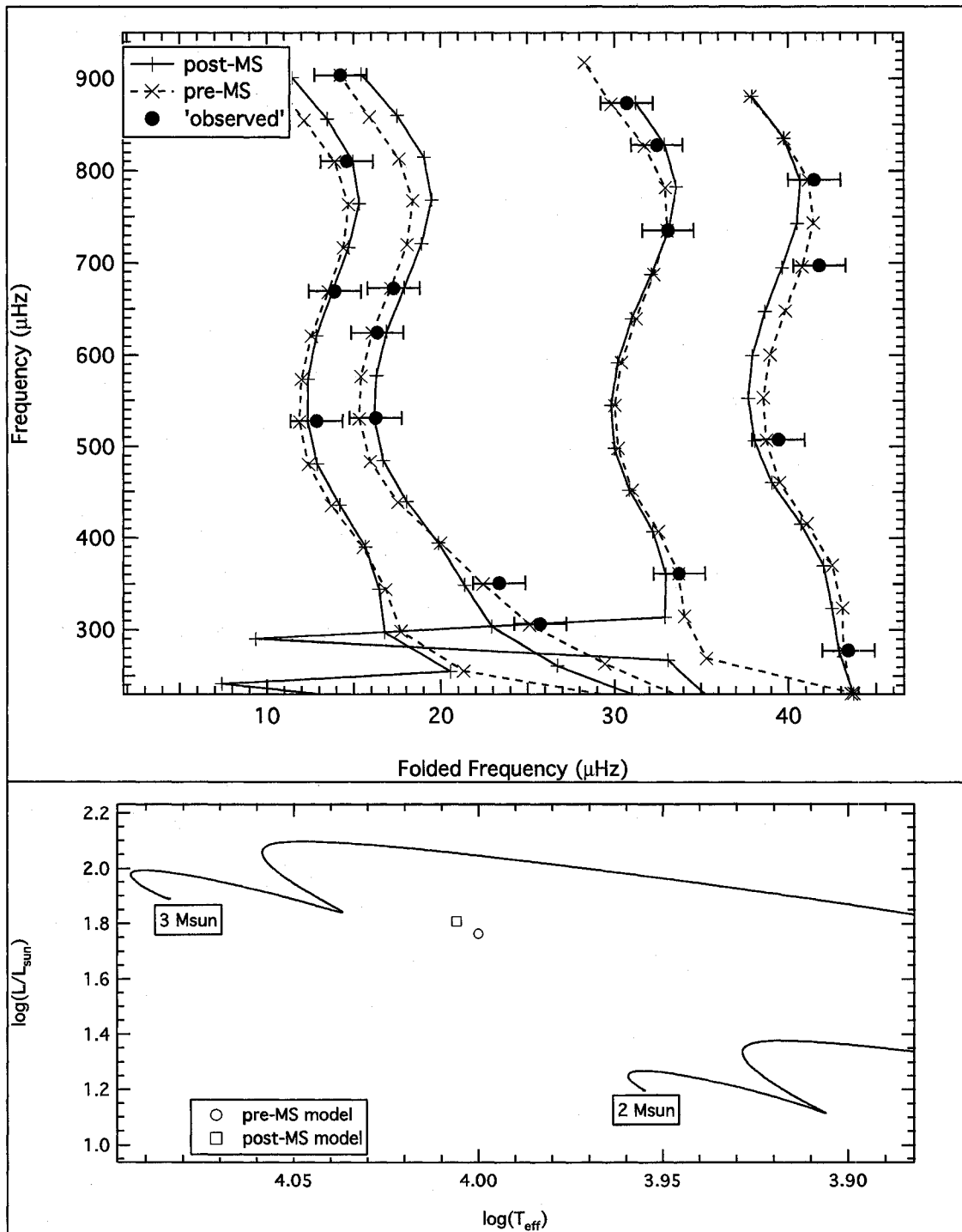
Figure 6.1 Echelle diagram showing an artificial oscillation spectrum matched to the frequencies of two models in the grid. HR-diagram locations for both models are indicated in the lower panel.

spectra with an uncertanty of 1.0 μHz to the PMS grid. Each panel corresponds to an artificial spectrum with a different number of frequencies (N). As N increases, the good models form a solution space that groups around large spacings that match. With a high enough N, the solution space is reduced to a group of models representing a single large spacing.

We present the results in figure 6.3 by plotting the number of good models (models that match with $\chi^2 < 1$) against the number of modes in the artificial spectrum. Since the models in the grid are not uniformly distributed throughout the HR-diagram we normalize our results. Specifically, the number of good models is normalized by the number of models that lie within $\Delta log(T_{eff})$ and $\Delta log(L/L_{\odot})$ of the template model HR diagram position. Figure 6.3 presents the average result from comparing the 50 synthetic spectra derived from *star1* to the grid. The number of good models from comparing an individual artificial spectrum to the grid is sensitive to the specific modes that it comprises, and can differ significantly from the average results we present here. We note that the ability to constrain stellar properties from oscillation frequencies depends to some degree on what modes are observed, but do not pursue this issue further.

For artificial frequency spectra with large uncertainties (> 1 μHz) the number of good matches is high. When the uncertainties in the artificial spectra exceed 1 μHz we cannot distinguish between PMS models and post-main sequence models. This is true regardless of the number of frequencies in the spectrum of the test model. We find that the size of the solution space as a function of the number of 'observed' frequencies is sensitive to the specific modes in the artificial spectrum. Recall that this result is based on the average
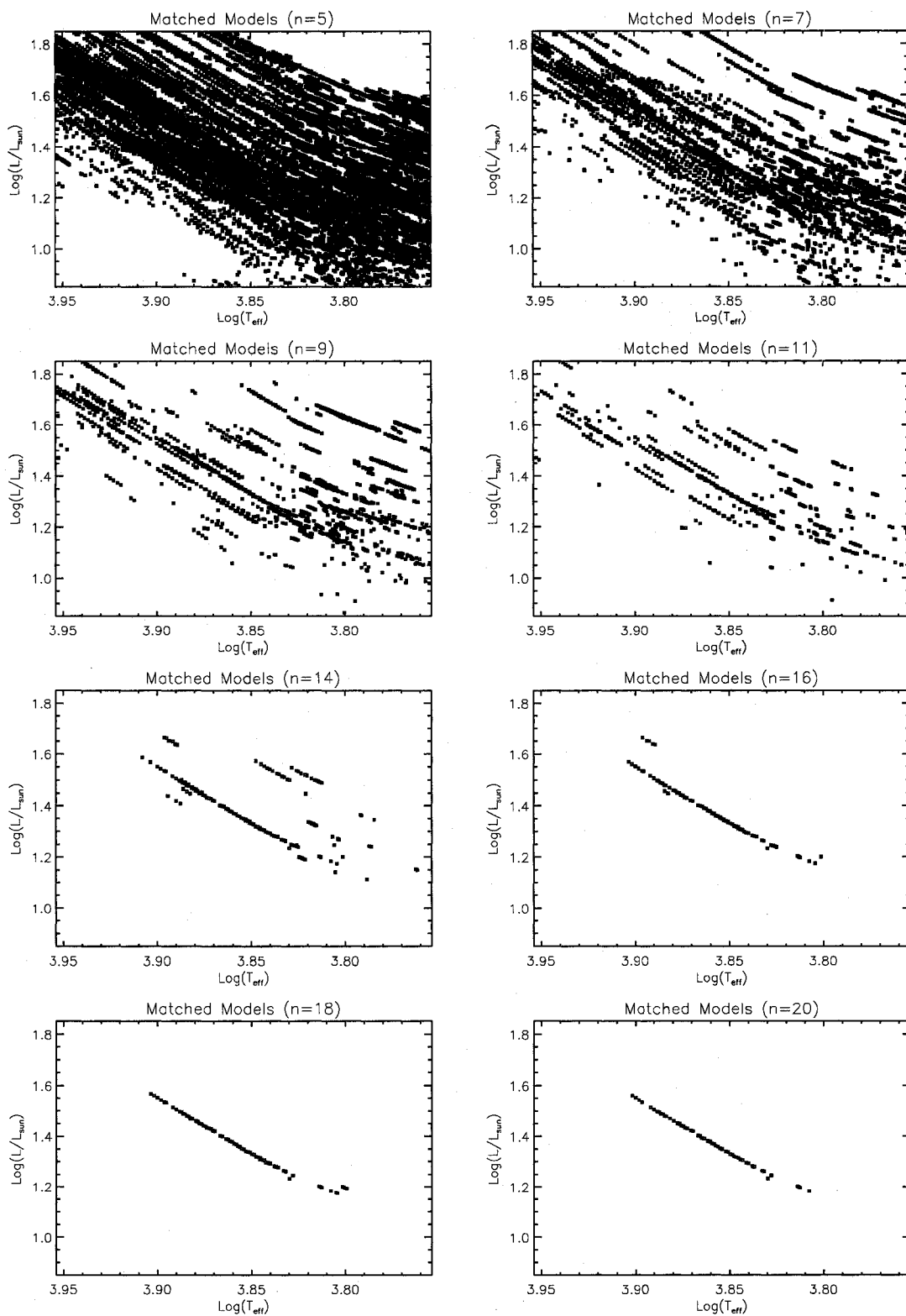
Figure 6.2 HR-diagram positions of PMS models that provide a good match to an artificial spectrum. Each panel shows models that match an artificial spectrum with a different number of frequencies (indicated with n).

solution space from the 50 artificial spectra and the results we present here reflect the most probable scenario. Also, the situation may be different for stars located farther away from the ZAMS where mode bumping plays a more important role. For the two stars considered here, matches to model frequency spectra occur by chance. Many of these chance matches are eliminated by improving the precision of the artificial spectrum. Without a measure of the large spacing to constrain the models, the solution space nearly covers the entire region of interest defined by the uncertainty in $log(T_{eff})$ and $log(L/L_\odot)$. Further, the frequency spacings decrease for models far from the ZAMS, making it more likely to have a match of low frequency modes.

For the artificial frequency spectra with smaller uncertainties, we find the number of good post-MS models drops faster with more frequencies in the spectrum. For artificial spectra with 11 or more frequencies and low uncertainty ($\Delta\nu < 0.25$ μHz) the 'observed' star was always identified as PMS from the oscillation spectrum. For artificial spectra with fewer or less certain frequencies, the 'observed' star was identified as PMS only some of the time. Again, whether or not the evolutionary stage of the star can be determined from the oscillation frequencies is sensitive to the specific modes that comprise the artificial spectrum.

For PMS models, we find the good models form a solution space that is typically distributed in several regions, with those in each group having similar large spacing. This is the chief difference between PMS and post-main sequence asteroseismology: the simpler structure and oscillation spectra of PMS stars often yields discrete groups of matched models, with the individual models in each group being of similar structure. Reducing the artificial

spectrum uncertainty causes the number of matched models to converge on a smaller solution space that includes the template model. The size of the solution space and whether it uniquely represents the template model depends on the uncertainty of the artificial spectrum.

Although constraining stellar properties through oscillation frequencies depends on the specific modes that are observed, the results of the χ^2 fitting for *star1* reveals several important results. For artificial spectra with uncertainties > 1.0 μHz, the solution space is large and it is difficult to establish any meaningful constraints on the observed star. Further, with enough frequencies in the artificial spectrum, the solution space will converge on a region in the HR diagram occupied by models with similar large spacings. Reducing the solution space further is accomplished most effectively by reducing the uncertainty of the frequencies rather than increasing the number of frequencies. For artificial spectra with uncertainties < 0.50 μHz, increasing the number of frequencies beyond 8 does not significantly reduce the size of the solution space. This is especially encouraging for ground-based observations, which can observe frequencies to this level of precision and can typically detect up to 10 frequencies.

To explore the sensitivity of the results from *star1* on the location in the instability strip, we select a second template star. This star is more massive and at a younger evolutionary stage, placing it in the more luminous and cool part of the δ-Scuti instability strip. We fit 50 synthetic spectra with uncertainties identical to those imposed imposed on the synthetic spectra of *star1*. The results of the PMS grid fitting are presented in figure 6.4. Here again, the trend reveals that the number of matched modes decreases and converges with
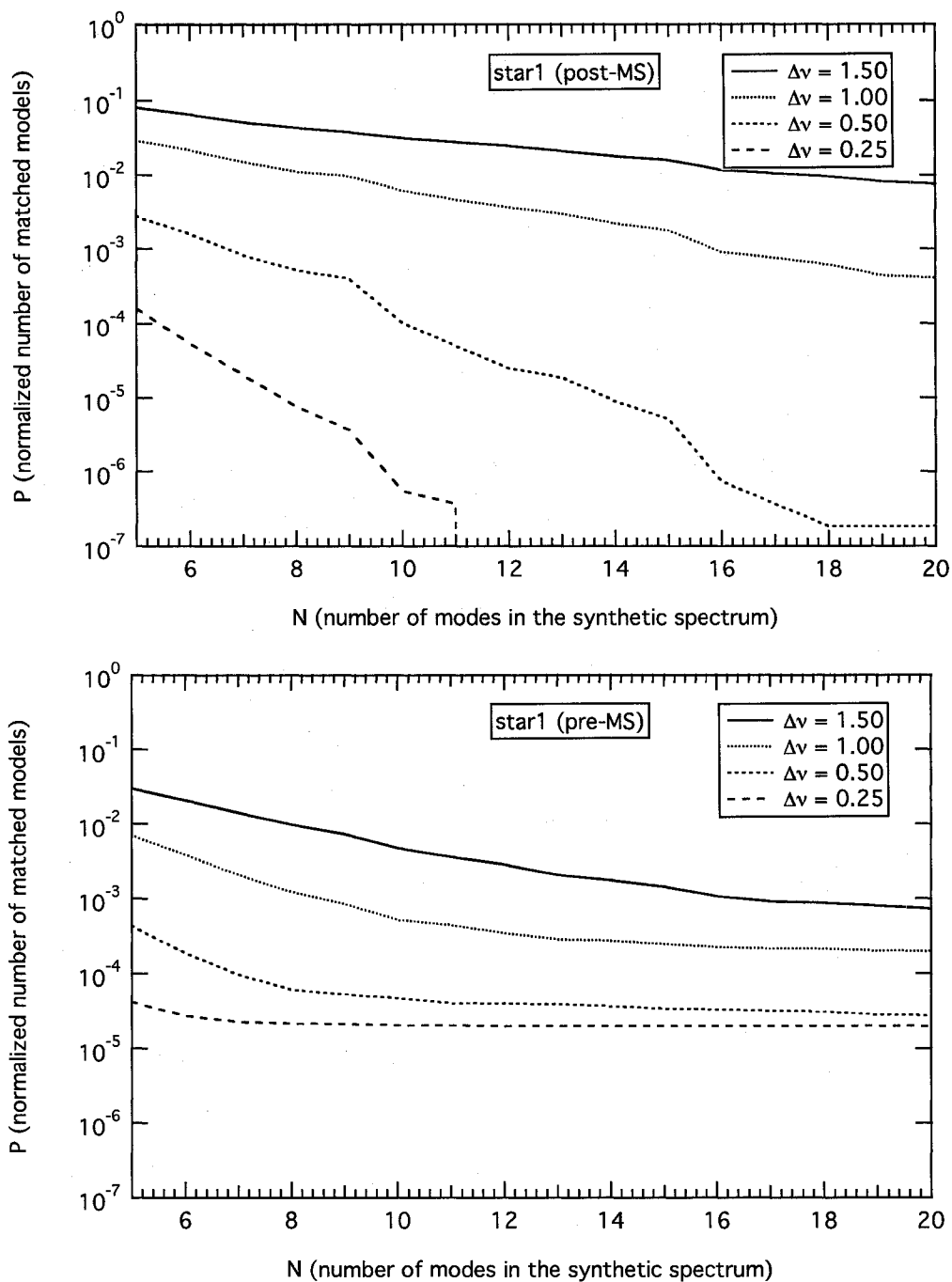
Figure 6.3 Results from comparing artificial spectra derived from *star1* to the PMS and post-main sequence grids. The number of models that matched the artificial spectrum is shown as a function of the number of frequencies in it. The number of matched models has been normalized by the number of models that lie within $\Delta log(T_{eff})$ and $\Delta log(L/L_\odot)$. Lines correspond to artificial spectra with a different uncertainties.
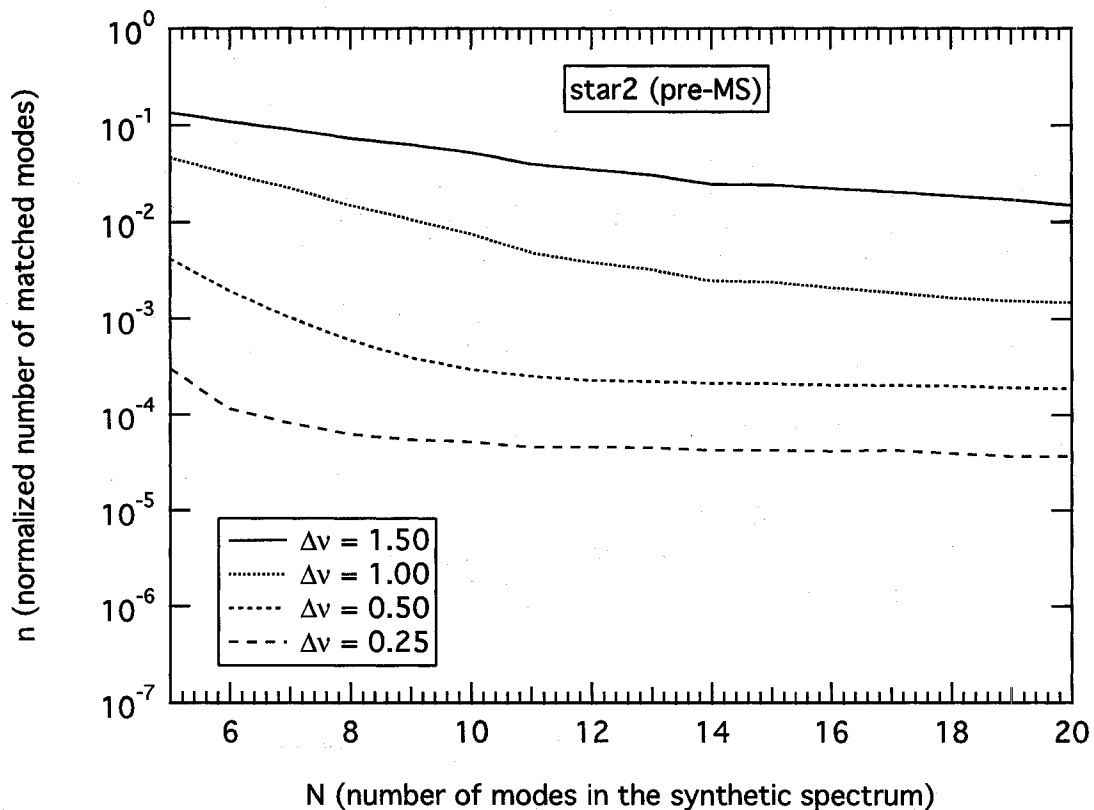
Figure 6.4 Results from comparing artificial spectra derived from *star2* to the PMS grid. The number of models that matched the artificial spectrum is shown as a function of the number of frequencies in it. The number of matched models has been normalized by the number of models that lie within $\Delta log(T_{eff})$ and $\Delta log(L/L_\odot)$. Lines correspond to artificial spectra with a different uncertainties.

increasing number of frequencies on a set of models surrounding the template star. The primary difference here is that more models match *star2* than *star1* for synthetic spectra with the same number of modes and uncertainty. This is an expected result because the frequency spectrum compresses as the radius increases (figs. 4.1 and 4.2), requiring higher quality data to distinguish models. The precision of an observed frequency spectrum necessary to constrain stellar properties is related to the average large spacing presented in figure 3.2.

We find that in both tested cases (*star1* and *star2*), reducing the scope of the solution space is achieved faster through increasing the accuracy of the observed frequencies rather than the number of frequencies in the observed spectrum. That is to say, *the successful use of asteroseismology as a tool for constraining stellar properties is primarily dependent on the quality of the modes rather than the quantity.*

Chapter 7

Modeling Real Stars

Although the results from model comparisons in chapter 6 are encouraging for using asteroseismology to constrain properties of PMS stars, the results are based on artificial oscillation spectra. These oscillation spectra were constructed from existing PMS models, which suffer from none of the effects of real world astronomy. When working with real oscillation data, allowances must be made for false modes from instrumental effects or aliasing. Also, rotation may split modes so that several frequencies exist where the model only has one. In this chapter, we demonstrate that constraints can be imposed on real PMS stars. Our results reflect the potential of employing dense grids for asteroseismology of PMS stars. Using the χ^2 defined in equation 6.1 we search our grids for close matches of the observed frequencies and the calculated adiabatic frequencies.

7.1 NGC 6530 85

Having five observed frequencies and lying inside the bounds of the instability strip, the data from NGC 6530 85 typifies the quality of oscillation spectra achievable from ground-based observatories. One of the frequencies has a very low amplitude and is similar in

frequency to another mode, which has been confirmed as a rotationally split mode (Guenther *et al.*, ApJ, submitted). Only the four frequencies with the largest amplitudes were used for comparison with the model spectra. Observed frequencies are listed in 7.1 alongside corresponding amplitudes with boldface indicating the frequencies selected for comparison to models. The observational uncertainty, corresponding to one over the duration time for the observations, is approximately 0.5 μHz. The observational uncertainty in the HR diagram position is unknown so we adopt arbitrary conservative values for $\Delta log(T_{eff})$ and $\Delta log(L/L_{M_\odot})$. The observed frequencies were compared to all models in both PMS and post-MS grids.

Table 7.1 Observed frequencies and amplitudes for NGC 6530 85 Zwintz *et al.* (2005b).

	frequency (μHz)	V Amp. (mmag)	B Amp. (mmag)
f1	**180.31**	30.2	39.1
f2	**146.99**	17.1	23.0
f3	179.76	8.2	11.4
f4	**122.51**	3.5	4.7
f5	**360.50**	1.8	2.0

In figure 7.1 we show the HR-diagram position of NGC 6530 85 and the locations of PMS models that match (have $\chi^2 < 1$) the observed frequencies. Better matches (lower χ^2) are signified by darker points, with the scale ranging from $\chi^2 = 0$ to $\chi^2 = 1$. Because only four observed frequencies are used, uniquely identifying the best model is not possible; indeed, thousands of the nearly 700,000 PMS models comprising the grid yield values of $\chi^2 < 1$. In figure 7.2 we show the χ^2 fit to each model that yielded $\chi^2 \leq 2$. The results are plotted against the χ^2 for the model, with filled circles indicating PMS models, and open circles indicating post-main sequence models. The model χ^2 is computed from the model and

observed HR-diagram locations and the corresponding observational uncertainties:

$$\chi^2_{model} = \frac{1}{2} \left(\frac{(T_{eff,mod} - T_{eff,obs})^2}{(\Delta T_{eff,obs})^2} + \frac{(L_{mod} - L_{obs})^2}{(\Delta L_{obs})^2} \right).$$ (7.1)

Results for PMS models are indicated with filled circles, and post-main sequence models with empty circles. Evidently the four observed modes of NGC 6530 85 can conclusively identify the star as PMS. The best post-main sequence models that are within the uncertainties of the observed HR diagram position all yield $\chi^2 \approx 2$. Although it is impossible to uniquely identify one of the PMS models as the solution, figure 7.2 demonstrates that there exists a locus of PMS models that provide a lower χ^2 than the others. This result also serves as an example of the necessity of high resolution grids, either with the strategy adopted here of computing dense grids, or through an accurate interpolation scheme. Without the ability to resolve models to a high degree, the entire group of models centered on $Log(T_{eff}) = 3.83$ and $Log(L/L_{\odot}) = 1.39$ (figure 7.1) would be missed.

We present the frequency spectrum of the model corresponding to the lowest χ^2 as an echelle diagram in figure 7.3. According to this model, the observed modes are $l = 0$ and $l = 1$, with the HR-diagram position closely matching the observed luminosity but with a modest difference in effective temperature. Although the frequencies were matched to model spectra consisting of $l = 0$, 1, 2 and 3 p-modes, the resulting best fit only requires p-modes of degree $l = 0$ and 1.
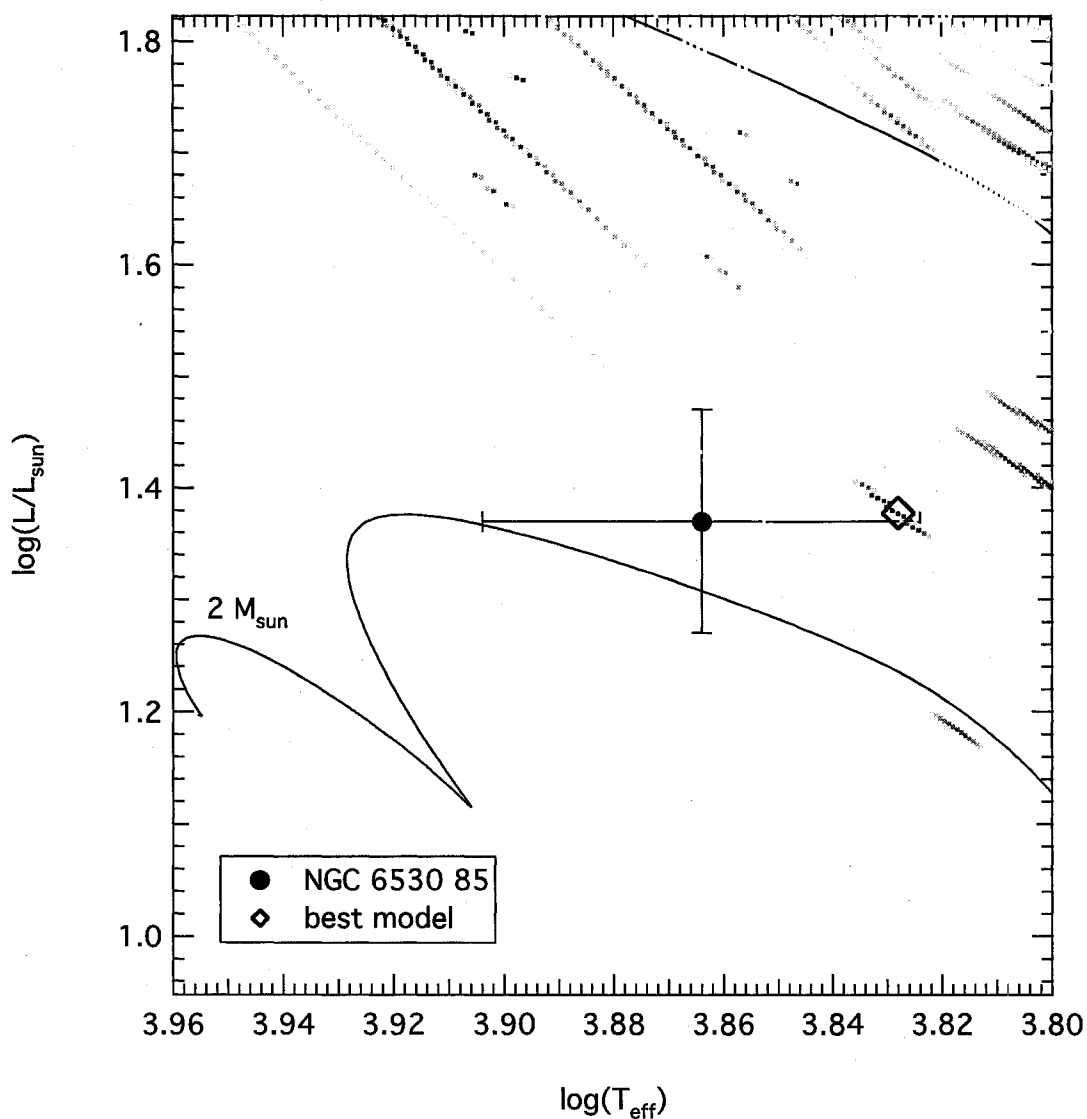
Figure 7.1 The HR-diagram location of NGC 6530 85 with the locations of models that match the observed frequencies with $\chi^2 < 1.0$. The grayscale is proportional to χ^2 with darker points indicating better matches. The model with the closest match is identified by the diamond.
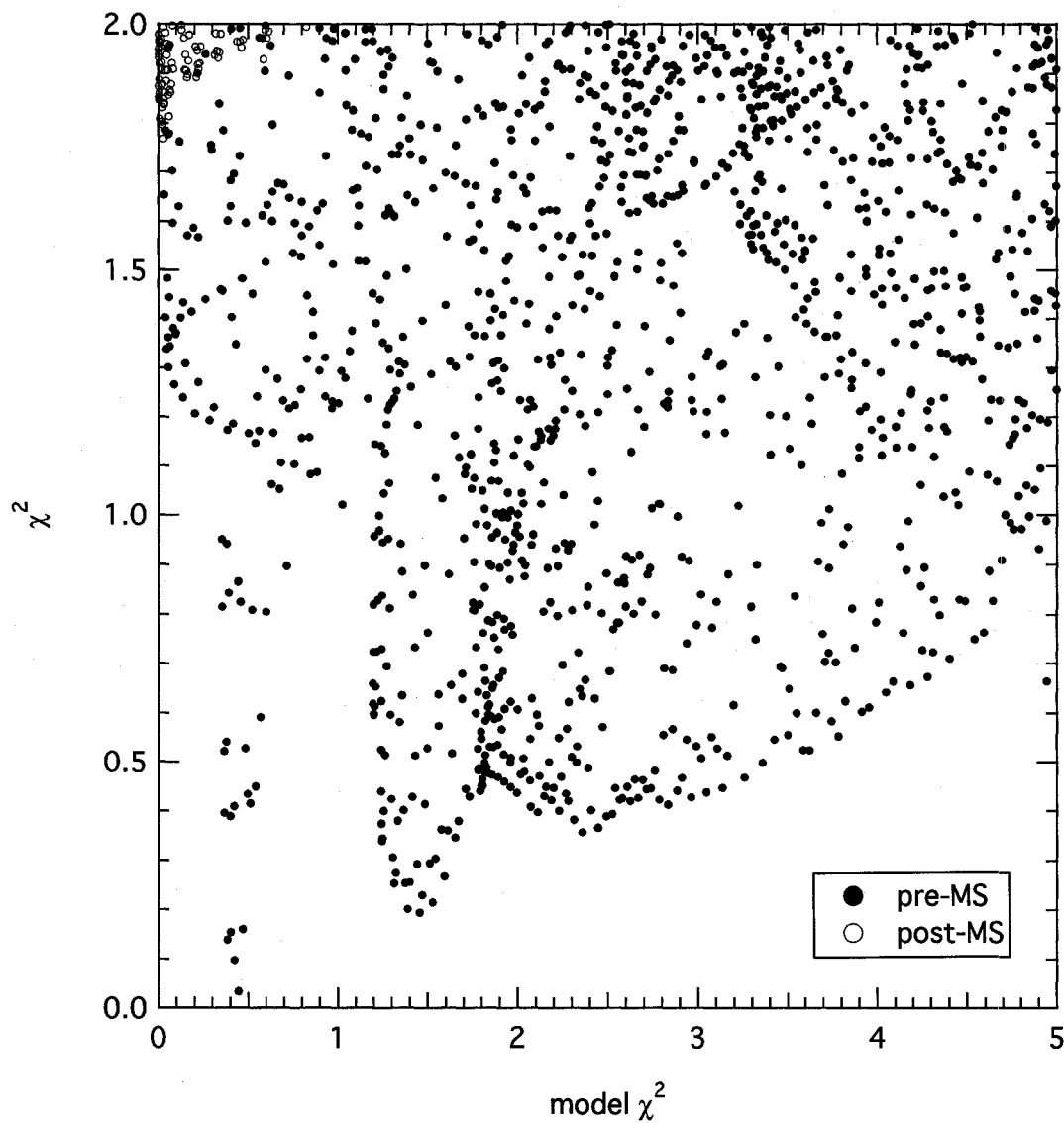
Figure 7.2 The χ^2 results from comparing the observed frequencies from NGC 6530 85 to the PMS and post-main sequence grids. PMS models are represented by filled circles and post-main sequence with open circles.
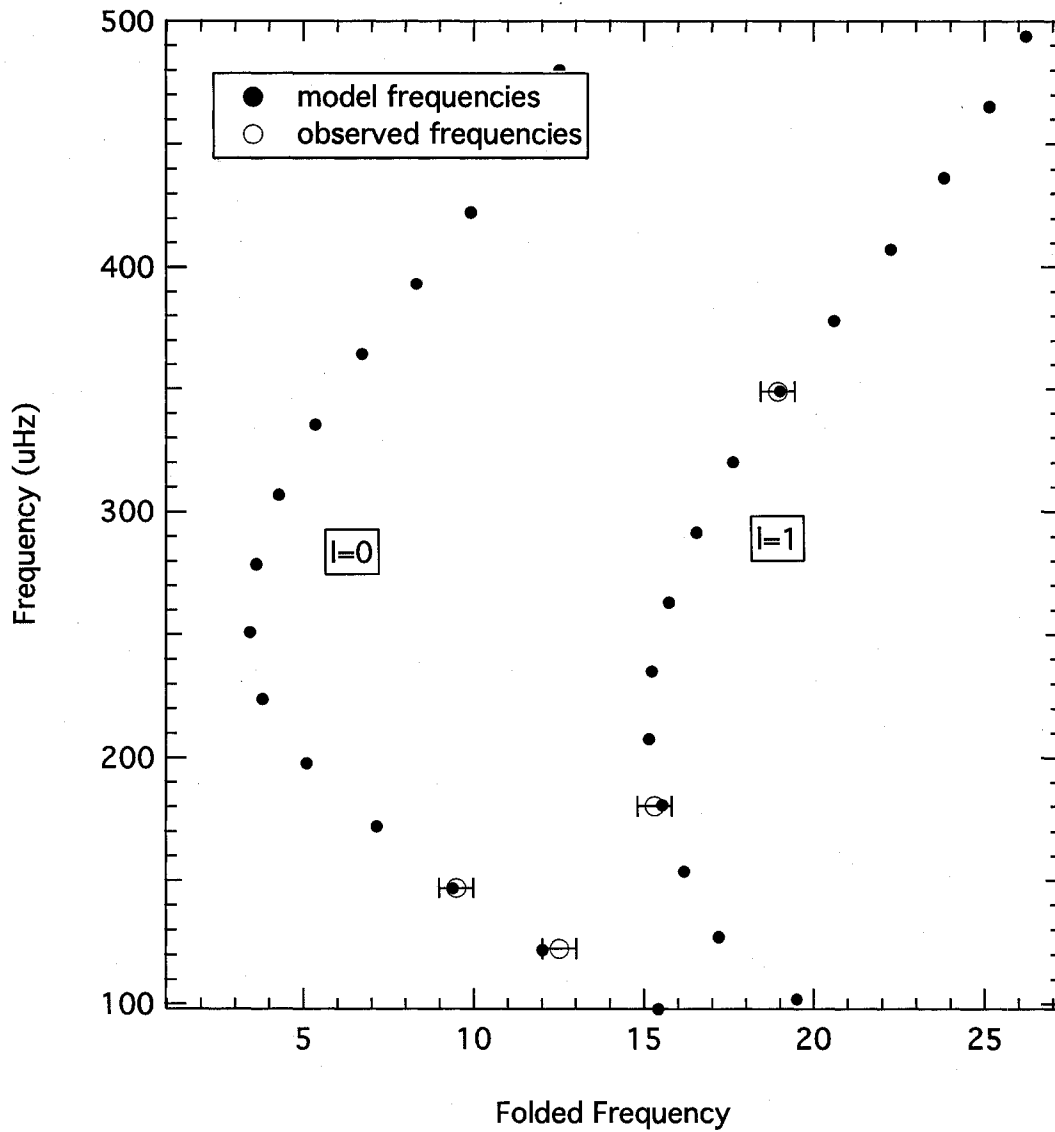
Figure 7.3 Echelle diagram for NGC 6530 85 compared with the frequency spectrum of the model with the lowest χ^2. The HR-diagram position of the model is identified in figure 7.1.

7.2 HD 104237

The Herbig Ae star HD 104237 (DX Cha) is a pre-main sequence spectroscopic binary system with a pulsating primary member. The system is bright ($V = 6.6$) and has well determined orbital parameters, however the stellar parameters are not well constrained. Estimates for the HR diagram position range from $Log(T_{eff}) = 3.929$ and $Log(L/L_\odot) = 1.55$ (van den Ancker *et al.*, 1998) to $Log(T_{eff}) = 3.869$ and $Log(L/L_\odot) = 1.41$ (Grady *et al.*, 2004), which we use to derive an uncertainty.

Oscillation frequencies were first detected in HD 104237 by Donati *et al.* (1997). Two subsequent observations totaling 42 nights of observing time yielded the detection of 8 pulsation frequencies (Böhm *et al.*, 2004). The observations comprise 1888 high resolution échelle spectra taken at the 1.9m Radcliffe telescope of the South African Astronomical Observatory and the Australian 74 inch telescope at Mt. Stromlo. Frequencies for the two runs are presented in table 7.2.

Table 7.2 Frequencies and amplitudes derived from the 1999 (left) and 2000 (right) data of Böhm *et al.* (2004).

|	frequency (μHz)	Amplitude (km/s)	frequency (μHz)	Amplitude (km/s)
f1	**385.29**	1.32	385.22	0.26
f2	**412.11**	0.47	412.14	0.33
f3	**329.90**	0.20	330.10	0.17
f4	**358.26**	0.14	358.94	0.18
f5	391.92	0.11		
f6	**377.50**	0.11	374.71	0.11
f7	403.70	0.10		
f8	408.33	0.05		

Because the metal abundance is unknown, we match the observed frequencies to the models

in the solar metalicity PMS grid. The five modes present in both data sets (identified with boldface text) were selected for comparison with our PMS models. Initially, the frequency matching was constrained to modes of degree $l = 0$ and $l = 1$ to narrow the solution space but we found no matches with $\chi^2 < 1$, however, matching to modes of degree $l = 0$ to $l = 3$ produced several models with $\chi^2 < 1.0$. Figure 7.4 shows the HR-diagram locations of models that yield $\chi^2 < 1$. Better matches (lower χ^2) are signified by darker points, with the scale ranging from $\chi^2 = 0$ to $\chi^2 = 1$. Although there are a host of individual models that provide matches to the observed data, these can be separated into two distinct regimes, each following a line of constant large spacing. In effect, the solution space represents two models that match the observed frequencies, with the lower temperature models yielding a superior statistical match.

We present the oscillation spectra of one of the models in each regime in figures 7.5 and 7.6. Echelle diagrams for nearby models with the same large spacing are similar. Based on the temperature and luminosity that each regime spans in the HR-diagram, we estimate the uncertainty of either solution as $\Delta Log(T_{eff}) \approx 0.02$ and $\Delta Log(L/L_\odot) \approx 0.05$. Changing the metalicity of the grid would shift the HR-diagram locations but produce similar results. Reducing the uncertainty associated with the observed frequencies would eliminate the hotter model. Alternatively, further observational constraints on HD 104237 or independent identification of the observed modes could be brought to eliminate one of these models.

Figure 7.5 demonstrates that 6 of the 8 observed frequencies were matched to the model, and 4 of them are sequential $l = 3$ modes. The modes are not necessarily $l = 3$ and

could be any degree, so long as the large spacing matches. Given the geometry of spherical harmonics, it is more likely that the modes are lower degree that are easier to detect from the ground. Identifying the degree of any of these 4 modes would further reduce the size of the solution space and constrain the HR diagram position through the large spacing for a specific degree.

Figure 7.6 shows that 5 of 8 frequencies are closely matched to the model, with two of the remaining unmatched frequencies approximately equidistant from an $l = 2$ mode. It is entirely possible that these frequencies are the result of rotational splitting, and if confirmed would provide compelling evidence to support the hotter model. Although a single solution remains elusive for HD 104237, the number of good matches is substantially less than for NGC 6530 85, which this is consistent with the findings of chapter 6. The possibility that 4 of the 8 frequencies are sequential modes also assists in reducing good model matches to cooler models that have large spacings of $\Delta_n \approx 25\mu Hz$.
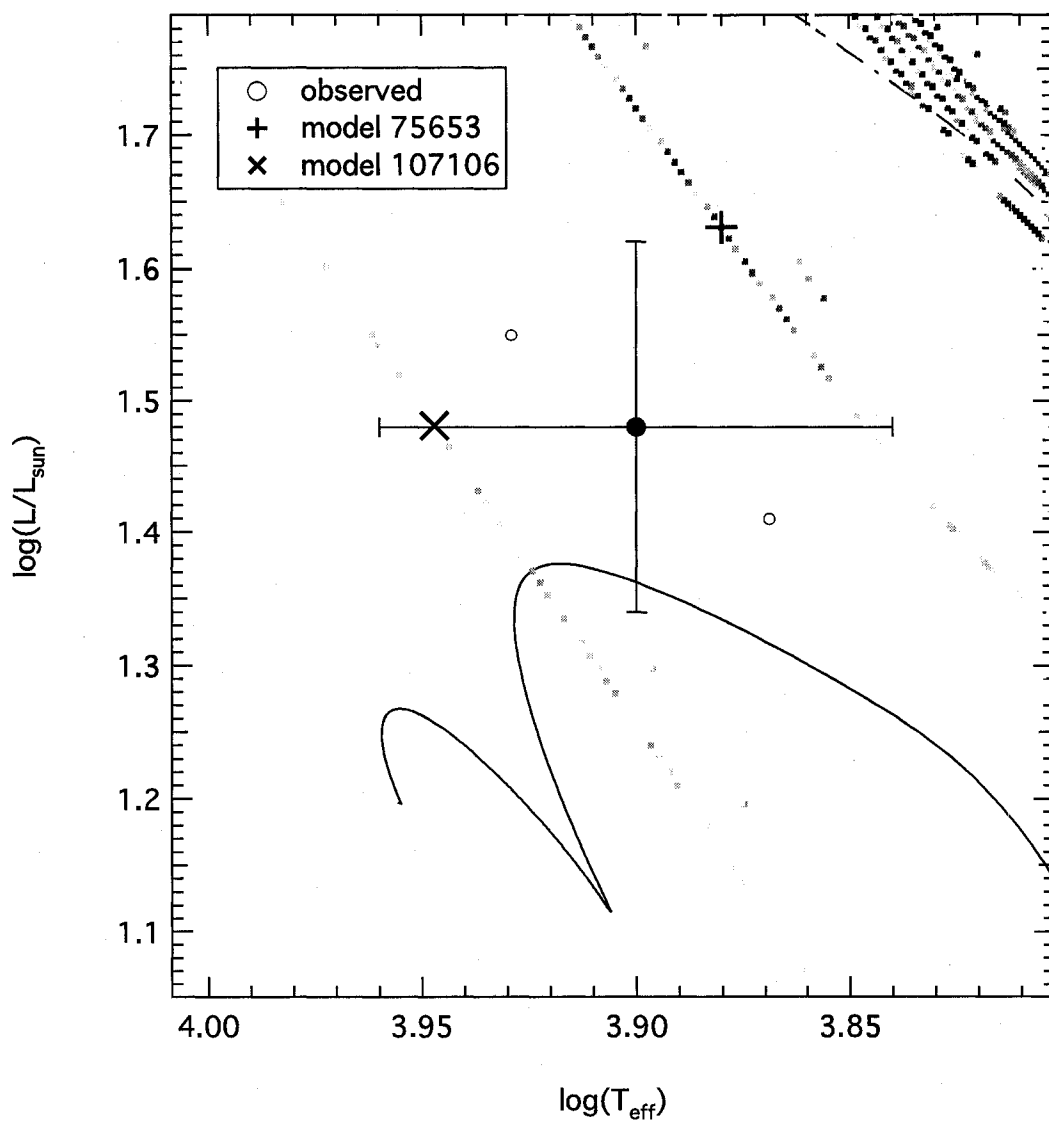
Figure 7.4 HR-diagram location of HD 104237 with the locations of models that match the observed frequencies with $\chi^2 < 1.0$. The grayscale is proportional to χ^2 with darker points indicating better matches.
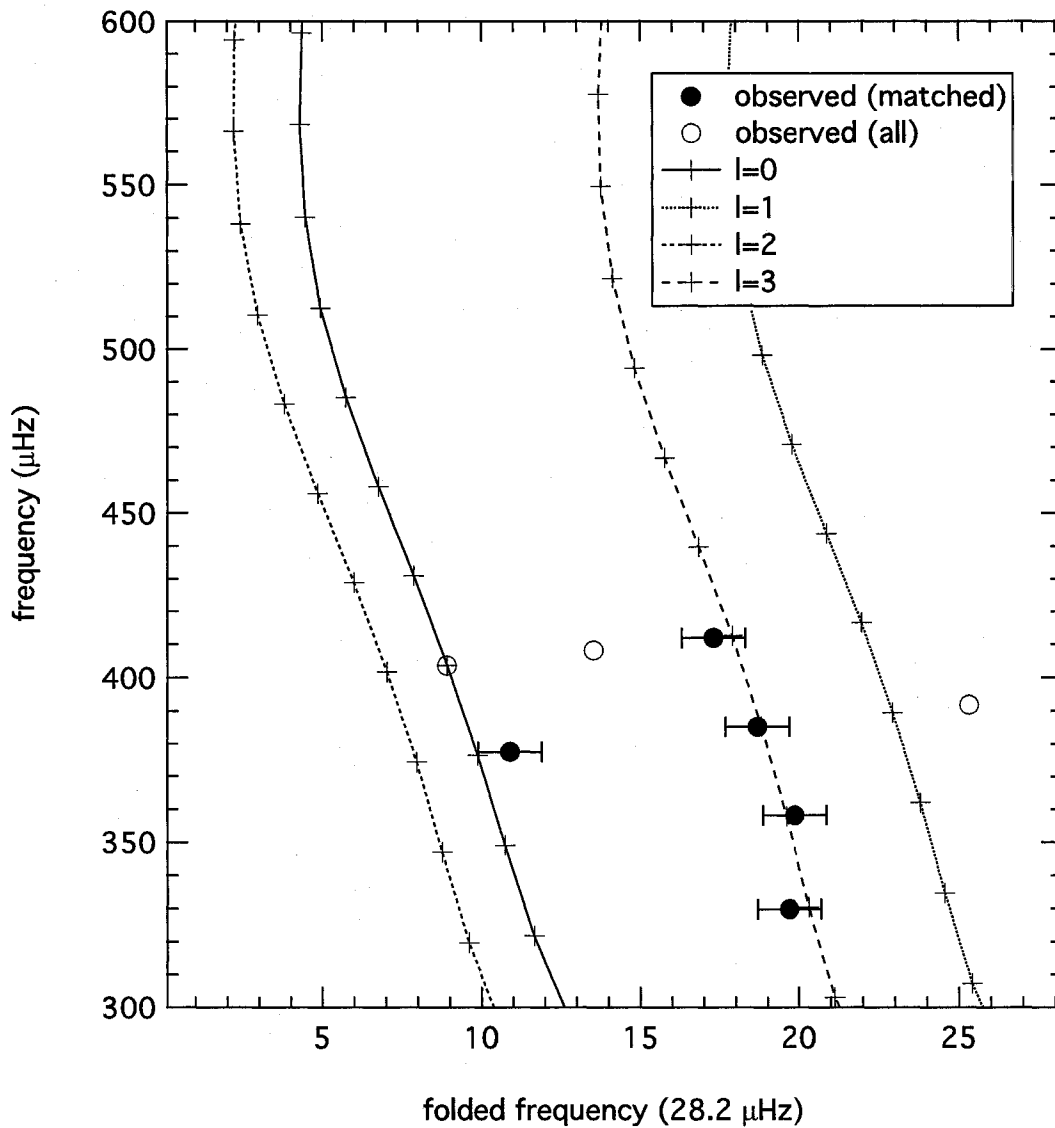
Figure 7.5 Echelle diagram of HD 104237 compared with the frequency spectrum of a close matching model. The HR-diagram position of the model is indicated as model 107106 in figure 7.4.
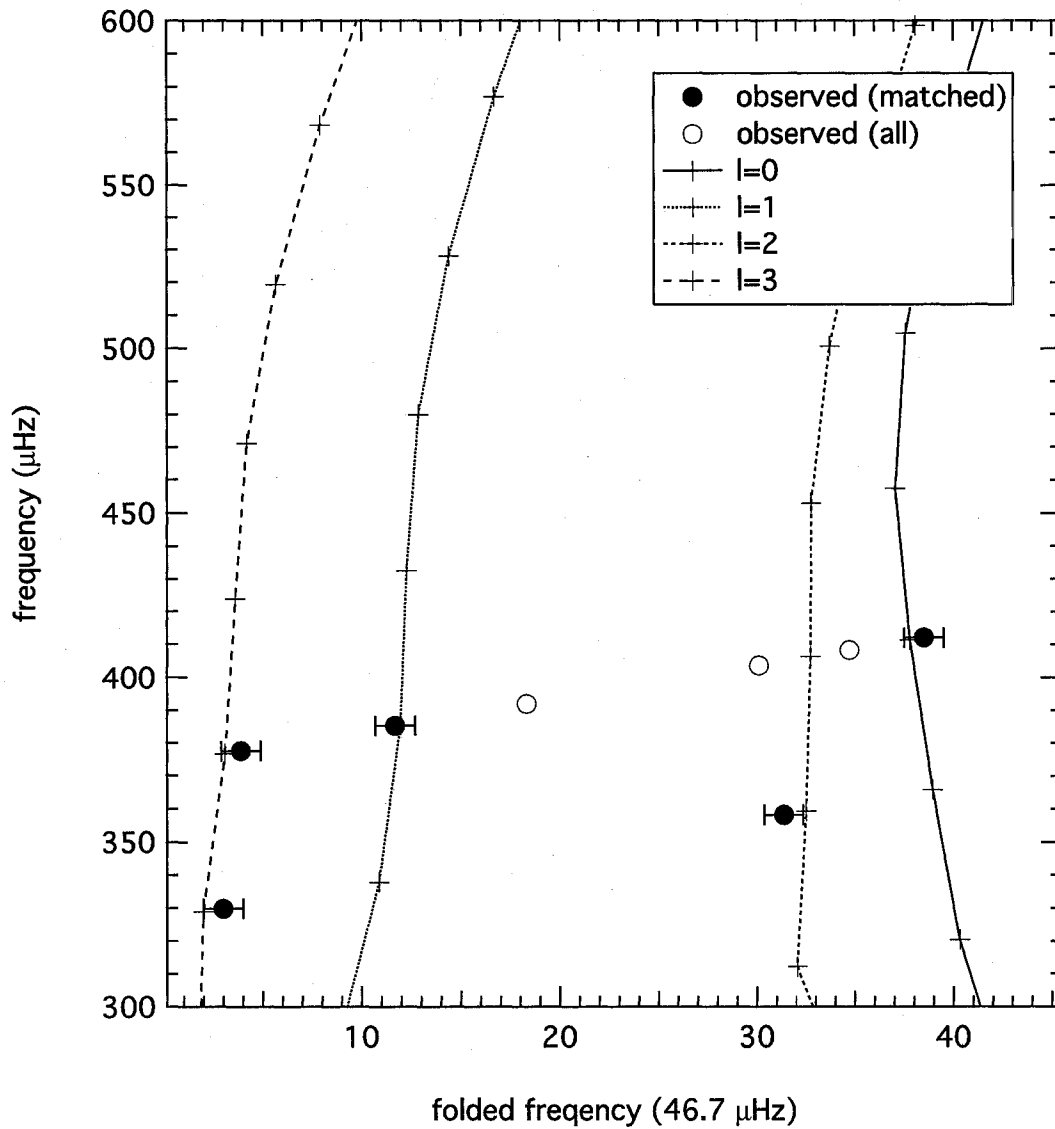
Figure 7.6 Echelle diagram of HD 104237 compared with the frequency spectrum of a close matching model. The HR-diagram position of the model is indicated as model 75653 in figure 7.4.

Chapter 8

Conclusions

We have calculated dense grids of models covering the intermediate mass range $((1.6 \leq M_\odot \leq 5.0))$ for pre- and post-main sequence evolutionary tracks. Pulsating PMS stars have been observed in the same δ Scuti instability strip as their post-main sequence counterparts. Because stars in both evolutionary stages can occupy the same HR-diagram position, the surface layers are similar, so determining the evolutionary stage can be ambiguous. We use asteroseismology to probe PMS stars by associating fundamental properties to p-mode oscillation spectra and through comparison with post-main sequence stars. *For models near the ZAMS, we find similar large spacings in both phases in both evolutionary stages, but marked differences in small spacings.* This finding reflects differences in the internal structure of PMS stars compared with post-main sequence stars with similar surface layers. We compare PMS and post-main sequence oscillation spectra by computing an "asteroseismic HR-diagram" in both evolutionary stages, which substantiates using asteroseismology as a tool for identifying evolutionary stages.

Through non-adiabatic analysis, we map the instability region for radiatively driven modes. *We find our instability strip encompasses all known PMS pulsators, and is consistent with the empirically determined blue edge.*

We computed new PMS isochrones, where the dense grid enabled us to resolve for the first time the nuclear burning 'bump' as PMS stars approach the ZAMS. We fit our isochrones to high quality photometry of the young open clusters IC 1590 and NGC 2264. *We find that the widening of the ZAMS in both clusters can be attributed in part to the nuclear burning 'bump' in our isochrones.* Because PMS stars evolve rapidly, isochrones are very sensitive to the zero age, and unlike post-main sequence isochrones which make use of the ZAMS, there is no equivalent for PMS stars. The birthline (Stahler, 1988) describes where PMS stars first appear, but is uncertain because of its sensitivity to mass accretion rates. Further, PMS isochrones are highly sensitive to uncertainties introduced by designating a PMS zero age and from our understanding of star formation. Rather than defining isochrones that are perfectly precise, we estimate the uncertainty in the PMS model ages, which results in isochrones that widen near the ZAMS. Our isochrones are in agreement with previously determined ages for the two young open clusters.

Unlike *helioseismology*, asteroseismoly deals with observations consisting of a handful of frequencies. Space missions like MOST and COROT are capable of detecting many more frequencies, but ground-based observations typically yield fewer than ten. An observed oscillation spectrum is always incomplete, and we can express the quality of the spectrum by the number of frequencies and the degree of precision to which we know them. The frequencies correspond to modes that may not be of the same degree or in sequential order. This limits our ability to use asteroseismology as a tool to constrain stellar properties, and is further complicated by mode bumping, which destroys the simple order of modes as predicted by asymptotic theory. The lack of mode bumping in PMS stars provides renewed

opportunity for asteroseismology.

We measure our ability to constrain stellar parameters through asteroseismology by constructing a set of artificial oscillation spectra with varied size and precision. We compare each artificial oscillation spectrum to the pre- and post-main sequence grids to find the models that match. Because all models in the solution match the artificial spectrum, our ability to constrain stellar properties is determined by the size of the solution space. As expected, higher precision or more frequencies yields fewer matched models. *We find that increasing the precision of the observations is more effective in reducing the size of the solution space than increasing the number of observed frequencies.* That is to say, few frequencies with high confidence imposes stronger constraints than large quantity of less reliable frequencies. We also find that more accurate observed oscillation spectra are required for stars further from the ZAMS than for those near the ZAMS to constrain stellar properties to the same degree of precision. This is caused by the larger radius of stars far from the ZAMS, which compresses the frequency spectrum.

Because pre-main sequence models rarely deviate from the simple asymptotic description, the solution space was found to group in regimes that trace models matching possible large spacings for the observed spectrum. This kind of solution is especially useful because the models in each subgroup share similar properties that can be tested against other observed criteria. This is true as well for post-main sequence frequency matching, but the chance alignment of frequencies from mode bumping yields models that are not aligned with contours of large spacing. This in turn makes the task of eliminating model matches considerably more onerous and perhaps impossible because the models can have

significantly different properties and must therefore be considered individually. Reducing the size of the solution space would require extremely precise frequency measurements, knowledge of the degree of individual modes, or very precise constraints on HR-diagram location.

To test our methods in the real world, we selected two pre-main sequence stars, namely NGC 6530 85 and HD 104237. We attempted to constrain their properties using asteroseismic data by matching the observed oscillation spectra to our model grids. We found the frequency matching results for NGC 6530 85 were consistent with the conclusions of the artificial oscillation spectrum fitting, with models comprising the solution space congregating around contours of large spacing in the HR diagram. The low number of observed frequencies permitted many matched PMS models, rendering a unique solution impossible. Notably, the four frequencies were only successfully matched to PMS models within the uncertainties of the HR diagram position. Further, the plethora of matched models includes a subset that defines a very small region in the HR diagram and produced the lowest χ^2 match to the observations. The salient point here is that the group models could easily have been missed through the use of a coarse grid.

The second observed spectrum belongs to HD 104237. Adhering to our findings in chapter 6, only the frequencies with the highest confidence levels were selected for matching to models. The resulting solution space contains models segregated according to large spacing. Constraining the properties further will require more precise frequencies, a larger observed oscillation spectrum, or additional information about existing frequencies such as identifying specific modes.

References

Aizenman, M., Smeyers, P. & Weigert A. 1977 A&A, 58, 41

Alexander, D. R., & Fergusion, J. W. 1994, ApJ, 437, 879

Banarjee, R. & Pudritz, R. E. 2007, ApJ, 660, 479

Baraffe, I., Chabrier G., Allard F., & Hauschildt P. H., 2002, A&A, 382, 563

Baraffe, I., Chabrier G., Allard F., & Hauschildt P. H., 1995, ApJL, 446, L35

Böhm, T., Catala, C., Balona, L. & Carter, B. 2004, A&A, 427, 907

Böhm-Vitense, E. 1958, *Zs. Ap.*, 46, 108

Breger, M. & Dyck, H. M. 1972, ApJ, 175, 127

Christensen-Dalsgaard, J. 1988, *A HR Diagram for Stellar Oscillations. Advances in Helio- and Astroseismology*, IAU Symp. No. 123, Kluwer, Dordrecht, pp. 295.

Christensen-Dalsgaard, J. 1993, ASPC, 42, 347

Christensen-Dalsgaard, J. 2003 *Lecture Notes on Stellar Oscillations* 5th ed.

Cox, J. P. 1980, *The Theory of Stellar Pulsation*, New Jersey, Princeton University Press

D'Antona F. & Mazzitelli, I., 1994, ApJS, 90, 467

Demarque, P. & Guenther, D. B. 1999, *Proc. Natl. Acad. Sci.* USA, 96, 5356-5359

Donait, J., F., Semel, M., Carter, B. D, Rees, D. E., Collier Cameron, A. 1997, MNRAS, 291, 658

Gough, D. 1987, A&A, 181, 289-292

Grady, C.A., Woodgate, B., Torres Carlos, A.O., *et al.* 2004, ApJ, 608, 809

Grevesse, N., Noels, A., & Sauval, A. J. 1996, in ASP Conf. Ser. 99. Cosmic Abundances, ed. S. S. Holt & G. Sonneborn (San Francisco: ASP), 117

Guenther, D. B., Zwintz, K. & Weiss, W. W. 2007, ApJ, 655, 342

Guenther, D., B., Zwintz, K., Weiss, W. W. & Tanner, J. 2007, ApJ, submitted

Guenther, D. B. 2004, ApJ, 612, 454

Guenther, D. B., 2002, ApJ, 569, 911

Guenther, D. B., 1994, ApJ, 422, 400

Guenther, D. B., Demarque, P., Kim, Y. -C., & Pinsonneault, M. H. 1992, ApJ, 387, 372

Guetter, H. H. & Turner, D. G 1997, AJ, 113, 2116

Hayashi, C. 1961, PASJ, 13, 450

Herbig G.H., 1960, ApJS 4, 337

Hillenbrand, L. A. 1997, AJ, 113, 1733

Iben, I. 1965, ApJ 141, 993

Iglesias, C.A. & Rogers, F.J. 1996, ApJ, 464, 943

Isaak, G. R. & Isaak, K. G. 2001, *Stellar Swismology, Stellar Ages and the Cosmological Constant*, In: Astrophysical Ages and Time Scales, ASP Conf. Series, vol. 245, (eds.) T. von Hippel, N. Manset, C. Simpson

Joy, A. H., 1942, PASP, 54, 15

Joy, A. H., 1945, ApJ, 110, 424

Larson, R. B. 2007, Reports on Progrss in Physics 70 (2007) 337

Lejeune, T., Cuisinier, F. & Buser, R. 1997 A&AS, 130, 65L

Morel *et al.* 1994, A&A, 286, 91

Osaki Y., 1975, PASJ, 27, 237

Palla, F. & Stahler, S. W. 1990, ApJL 360 L47-L50

Palla, F. & Stahler, S. W. 1991, ApJ, 375, 288

Palla, F. & Stahler, S. W. 1993, ApJ, 418, 414

Palla, F. & Stahler, S. W. 1999, ApJ, 525, 772-783

Park, B., Sung, H., Bessell, M. S. & Kang, Y. 2000, ApJ, 120, 894

Roxburgh, I. W. & Strittmatter, P. A. 1965 Za, 63, 15R

Stahler, S. W., Shu, F. H. & Taam, R. E. 1980 ApJ, 242, 226-241

Stahler, S. W. 1983, ApJ, 274, 822-829

Stahler, S. W. 1988, ApJ, 332, 804-825

Sung, H., Bessell, M. S., & Lee, S.-W. 1997, AJ, 114, 2644

Suran, M., Goupil, M., Baglin, A., Lebreton, Y., Catala, C. 2001 A&A, 372, 233

Swenson, F. J., Faulkner, J., Rodgers, F. J., & Iglesias, C. A. 1994, ApJ, 425, 286

Tassoul, M. 1980, ApJS, 469-490

Turner, D. G. Private Communication

Ulrich, R. K. 1986, ApJ, 306, L37-L40

van den Ancker, M. E., de Winter, D., Tjin A Djie, H. R. E. 1998, A&A, 330, 145

Zwintz, K. 2006, Ph.D. Thesis, University of Vienna

Zwintz, K. Marconi, M. Reegen, P., & Weiss, W. W. 2005, MNRAS, 357, 345

Zwintz, K. & Weiss, W. W. 2006, A&A, 457, 237

Unno, W., *et al.* 1989 *Nonradial Oscillations in Stars*, 2nd edition, (University of Tokyo, Tokyo).

Wuchterl, G. 1999, ASP, 173, 181